Dissertation

submitted to the

Combined Faculty of Natural Sciences and Mathematics of the

Ruperto Carola University Heidelberg, Germany

for the degree of

Doctor of Natural Sciences

Presented by

M.Sc. Franziska Dietrich

born in: Munich

Oral examination: 01.10.2020

A SYSTEM TO SEGMENT THE ROLE OF HYALURONIC ACID DURING RE-EPITHELIALIZATION

Referees: Prof. Dr. Ralf Bartenschlager

PD Dr. Heike Böhm

"To raise new questions, new possibilities, to regard old problems from a new angle, requires creative imagination and marks real advance in science."

Albert Einstein

Content

Abstract

Wound healing is a complex, multi-step process. To be able to comprehensively examine the role of hyaluronic acid (HA) on re-epithelialization it is crucial to isolate re-epithelialization as the process where keratinocytes migrate and proliferate from the other processes during wound healing. The effect of HA on re-epithelialization is controversially discussed in literature and comparability between independent studies is hampered as applied HA concentrations, molecular weight (MW) of HA as well as cell systems, substrate nature (glass, plastic) and extracellular matrix (ECM) composition all differ from publication to publication. Therefore, in this thesis I comprehensively compared for the first time the effect of apical presented HA of different MW (5, 60, 700 and 1800 kDA) and concentrations (5, 50, 500, 1000 µg/mL) within the framework of re-epithelialization using a human keratinocyte cell line (HaCaT). I showed that HA hampers migration on collagen I-coated glass surfaces in a concentration-dependent manner whereas in terms of proliferation HA has a pro-proliferative effect under conditions of low density on cell culture plastic.

With the aim to further reduce the complexity of the interplay of HA with other ECM molecules it is crucial to have a wound healing system comprising of a minimal number of components with the possibility to stepwise increase complexity. Following a bottom-up approach I employed bi-functionalized glass surfaces and altered their functional groups: Only HA and a second, integrin-addressing binding ligand were presented on an otherwise passivated background. In order to address different integrin-binding families I proved the established cRGD as well as a novel peptide, EPDIM to be suited to mediate HaCaT cell adhesion and subsequent spreading. Additionally, I investigated whether end-alkylated HA of 5, 10 and 60 kDA can be bound to azide-presenting surfaces via click chemistry. Surface saturation with HA was determined via QCM-D experiments and accessibility of surface-bound 5 and 10 kDA HA by the hyaladherin aggrecan proved bioactivity of immobilized HA. Surfaces presenting HA without additional adhesive peptides did not mediate HaCaT cell adhesion. Cell adhesion and subsequent spreading was observed on bi-functionalized glass surfaces with cRGD or EPDIM as a binding ligand together with three different concentrations of immobilized HA. Furthermore, indirect immunofluorescence revealed a direct correlation between immobilized HA and the degree of focal adhesion formation.

In order to mimic the dynamic changes in ECM composition during wound healing (e.g. when the provisional matrix evolves into granulation tissue) I developed a two-stage wound model system. I showed that formation of confluent monolayers on polycarbonate membranes was achieved within 24 h. By cutting such HaCaT-cultivated membranes (2D epidermal models) a real wound site was introduced. Customized molds enabled the mechanical fixation of membrane-cultivated HaCaTs on any desired surface without the need of collagen I glue thus ensuring a clean and well-controllable ECM environment without unintentional insertion of collateral ECM molecules. I demonstrated that such vegetated membranes can be used to observe migrational activities of keratinocytes in time-lapse

imaging on collagen I gels, collagen I-coated glass surfaces as well as on minimalistic, highly-defined ECM models, where only one single binding motif is presented. Furthermore, migration was also mediated upon providing bi-functionalized glass surfaces where the binding ligands cRGD or EPDIM were presented orthogonally with HA of varying concentration. In contrast to systems in which cells form a confluent layer on the same surface they migrate on after wounding, this novel two-stage ECM system ensures that the migration interface is not harmed by the wounding procedure and can be chemically different than the interface on which the cell monolayer has been cultivated.

Combining the two-stage ECM model with bi-functionalized surfaces creates a two-stage ECM wound healing model, which can be applied in 2D cell culture as well as 3D tissue systems and has the potential to reveal HA's signaling role in cooperation with other ECM molecules on re-epithelialization in future application.

Zusammenfassung

Wundheilung ist ein komplexer, mehrstufiger Prozess. Um die Rolle von HA während der Reepithelialisierung umfassend untersuchen zu können, muss der Prozess der Reepithelialisierung, in dessen Rahmen Keratinozyten migrieren und proliferieren, von den anderen Prozessen während der Wundheilung isoliert werden. Der Effekt der HA auf die Reepithelialisierung wird in der Literatur kontrovers diskutiert. Unterschiedliche Konzentrationen an eingesetzter HA, unterschiedliche Molekulargewichte, sowie Zellsysteme, Beschaffenheit der Oberfläche (Glas oder Plastik), sowie die Zusammensetzung der extrazellulären Matrix (EZM) erschweren die Vergleichbarkeit von unabhängigen Forschungsstudien. Daher wurde im Zuge dieser Dissertation der Effekt von apikal präsentierter HA unterschiedlichen Molekulargewichts (5, 60, 700 und 1800 kDA) sowie unterschiedlicher Konzentrationen (5, 50, 500, 1000 µg/mL) im Rahmen der Reepithelialisierung und unter Verwendung einer humanen Keratinozyten-Zelllinie (HaCaT) zum ersten Mal umfassend verglichen. Ich habe nachgewiesen, dass HA die Migration auf Kollagen I beschichteten Glasoberflächen konzentrationsabhängig hemmt, wohingegen die Proliferation bei geringen Zelldichten auf Plastikoberflächen durch HA gefördert wird.

Um die Komplexität im Zusammenspiel von HA mit anderen EZM Molekülen zu reduzieren ist es wichtig, zunächst ein Wundheilungssystem mit möglichst wenig Komponenten zu entwickeln, dessen Komplexität im Anschluss schrittweise erhöht werden kann. Im Sinne einer *bottom-up* Strategie habe ich bi-funktionalisierte Oberflächen verwendet und entsprechend angepasst: nur HA sowie ein zweiter Integrin-adressierender Bindeligand wurden auf einer ansonsten inerten Oberfläche präsentiert. Dabei habe ich mit dem Ziel, unterschiedliche Integin-bindende Familien zu adressieren, bewiesen, dass sowohl die etablierte Bindesequenz cRGD, sowie ein neues Bindemotiv, EPDIM erfolgreich Zelladhäsion und Zellspreiten vermitteln. Zusätzlich habe ich untersucht, ob end-alkylierte 5, 10 oder 60 kDA HA über Click Chemie auf Oberflächen, die Azidgruppen präsentieren, immobilisiert werden kann. Die Oberflächensättigung mit HA wurde mit Hilfe von Quarzkristall-Mikrowaagen mit Dissipationsaufzeichnung (QCM-D) bestimmt und die Bioaktivität von immobilisierter 5 und 10 kDA HA über Aggrecanbindung konnte bewiesen werden. Zellen konnten nicht auf Oberflächen, die nur HA und keine weiteren Haftmotive präsentierten adhärieren. Auf bi-funktionalisierten Oberflächen, die cRGD oder EPDIM sowie HA in drei unterschiedlichen Konzentrationen präsentierten, konnten Zellen anhaften und anschließend auch spreiten. Des Weiteren konnte durch indirekte Immunfluoreszenz gezeigt werden, dass ein direkter Zusammenhang zwischen der Menge an immobilisierten HA und der Ausbildung von Fokaladhäsionen bestand.

Um dynamische Änderungen in der EZM Zusammensetzung während der Wundheilung (beispielsweise, wenn der Blutpfropf zu Granulationsgewebe reift) zu simulieren, habe ich ein zweistufiges Wundmodelsystem entwickelt. Dabei konnte ich zeigen, dass innerhalb von 24 h ein konfluenter Zellmonolayer auf Polykarbonatmembranen gebildet wurde. Indem die HaCaT

bewachsenen Membranen (2D epidermale Modelle) in der Mitte durchgeschnitten wurden, wurde eine echte Verwundung dieses Zellrasens verursacht. Durch die Verwendung von spezifisch angepassten Formen konnten Membran-kultivierte HaCaT Zellen auf beliebigen Oberflächen fixiert werden, ohne dass Kollagen I Kleber verwendet werden musste. Dadurch wurde eine hochkontrollierte EZM Umgebung ohne das Risiko von Verunreinigungen mit ungewollten EZM Molekülen gewährleistet, Ich habe in Zeitraffer-Aufnahmen zeigen können, dass derartige 2D epidermalen Modelle verwendet werden können, um Keratinozytenmigration auf Kollagen I Gelen, Kollagen I beschichteten Oberflächen, aber auch auf minimalistischen, hoch-definierten EZM Modellen, die nur ein einziges Bindemotiv präsentieren, auszulösen. Zudem konnte Zellmigration auch auf bi-funktionalisierten Oberflächen, die die Bindeliganden cRGD oder EPDIM zusammen mit unterschiedlichen HA Konzentrationen präsentierten, beobachtet werden. Im Gegensatz zu anderen Migrationsassays, bei denen die Zellen auf derselben Oberfläche, auf der sie migrieren sollen, einen Monolayer bilden, beinhaltet dieses neue Zweistufen- EZM-Model den Vorteil, dass die Migrationsoberfläche nicht durch die Verwundung selbst beeinträchtigt wird. Zusätzlich kann die erste EZM Stufe chemisch anders zusammengesetzt sein als die zweite Stufe.

Durch die Kombination beider Systeme, die des zweistufigen EZM-Models sowie das der hochdefinierten bi-funktionalisierten Oberflächen, entsteht ein zweistufiges EZM-Wundheilungsmodell, das in 2D Zellkulturen sowie in 3D Zellkulturen verwendet werden kann. Dieses Modell hat das Potential, in Zukunft die Rolle von HA in der Signalweiterleitung und ihr Wechselspiel mit anderen EZM Molekülen während der Reepithelialisierung aufzudecken.

1 Introduction

1.1 The human skin

All vertebrate organisms are covered and protected by skin, the largest organ in the body (Smith and Melrose, 2015). The skin consists of a wide variety of different cells such as keratinocytes, fibroblasts, melanocytes, vascular endothelial, lymphatic endothelial, melanocytes, and nervous cells. Structurally, the skin can be separated in the epidermis and the dermis (Smith and Melrose, 2015). The epidermis represents the outermost barrier against the environment and is a multi-layered stratified squamous epithelium formed by tightly packed keratinocytes (Rittié, 2016). As the epidermis is continuously renewed, keratinocytes proliferate at the basal side and eventually differentiate on their way to the *stratum corneum*, the top layer of the epidermis (Figure 1). On the basal side, the epidermis is separated from the underlying dermis by the basement membrane (BM) mainly consisting of collagen IV, laminin 111 (former laminin 1) and laminin 332 (former laminin 5) (Larjava, Häkkinen and Koivisto, 2013; Iorio, Troughton and Hamill, 2015) (Figure 1).

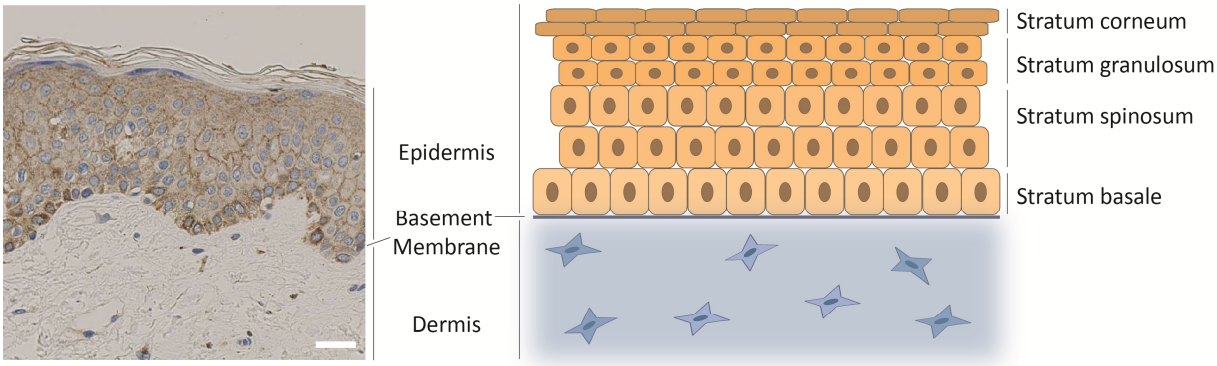

Figure 1: Structure of the human skin. Left: Histological section of human skin stained with hematoxylin and eosin. The epidermis is separated from the dermis by a basement membrane. Scale bar: 100 µm (provided by N. Grabe); Right: Scheme of the skin. The dermis comprises of dermal fibroblasts. In the epidermis keratinocytes proliferate at the basal side and eventually differentiate and by this cornify on their way to the stratum corneum, the top layer of the epidermis. EM image adopted from Nils Grabe *Note: the color change indicates the level of cornification, the darker the higher; scheme not according to scale*

Dermal fibroblasts are located in the dermis, a collagen-rich (almost 90 % collagen I and 10 % collagen III, 2% collagen V) connective tissue (Krieg and Aumailley, 2011). The extracellular matrix (ECM) in the skin is mainly produced by those fibroblasts (Rittié, 2016) (Figure 1). Within the ECM one can distinguish between structural and non-structural components. Within the structural components fibrous as well as non-fiber forming components exist (Järveläinen *et al.*, 2009). Fiber-forming proteins in human skin determine the three-dimensional structure and define both rigidity and elasticity of the tissue. In the skin, these are especially collagens (up to 77 % of dry weight human skin (Weinstein and

Boucek, 1960)) but also fibrin, fibronectin, vitronectin, elastin and fibrillin are found (Frantz, Stewart and Weaver, 2010). Non-fiber forming components, such as proteoglycans and glycosaminoglycans (GAG), fill the interstitial space in the tissue and influence the 3D structure as well as the mechanics of the tissue. Proteoglycans typically comprise a core (glyco)protein, which is non-covalently connected to large GAG side-chains (Ghatak *et al.*, 2015). GAGs (or mucopolysaccharides) are non-branched polysaccharides of repeating disaccharide units. Due to their hygroscopic character they contribute to the viscoelasticity of the tissue (Tracy, Minasian and Caterson, 2016). Typical GAGs and proteoglycans in the skin are hyaluronan, dermatopontin, versican, decorin, biglycan, lumican, keratocan, fibromodulin, perlecan and syndecans (Smith and Melrose, 2015). Non-structural proteins such as osteopontin, SPARC, CCN2, Tenascin-C and Fibulin-5 represent the so called matricellular proteins, which modify cell-matrix interactions (Järveläinen *et al.*, 2009). These proteins can often only be found in the skin's ECM upon wounding and disappear after the wound has been healed. (Tracy, Minasian and Caterson, 2016).

1.2 Cutaneous wound healing at a glance

Once the skin as the barrier against the outer environment is wounded it needs to be restored as fast as possible to fulfil its protection function. The process of cutaneous wound healing comprises multiple overlapping and tightly orchestrated steps. In general, three major phases can be distinguished: (i) coagulation with inflammation, (ii) proliferation and (iii) tissue remodeling (Xue and Jackson, 2015) (Figure 2). The complex process of wound healing is tightly regulated with different cell types as well as cytokines, growth factors and chemokines being involved (Pastar *et al.*, 2014). Delay or lack of one healing step may lead to impaired wound healing, which in turn may result in a non-healing, chronic wound.

Upon wounding, hemostasis is the first thing to occur. A coagulation cascade is induced which finally results in a fibrin clot consisting of a mesh of cross-linked fibrin fibers, as well as to a smaller extent plasma fibronectin and vitronectin carrying platelets (Reheman *et al.*, 2005; Wang *et al.*, 2014). This fibrin clot harbors cytokines and growth factors, which attract circulating immune cells. The first cells to enter the wound side are neutrophils. They degrade cell debris and phagocyte bacteria but also release further cytokines, which probably activate fibroblasts and keratinocytes at a very early stage in wound healing (Martin, 1997). Eventually, macrophages (in their de-differentiated monocyte-form) infiltrate the wound site and phagocyte remaining cell debris as well as neutrophils. Additionally, macrophages secrete chemical mediators such as transforming growth factor β (TGF-β) and vascular endothelial growth factor (VEGF) to recruit fibroblasts and endothelial cells (Alhajj, Bansal and Goyal, 2020). Macrophages stay in the wound site until healing has been completed. Once the wound site is cleaned from bacteria and cell debris, inflammation decays and wound healing proceeds in the proliferation phase (Figure 2).

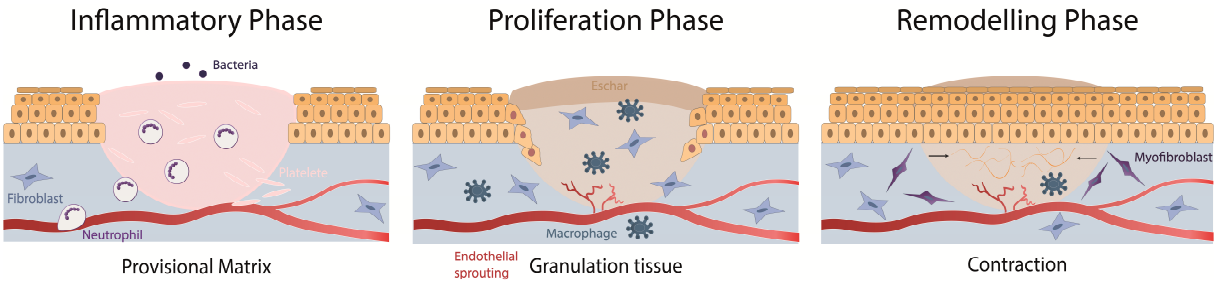

Figure 2: Wound healing at a glance.

The main task of the proliferation phase is to reconstruct the damaged skin. With the recruitment of endothelial cells new capillaries are formed, giving the healing wound an overall pinkish color (Alhajj, Bansal and Goyal, 2020). Fibroblasts, being recruited to the wound site, proliferate and rapidly expand. They produce most of the structural proteins necessary for tissue reconstruction, thereby transforming the provisional matrix (the fibrin clot) into granulation tissue (Rittié, 2016). This in turn provides the matrix on which keratinocytes migrate into the wound site (Pastar *et al.*, 2014). This process called re-epithelialization will be discussed in detail later. Once the leading edges of adjacent migration fronts meet each other, keratinocytes start to differentiate in apical direction leading to stratification and thickening of the epidermis (Figure 2).

Upon closure of the wound site by epidermal keratinocytes, efforts are made to reverse all cellular responses as well as extracellular rearrangements having been initiated to mediate wound healing. A special focus lies in the attempt to restore the tensile strength of the ECM (Gonzalez *et al.*, 2016). The wound size and in particular its thickness, partial (BM is mostly intact; dermis is slightly wounded) or full (dermis is fully wounded), as well as intensity and duration of the inflammation phase and efficiency of re-epithelialization all determine the success of the remodeling and thus the extent of scarring (Rittié, 2016).

Interestingly, early fetal developing skin heals scarless and amniotic fluid accelerates re-epithelialization in a human wound model, both demonstrably due to their increased content in HA and hyaladherins (Toole, 2004; Tracy, Minasian and Caterson, 2016).

1.2.1 The ECM during wound healing

The composition of the ECM within the wound site reflects the wound healing phase. At the beginning, the wound site comprises mainly cross-linked fibrin with platelets, vitronectin and plasma fibronectin incorporated in that mesh (Clark *et al.*, 1982) (Table 1). As mentioned above, once fibroblasts invade into this fibrin mesh, the initial provisional matrix is replaced by granulation tissue. Granulation tissue contains mostly collagens. At the beginning collagen III dominates which is eventually replaced by collagen I (Table 1). Besides collagens the granulation tissue further comprises

proteoglycans and cellular fibronectin as well as the matricellular proteins thrombospondin1, osteopontin, SPARC and tenascin C (Rousselle, Montmasson and Garnier, 2019).

Finally, epidermal keratinocytes deposit their own ECM in order to re-establish the BM. Laminin 332 is the first BM component deposited on the way to restore the BM during wound healing. Besides, collagen IV and VII, perlecan and nidogens contribute as well to the reforming BM (Rousselle, Montmasson and Garnier, 2019) (Table 1).

Table 1: ECM composition during wound healing

Provisional Matrix	Granulation tissue	Reforming basement membrane
Fibrin	Collagen I	Laminin 332
Plasma Fibronectin	Collagen III	Laminin 111
Vitronectin	Cellular Fibronectin	Collagen IV
	Glycosaminoglycan (increased HA)	Collagen VII
		Glycosaminoglycans

An imbalance in the ECM composition during wound healing contributes to impaired, delayed or a fail in re-epithelialization and thus provokes chronic, non-healing wounds or hypertrophic scars (Ghatak *et al.*, 2015).

1.2.2 Re-epithelialization

Re-epithelialization comprises migration, proliferation and differentiation. Re-epithelialization is a very critical step as the skin's integrity is restored (Xue and Jackson, 2015; Rittié, 2016). The migration of keratinocytes into the wound site starts a few hours upon wounding during the proliferation phase. Re-epithelialization requires the activation of wound-adjacent keratinocytes, which in a healthy tissue are tightly packed. To acquire a motile phenotype (Pastar *et al.*, 2014), the adhesive contacts to neighboring cells (desmosomes) and to the basal lamina (hemidesmosomes) need to become loose. As cell-cell contacts are not fully dissolved, keratinocyte migrate collectively. In addition, migrating keratinocytes deposit matrix-metalloproteases (MMPs) to break down ECM components and pave the migration path. If upon wounding both the epidermis as well as the dermis are affected (a so-called full thickness wound) the wound site is first "filled" with fibronectin before keratinocytes invade the wound site (Eckes, Nischt and Krieg, 2010). For this, keratinocytes adapt their integrin expression, enabling them to migrate on top of the provisional matrix right under the eschar of the wound (Pastar *et al.*, 2014). It has been postulated that collagen I contributes to keratinocyte activation before they migrate (Guo, Toda and Grinnell, 1990). Additionally, there is a feedback loop between collagen I (as well as collagen IV) and expression of collagenase (MMP-1) (Petersen *et al.*, 1990). In line with this, *in vitro*

studies showed a promoted migration of human keratinocytes on type I and IV collagens, vitronectin, and fibronectin (Woodley, Bachmann and O'Keefe, 1988; Brown *et al.*, 1991). Keratinocytes at the leading edge secrete laminin 332 in order to restore the basement membrane (Frank, 2004). Depending on post-translational modifications laminin 332 acts initially pro-migratory before it is stably integrated in the BM, where it promotes adhesion and anchoring of keratinocytes (Michopoulou *et al.*, 2020).

Simultaneously, cells in the periphery of the wound site re-enter the mitotic cycle and start to proliferate to provide new cells, contributing to the migrating pool. The proliferating rate is regulated by growth factors, degree of differentiation and cell adhesion to the ECM (Morasso and Tomic-Canic, 2005). The exact spatio-temporal organization of proliferation and migration during re-epithelialization is still being discussed. While some authors claim a clear separation between proliferating and migrating cells, others postulate that the proliferation and migration zone overlap in the middle (Safferling *et al.*, 2013; Park *et al.*, 2017). As the first study was performed in a human and the second in a murine system, it is indistinct whether deviations in their observation can be ascribed to the different model systems used.

How re-epithelialization is terminated is not fully evaluated. It has been described that the confluence plays a key role in keratinocyte's behavior switch: at low density, keratinocytes proliferate and migrate whereas upon reaching confluence, growth arrest and differentiation are triggered by maturated cell-cell contacts (Perrais *et al.*, 2007). Additionally, ECM proteolysis and BM (re-)formation are controlled by confluence (Botta *et al.*, 2012).

1.2.3 Integrins – mediators to the ECM

Cells interact with the ECM via integrins. Integrins are heterodimers of α and β subunits consisting of an intracellular, transmembrane and extracellular domain. There are eighteen α- and eight β-subunits which make all together 24 integrin subtypes (Longmate and DiPersio, 2014). These subtypes can be grouped in several integrin families depending on respective binding motifs within the ECM which are recognized by the integrin's extracellular domain: fibronectin (via the RGD binding motif), collagen, laminin or leucocyte receptors (Figure 3 A). Integrins are bi-directional signaling receptors that transmit chemical as well as mechanical information of the surrounding matrix into the cell (outside-in signaling), or cells adapt their environment according to their needs (inside-out signaling) (Longmate and DiPersio, 2014). As the integrin's intracellular domain is connected by a multi-protein complex to the cytoskeletal proteins, cell reactions towards its environment such as cell shape, polarization or motility are mediated (Kapp *et al.*, 2013) (Figure 3 B). In the epidermis, integrins are mainly expressed by basal keratinocytes sitting on the basement membrane. Upon differentiation and on their way to the top layers of the skin, keratinocytes eventually lose their integrin expression. The pre-dominant integrins expressed in an intact epidermis are α2β1 (collagen receptor), α3β1 (laminin 332 and laminin 511) and α6β4 (mainly laminin 332, in hemidesmosomes) (Longmate and DiPersio, 2014). Upon wounding and

activation of keratinocytes the expression profile of integrins changes due to the altered ECM environment. The most affected integrins belong either to the fibronectin- (e.g. α5β1) or the laminin-binding family (e.g. α3β1) and their absence is correlated with erroneous wound closure (Longmate and DiPersio, 2014).

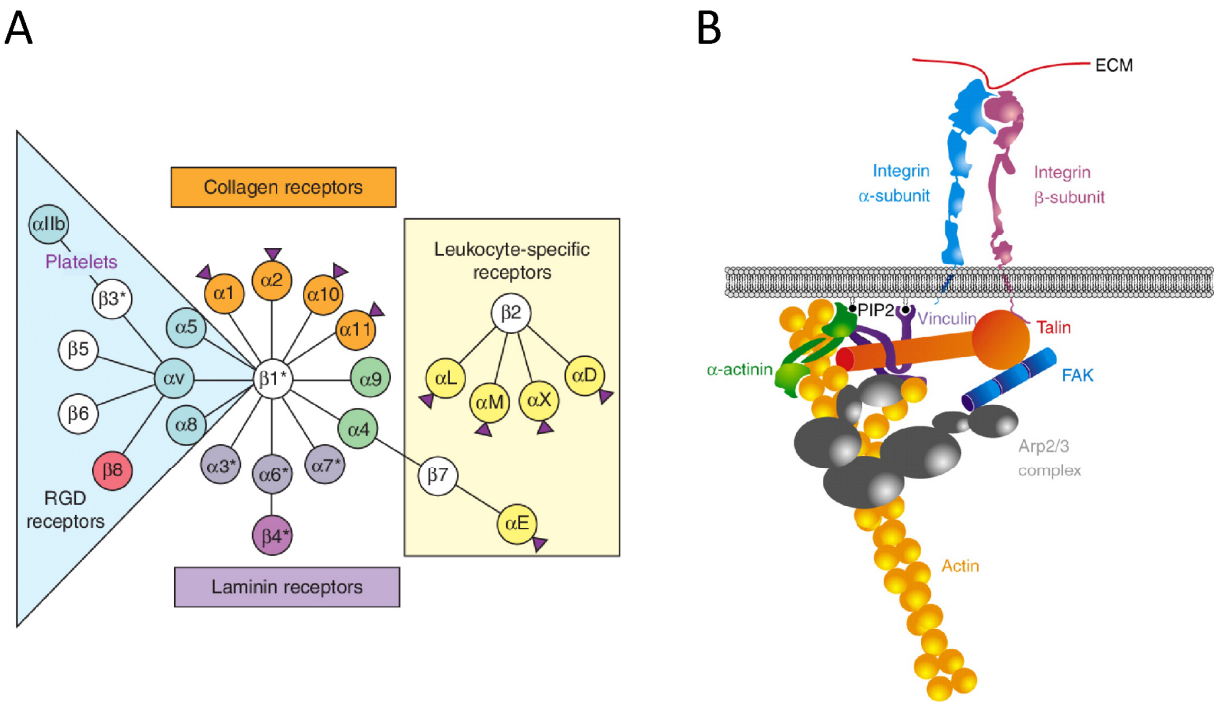

Figure 3: A) Integrin heterodimer families. (B) Linkage between integrins and the actin cytoskeleton. Adopted from (A) (Hynes and Naba, 2012) and (B) (Vicente-Manzanares, Choi and Horwitz, 2009)

1.3 Hyaluronic acid – a structural and regulatory polymer

1.3.1 Structure and properties of HA

Hyaluronic acid or hyaluronan (HA) is a highly conserved GAG composed of repeating disaccharide units of D-glucuronic acid and *N*-acetyl-D-glucosamine, linked via alternating β-(1-4) and β-(1-3) glycosidic bonds. (Monslow *et al.*, 2009) (Figure 4). As all other GAGs, HA belongs to the non-fiber forming components of the ECM (Tracy, Minasian and Caterson, 2016). However, HA is special within the GAGs, being the only non-sulfated GAG and not being attached to a protein core. Under physiological conditions, HA is a polyanion associated with extracellular cations (Na^+, Ca^{2+}, Mg^{2+}, K^+) (Mero and Campisi, 2014).

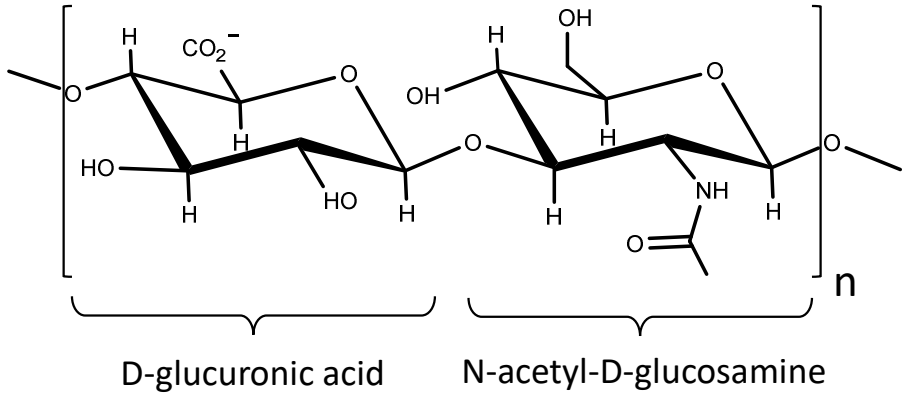

Figure 4: Chemical structure of HA.

HA occurs extracellular, bound to cellular receptors or intracellular (Anderegg, Simon and Averbeck, 2014). Extracellular HA can form intra- as well as inter-molecular crosslinks via hydrogen bonds. It can be also bound to extracellular proteoglycans such as versican or aggrecan, as well as other matrix proteins such as collagen. Overall, this composition is essential for the structural stability of the ECM. Especially when tissues are remodeled, e.g. during development or during wound healing, HA levels increase and as the polymer is permanently degraded by hyaluronidases, HA species of different sizes appear. HA with a very low molecular weight (LMWHA) has a more rod-like structure whereas high molecular weight HA (HMWHA) polymers form more compact random coils. The conformation depends on the number of molecule bonds: the lesser bonds the lesser degrees of freedom and subsequently the more rigid is the polymer. HA has been reported to have a persistence length of 4.2 nm in 0.2 M NaCl solution at 25 °C, determined by data from dynamic light scattering and low shear viscometry (Takahashi *et al.*, 1999) and of 6.8 and 7.5 nm, respectively in 0.15 M NaCl at 37 °C determined by data derived from multiangle light scattering (Mendichi, Šoltés and Giacometti Schieroni, 2003). Both studies used a comparable size range of 59.4-6270 kDa and 40-5500 kDa, respectively. The persistence length defines the bending stiffness of a polymer. Hence, if the polymer is shorter than the persistence length it is expected to have a linear conformation. Weigel and Baggenstoss reported that based on data derived by size exclusion chromatography and multiangle light scattering HA smaller than 100 kDa has a more rod-like structure whereas HA bigger than 300 kDa occurs more coil-like. They observed that in the range from 100 to 300 kDa different HA polymers can have either the one or the other conformation (Weigel and Baggenstoss, 2017). With its different size, HA plays different roles.

Under healthy tissue conditions HA can have a molecular weight of several million Dalton (Balazs *et al.*, 1967; Dahl,' *et al.*, 1985). Basically, HMWHA acts as a structural component of the ECM, it opens up space and, as HA is highly hygroscopic, it can trap high amounts of water (up to 100 times its weight (Day and Prestwich, 2002; Anderegg, Simon and Averbeck, 2014). Thus, HA determines the physical properties of the tissue. Moreover, due to HA's negative charge it can electrostatically bind

growth factors and cytokines resulting in local concentration gradients as well as in their activation (Kjeuin and Lindahl, 1991; Schlessinger, Lax and Lemmon, 1995).

HA acts as a signaling molecule which interacts with its receptors and co-receptors. By this it induces different pathways and thus determines cellular reactions (Weigel and Baggenstoss, 2017). Since HA is naturally polydisperse, especially when tissue is remodeled e.g. during development or wound healing it is difficult to lead back single effects to specific HA species.

1.3.2 Metabolismus

HA is synthesized directly into the extracellular space by three membrane-embedded HA synthases (HAS) expressed by dermal fibroblasts and basal keratinocytes, namely HAS1, HAS2 and HAS3 (Aya and Stern, 2014).

This makes the polymer special in comparison to other GAGs which are typically produced in the golgi (Aya and Stern, 2014). Even though structurally similar, the synthases differ within their kinetic characteristics as well as the size of their synthesized products. HAS1 and HAS2 synthesize HA of 2-4 MDa (Anderegg, Simon and Averbeck, 2014) while HA from HAS3 is characterized by varying sizes. In *in vitro* and *in vivo* experimental set-ups molecular sizes of 0.1 to 1 MDa and 0.2 to 2 MDa were found respectively (Itano *et al.*, 1999). It is assumed that the three similar HA synthases determine the different roles which HA plays in a wide variety of biological processes. Besides that, the activity of HAS depends further on posttranslational modifications such as ubiquitation, phosphorylation, and N-glycosylation (Vigetti *et al.*, 2009; Karousou *et al.*, 2010; Tammi *et al.*, 2011).

HAS1 is the main synthase involved in extracellular HA production in normal human keratinocytes (Malaisse *et al.*, 2014) while HAS2 predominates in dermal fibroblasts (Anderegg, Simon and Averbeck, 2014). Knock-out of HAS2 is lethal in mural embryos, but not in adult mice (Camenisch *et al.*, 2000; Spicer A P and Lee Tien J, 2004) indicating that the loss of one HAS enzyme can be compensated by the other synthases.

HA has a fast turn-over with its half-lifetime being tissue specific. Experiments in rabbits showed a half-life of radioactive-labelled HA in blood of three to five minutes, in skin less than 24 h and in cartilage one to three weeks (Anderegg, Simon and Averbeck, 2014). Degradation of HA occurs via hyaluronidases, or within the presence of reactive oxygen species (ROS). Besides that, smaller HA species can also be produced directly by HAS3 (Itano *et al.*, 1999). In humans, six different hyaluronidases exist, namely HYAL1-4, PH20 (= SPAM1) and HYAL-Phyal1 (Krupkova *et al.*, 2020). HA catabolism has been best investigated for HYAL1 and HYAL2 in human. These enzymes degrade HA via its hexosaminidic β (1-4) linkages (Lenormand, Amar-Bacoup and Vincent, 2011). Catabolism occurs intra- as well as extracellularly in a cluster of differentiation (CD44)-dependent manner (Culty, Nguyen and Underhill, 1992; Harada and Takahashi, 2007). First, CD44-bound HA is degraded by GPI-anchored HYAL2 to fragments of 10-20 kDa (Harada and Takahashi, 2007). After, further HA

degradation is achieved upon internalization of small HA fragments by intracellular HYAL1 in endosomes (Stern, 2004). The resulting tetrasaccharides are finally degraded by lysosomal exoglucosidases (Anderegg, Simon and Averbeck, 2014).

1.3.3 Hyaladherins – HA-binding proteins

Even though HA is a rather simple molecule, it has a vast effect on several cellular processes. This diversity is regulated on the one hand by the wide range of molecular sizes of HA and on the other hand by HA's many hyaladherins – proteins which interact with HA. The expression, affinity, specificity, their cellular localization and regulation is tissue- as well as cell-specific (Day and Prestwich, 2002).

Known receptors for HA are CD44 (cluster designation 44), TLR2 and 4 (toll-like-receptor) as well as HARE (HA receptor for endocytosis) and LYVE-1 (lymphatic vessel endothelial HA receptor 1) (Prevo *et al.*, 2001; Weigel and Baggenstoss, 2017). The latter two are mainly expressed in endothelial cells (Aya and Stern, 2014), whereas CD44 is highly expressed in basal layer keratinocytes (Frenkel, 2014). In the dermis, the proteoglycans aggrecan and versican are the most important hyaladherins. By forming linkages with HA they retain HA in the connective tissue, stabilize HA conformations and additionally interact with fibronectin and collagen (Hardingham, 1981; Sorrell *et al.*, 1999). All these listed hyaladherins share a Link module of about 93 conserved amino acid sequence which has been shown to be a common binding motif for HA. Other proteins belonging to the Link module superfamily are neurocan, brevican, stabilin-1 as well as TSG-6, whereas TSG-6 can form complexes with petraxin-3 or thrombospondin-1 (Anderegg, Simon and Averbeck, 2014). However, additional HA binding proteins have been identified which do not possess a Link module such as RHAMM (receptor for HA mediated motility) and Layilin (Bono *et al.*, 2001).

HA receptors in the skin are CD44, RHAMM and LYVE-1. LYVE-1 is selectively expressed during angiogenesis and mediates HA-induced leukocyte adhesion as well as HA degradation (Johnson *et al.*, 2007). RHAMM has a low expression in intact skin, which is induced during the repair process in dermal fibroblasts but is also increased in cancer cells (Tolg *et al.*, 2006). CD44 is expressed by dermal fibroblasts and keratinocytes. CD44 is the predominant receptor for HA in keratinocytes (Underhill, 1992). CD44 is a transmembrane spanning glycoprotein with an extracellular and intracellular binding domain. With its cytoplasmic domain, CD44 interacts via two adaptors (ezrin/radixin/moesin (ERM) proteins and ankyrin) with the cytoskeleton (Thorne, Legg and Isacke, 2004). It is encoded by 20 exons, for 10 exons alternative splicing has been described. Most of the changes predominantly affect the extracellular protein structure and are connected to CD44's different biological roles (Brown *et al.*, 2011). Intracellular CD44 is being connected to the cytoskeleton (Anderegg, Simon and Averbeck, 2014).

The minimum HA lengths being recognized by HA binding ligands are reported to be hexasaccharides (HA6) or decasaccharides (HA10) (Day and Prestwich, 2002). Several hyaladherins can bind to one HA polymer with a distance of three to five disaccharides (Day and Prestwich, 2002). For this reason, an HA receptor clustering within the cell membrane and subsequently the formation of signaling platforms can occur which transduces information within the cell, e.g. in case of CD44 to the cytoskeleton (Anderegg, Simon and Averbeck, 2014).

To sum up, the interaction of HA with its various hyaladherins highly depends on the size of HA, its conformation, which in turn might be affected by other, already bound hyaladherins as well as possible post-translational modifications of the relevant HA receptors. Additionally, as HA is polydisperse in natural systems, different HA sizes might compete for binding sites, adding another layer of complexity.

1.3.4 Chemical modifications of HA

Due to its high biocompatibility as well as its exceptional ability to absorb large amounts of water, HA has long been very interesting for biomedical applications such as a dermal fillers or vehicles for drug release. Quite often, HA has been chemically modified in order to improve its properties for the intended biomedical application. For instance, crosslinking HA polymer chains via their carboxyl groups led to a reduced degradation and, thus, higher stability of the resulting HA hydrogels (Yeom *et al.*, 2010). Different modifications sites are amenable within the polymer (Figure 5) to synthesize HA derivatives with a wide variety of functional groups (Schanté *et al.*, 2011). In our lab thiol as well as alkyne groups were introduced to immobilize HA on different surfaces. A functional group can be introduced either at the reducing end (the hydroxyl group) or within the chain (the carboxylic acid group) resulting in an end-alkylated/thiolated and respectively side-alkylated/thiolated molecule (Minsky, Antoni and Boehm, 2016). An end-alkylation introduces only one reaction group per molecule HA whereas a side-alkylation can introduce several alkyl groups in HA. Minsky *et al.* showed that both modifications maintain the accessibility of binding ligands. However, the latter is accompanied with an increase in 3D HA complexity as one and the same molecule might be modified at several sites and thus has more than only one possible interaction site with the surface and thus binding sites for cells might be covered. In contrast, a chemical modification of the HA polymer at the reducing end brings the advantage of a more linear conformation of HA (if LMW HA is utilized) and, thus, interrelates with a theoretical higher accomplishable molecule density on the surface as steric hindrance is reduced.

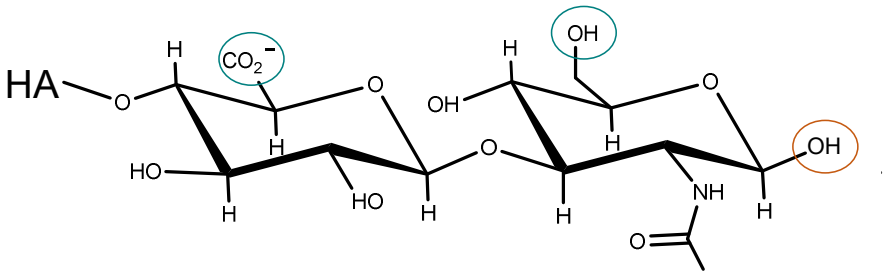

Figure 5: HA structure with indicated sites for chemical modification. Green: side modification sites; brown: end modification site

1.3.5 HA's role during cutaneous wound healing

Even though HA can be found in the whole human body, half of the total HA is located in the skin. Under physiological conditions, HA shows a MW of around 6000 kDa, concentrations are about 400-500 µg per g tissue (Cowman *et al.*, 2015). Even though the amount of HA is higher in the dermis than the epidermis, local concentrations of HA might be higher in the epidermis owing to the lower ECM space within cells in the tissue. The half-life of HA in human epidermis is less than 24 h (Tammi *et al.*, 1991).

As early as 1955, an increased mucopolysaccharide deposition – what is now known to have been predominantly HA –, has been observed in wound sites at the beginning of wound healing (Dunphy and Udupa, 1955). Today it is known that upon epidermal wounding, HA synthesis in dermal fibroblasts is activated through transcriptional activation of the HAS genes, especially HAS2 (Ghatak *et al.*, 2015; Koistinen *et al.*, 2017) Maytin, Chung and Seetharaman, 2004; Tammi *et al.*, 2005). Simultaneously with increased HA concentrations, HA fragments of low molecular mass (~5 kDa<MW<20 kDa) accumulate as a result of excessive digestion by hyaluronidases as well as ROS (Figure 6) (Aya and Stern, 2014). Eventually, the activity of HYALs decreases and new, HMWHA (>1000 kDa) is simultaneously synthesized, shifting the HA composition in the wound site from LMWHA to HMWHA (Figure 6).

HA participates in all phases of wound healing. During the inflammation phase it is involved in initiating the clotting pathway (Stern, Asari and Sugahara, 2006). Due to increased HA levels in the wound site and HA's hygroscopic properties, water accumulates, leading to tissue swelling (Gerdin and Hällgren, 1997). Thus, ligands for receptors on inflammatory cells are presented and migration paths open up for cells involved in wound healing (Toole, 2004). Small HA fragments together with growth factors attract fibroblasts to the wound site and the proliferative phase of wound healing is entered. More HA (of higher MW) together with other GAGs and collagens is newly synthesized by these fibroblasts resulting in the formation of granulation tissue (Frenkel, 2014). HA promotes keratinocyte migration and proliferation and thus re-epithelialization. While high HA levels in the ECM have been shown to induce proliferation and migration, low levels favor cell differentiation (Toole, Wight and Tammi, 2002). However, HA's effects on wound healing not only depends on its concentration but also on its

size (Tracy, Minasian and Caterson, 2016). Several studies were performed to attribute single cellular responses towards specific sizes or concentrations of HA within the framework of wound healing and re-epithelialization.

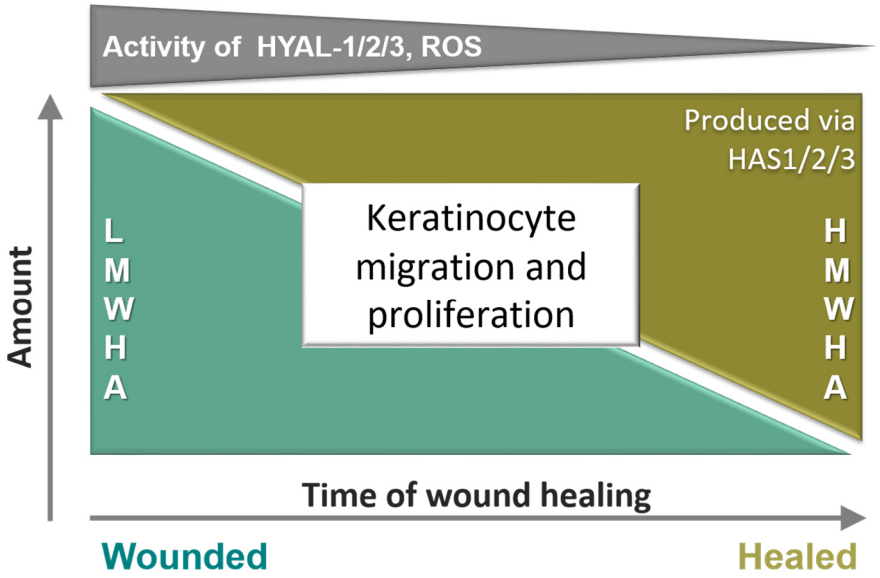

Figure 6: HA metabolism during wound healing. (LMWHA: low molecular weight HA; HMWHA: high molecular weight HA; HYAL: hyaluronidase; ROS: reactive oxygen species; HAS: HA synthase; adapted from Anderegg *et al.*, 2014).

Ghazi *et al.* compared the effect of size ranges of HA on keratinocyte migration. They used a human keratinocyte cell line and, after applying scratch assays, observed an increased wound closure and cell proliferation only when 100-300 kDA HA was applied at a concentration of 2 mg/mL (Ghazi *et al.*, 2012). D'Agostino *et al.* were one within a few which comprehensively compared a wide spectrum of different MWs of HA on keratinocyte migration. They also applied scratch assays of monolayers of a human keratinocyte cell line grown on collagen I-coated cell culture plastic surfaces. After treating cultures with 1 mg/mL HA solutions of different MW, they observed a proportional increase in migration velocity from 15 kDa on and a faster migration the higher the applied MW of HA was (D'Agostino *et al.*, 2017). Damodarasamy *et al.* compared the healing effect of exogenously applied 2, 250 and 100 kDa HA (10 ng/µL) on full-thickness wounds in mice. They found a significant improve on wound closure and collagen I and III deposition upon treatment with 250 kDa HA (Damodarasamy *et al.*, 2014).

Commercially available HA applications were deployed by Rüther *et al.* who treated full-thickness human skin cultures with 10 µL drops with 0.05 mg HA (of unknown MW) two times a day with an interval of 8 h with the result of increased re-epithelialization (Rüther *et al.*, 2017). Nyman *et al.* used a human *in vivo* cutaneous wound model and applied 0.5 mg HA in solution (of unknown MW) by intradermal injection and observed accelerated re-epithelialization (Nyman *et al.*, 2013). Studies regarding keratinocyte proliferation are contradictory to the effect of HA. Some authors claim that HA

improves proliferation (Tammi and Tammi, 1991; Gu *et al.*, 2010), whereas a more recent study did not found a proliferation enhancing effect of HA (Malaisse *et al.*, 2016).

Wound healing is a complex, multi-step process and HA has been shown to be involved throughout the whole process. However, different model systems (species, cell lines, tissues), different concentrations and sizes as well as additional ECM components make it difficult to compare independent studies with each other. To be able to comprehensively examine the role of HA on re-epithelialization it is thus crucial to first isolate the process where keratinocytes migrate and proliferate from the other wound healing phases. Second, HA is only one of many different ECM molecules. Because of that one has to provide an ECM environment where the interplay between HA with other ECM components can be controlled. And third, model systems need to be created which make it possible to transfer the experimental insights from a 2D cell culture system to a 3D tissue environment. And forth, even though HA is highly conserved across all species, the skin structures as well as the process of re-epithelialization varies even within mammals. Thus, to investigate the role of HA during re-epithelialization in human, it is vital to have a human model system.

1.4 Wound healing models

The following section will provide an overview on wound healing models developed to investigate the process of re-epithelialization. Different wound model systems to observe re-epithelialization have been established in the past. Commonly used are scratch assays, where a 2D monolayer is mechanically scratched to generate a wound site (Figure 7 A). This is a straight-forward method which is easy to perform without the need of special equipment or expertise. Scratch assays are especially suited if no special focus is set on the underlying ECM properties. In cases where a controlled, artificial ECM environment is applied to examine its effect on wound healing this method holds the unfavorable risk to not only remove cells but also to destroy the underlying ECM.

Alternatively, so called pseudo-wounds can be created via confinements which separate two adjacent cellular monolayers. Upon removal of the confinement two monolayers face each other with a clear cell-free line – the artificial wound site – in between them (Figure 7 B). The advantage is that the width of such artificial wound sites is independent from the handling and thus highly reproducible. However, those confinements still hold the potential risk to affect introduced surface characteristics. Additionally, this method only creates an artificial wound site and does not reflect a real wound as cells are not ruptured but only cultivated in a defined and enclosed area.

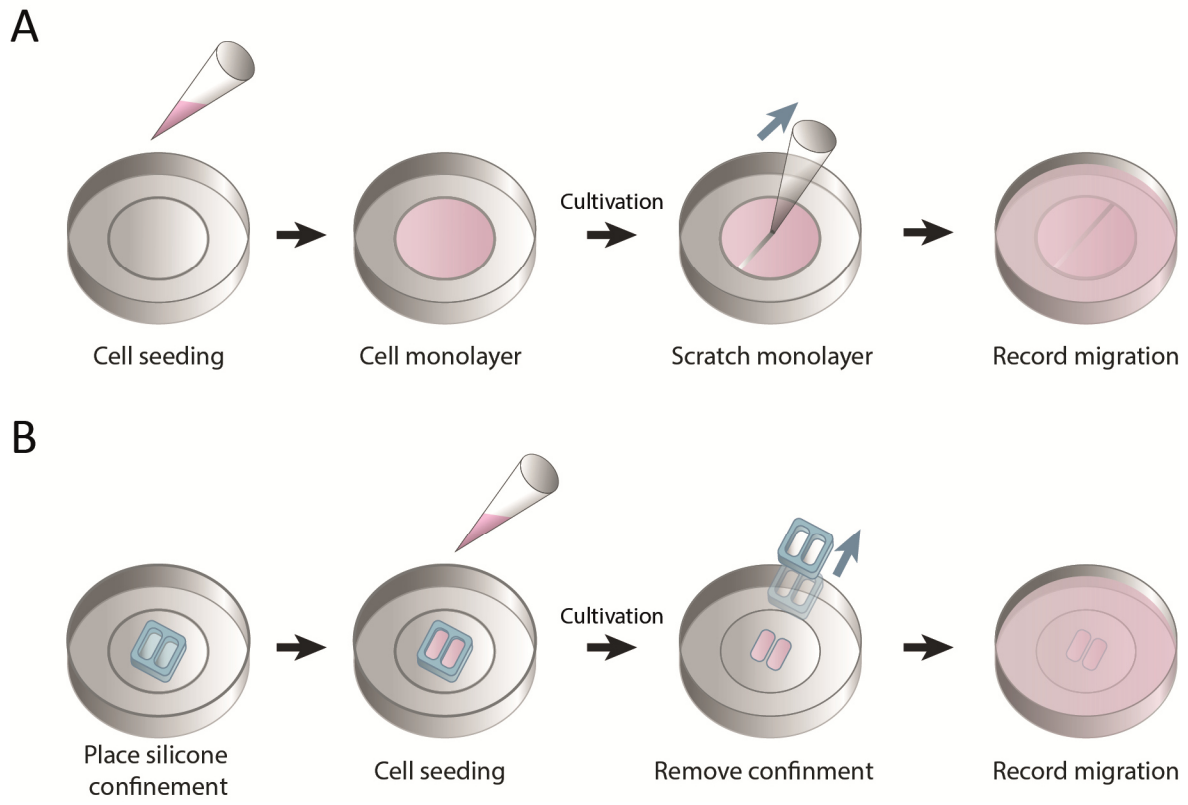

Figure 7: Wound healing models. (A) scratch assay, (B) pseudo-wound generation using a silicone-based confinement.

Other methods to generate two separated monolayers are chemical barriers, where caged adhesion molecules are utilized. Those molecules are non-adhesive upon cell seeding and can be un-caged by an external stimulus, e.g. light (Wirkner *et al.*, 2011). However, this approach requires special equipment to tightly control the localization of un-caging and as cells need to be first seeded in a defined area before a second area is photoactivated to mediate migration, this technique requires several steps. Additionally, currently only a few photoactivatable caged peptides such as cRGD are commercially available leading to low flexibility in experimental design.

By choosing cell lines or primary cells of interest one is flexible in the model system's origin for the before mentioned wound healing models. Primary cells, such as NHEK (normal human epidermal keratinocytes), are isolated from tissue and therefore maintain tissue-specific markers and functions. However, they have a finite life span and eventually lose those specific characteristics during passaging or terminally differentiate upon reaching confluence (Lee, Yuspa and Dlugosz, 1998). An alternative to primary cells are cell lines. HaCaT is a spontaneously transformed immortal human keratinocyte cell line, which has a near normal phenotype in contrast to cancer tissue derived cells lines (Boukamp *et al.*, 1988). HaCaT cells have been widely used for cell migration experiments (Ghazi *et al.*, 2012; D'Agostino *et al.*, 2017).

Most of the studies published on human wound healing and re-epithelialization have been performed in 2D systems. However, the epidermis is a multilayered 3D three dimensional tissue with

layered keratinocytes. Thus, cells cultivated in 2D lack the physical influence of bottom and top cells as well as the narrowed diffusion space within the surrounding ECM and their restricted access to nutrients. Also, it should be kept in mind that the keratinocytes in the epidermis are in various differentiation states showing specific characteristics. Many of the available 3D studies examining keratinocyte migration in wounds were conducted using rabbit or mural tissue systems (Pastar *et al.*, 2014). However, murine or rabbit wounds heal mainly via contraction whereas human wounds mainly heal via re-epithelialization (Dorsett-Martin, 2004). Additionally, since the human epidermis is much thicker compared to mice or rats and is less hairy, the gained information about the re-epithelialization process cannot be fully transferred in between these species (Rittié, 2016). Lately, partial- or full-thickness human skin cultures were developed where primary human keratinocytes are cultivated in 3D and eventually form a stratified epithelium. In case of full-thickness human skin cultures, also the dermis is reconstructed (Pastar *et al.*, 2014). Those models have been employed to elegantly examine in a two-step staining procedure the origin of migrating keratinocytes during re-epithelialization (Safferling *et al.*, 2013). For this, tissues were wounded and cultivated. After defined time points, samples were prepared for immunohistochemistry. Therefore, all reported data were end-point measurements with no live-cell imaging being performed. In contrast, Park *et al.* established an intravital imaging method to unravel keratinocyte behavior during re-epithelialization in genetically manipulated, living mice (Park *et al.*, 2017). However, such an approach cannot be transferred into humans.

1.5 Strategies to mimic the ECM – The bottom up approach

Re-epithelialization is a complex process where the ECM is highly remodeled throughout the healing process. However, available model systems make it difficult to tackle the contribution of the extracellular environment on re-epithelialization in human systems in real time. Even though re-epithelialization relies on the proliferation and migration of epidermal keratinocytes, this process is an orchestrated interaction with paracrine signaling molecules released by dermal fibroblasts (Werner, Krieg and Smola, 2007). A sophisticated ECM mimicking substrate close to the *in vivo* situation are so called dermal equivalents where primary dermal fibroblasts are encapsulated in a collagen I matrix. Human dermal fibroblasts (NHDF) remodel the collagen I matrix, measurable by a reduction in dermal equivalent (DE) diameter (Figure 8 A), and also secrete additional ECM components (Safferling *et al.*, 2013).

These dermal equivalents have been used as a substrate for commercially available epidermal full-thickness (containing epidermis and dermis) cultures (Safferling *et al.*, 2013). Even though being rather close to the *in vivo* situation, this approach does not dissect the effect of individual ECM components. Moreover, as dermal fibroblasts secrete continuously not only an undefined bulk of paracrine signaling molecules but – as the main producers of the ECM – ECM molecules, the ECM environment cannot be defined neither controlled under these conditions. Own experiments with 3D

human skin tissue cultures proved the importance of fibroblastic components on keratinocyte migration, as upon removal of dermal fibroblasts no migration occurred whereas upon addition of fibroblast conditioned medium migration was induced (data not shown).

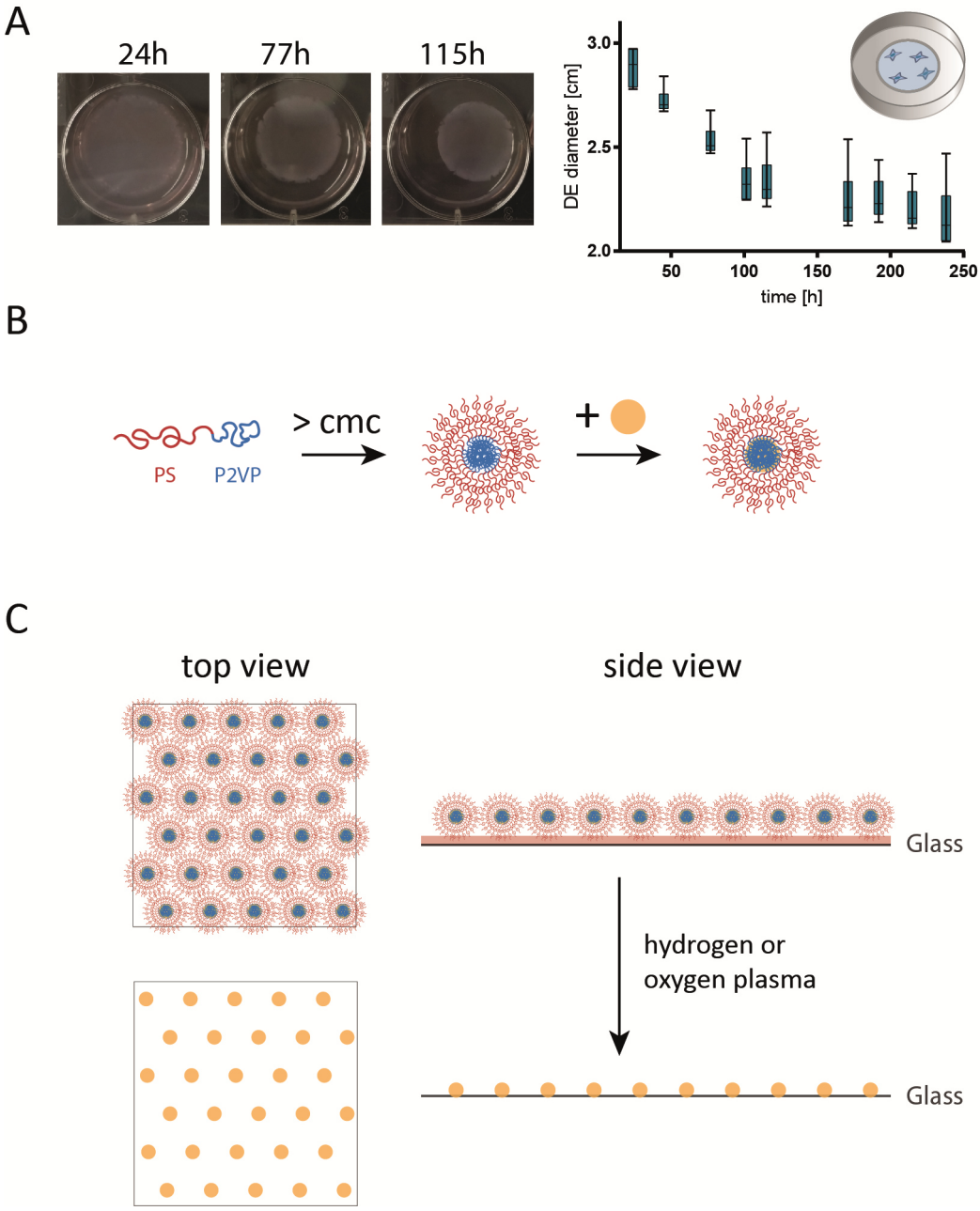

Figure 8: ECM mimicking models. (A) NHDFs (1 x 106 cells/mL) embedded in a collagen I matrix, also called dermal equivalents (DE) remodel the substrate eventually reducing the diameter of the DE over time. (B) Diblock-copolymers (hydrophilic block of poly-2-vinylpyridine (P2VP) and a hydrophobic block of polystyrene (PS)) form micelles upon exceeding of the critical micelle concentration (cmc). (C) The hydrophilic cores of these micelles are subsequently loaded with gold salts. Via spin coating loaded micelles self-assemble on glass surfaces in close-packing of equal spheres. Subsequent plasma treatment generates gold-nanostructured glass surfaces with gold-nanoparticles being arranged in a quasi-hexagonal order.

A simpler strategy to mimic the ECM in cell culture is to coat tissue culture dishes (plastic or glass) with either purified ECM components or a mixture of them (Kuschel *et al.*, 2006). In case of re-

epithelialization, collagen I-coated dishes are widely used (Ghazi *et al.*, 2012; D'Agostino *et al.*, 2017). This approach can also be used to coat glass surfaces thus enabling the application of sophisticated microscopic imaging methods. The ECM of those surfaces is adequately controllable and enables cells to process their 2D environment. Often, ECM proteins are purified from tissues, hence batch to batch variations cannot be excluded. Moreover, in cases where the contribution of single integrins towards a cellular response is analyzed, full protein surface coatings are not applicable (as more than one integrin heterodimer would be addressed).

Block-copolymer micellar nanolithography (BCML) offers a strategy to specifically immobilize binding ligands of ECM molecules on glass surfaces (Figure 8 B, C). By self-assembly of gold-loaded diblock-copolymers (hydrophilic block of poly-2-vinylpyridine (P2VP) and a hydrophobic block of polystyrene (PS)) on glass surfaces gold-nanostructured surfaces can be generated with gold-nanoparticles being arranged in a quasi-hexagonal order (Figure 8 C) (Kästle *et al.*, 2003). By varying BCML parameters like the block-copolymer length as well as its concentration, the distance between gold-nanoparticles can be tuned. Upon functionalization of those gold-nanoparticles with ligands of interest via thiol groups (gold-thiol interaction) the nature of the binding motif is controlled (Figure 9 A). The ligand density being presented to the cells is directly defined by the spacing of the gold-nanostructures. To make sure that cells solely interact with the binding motifs, the glass surface is passivated by covalently bound polyethylene glycol (PEG). Following this method, it was possible to prove that the spacing of binding ligands is decisive for cellular focal adhesion (FA) formation and cell spreading (Cavalcanti-Adam *et al.*, 2007). As binding motifs within the ECM are limited, often one and the same binding motif can be recognized by different integrins. Therefore, ligands of varying integrin-specificity have been chemically synthesized (Kapp *et al.*, 2017). cRGD is a widely used peptidomimetic to address integrins of the fibronectin binding family. c(RGDfV) is a modification of the preserved and highly conserved RGD peptide, the general binding motif of fibronectin which also occurs in other ECM molecules such as collagen I. c(RGDfV) has improved characteristics due to several modifications by which it shows a comparable low IC_{50} compared to other fibronectin addressing integrins (Kapp *et al.*, 2013). Furthermore, its D-amino acid residue as well as its cyclisation lead to a higher stability and activity, both essential for experiments spanning several days (Aumailley *et al.*, 1991; Mas-Moruno *et al.*, 2016).

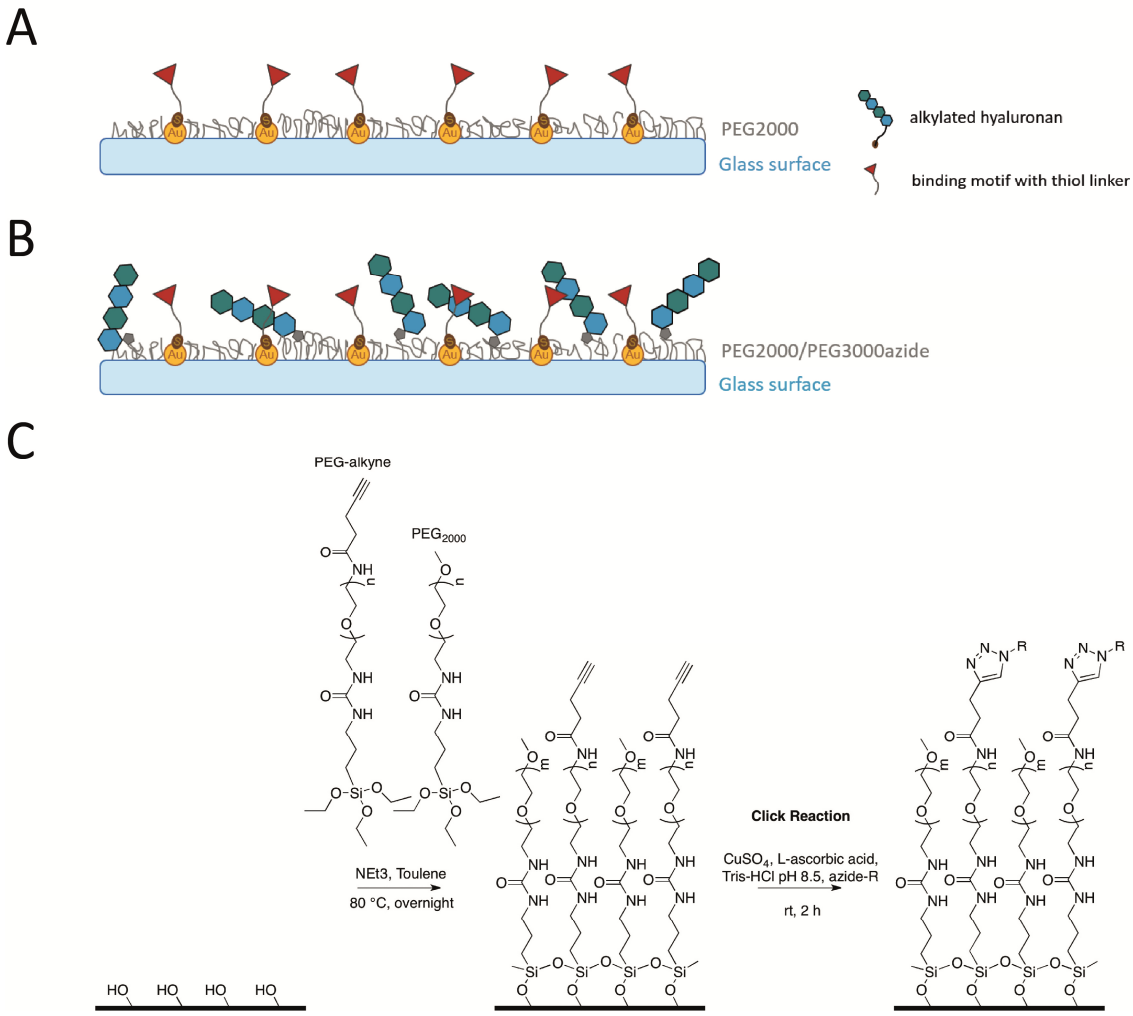

Figure 9: Strategies to generate (A) mono-functionalized or (B) bi-functionalized glass surfaces. (C) In order to generate bi-functionalized glass surfaces a click reaction is performed (chemical reaction adopted from Schenk *et al.*, 2014).

An extension of the described functionalized glass surfaces was made when glass surfaces were not only passivated with PEG2000 but with a mixture of two PEG species (Figure 9 B). By this it was possible to not only immobilize one binding ligand on the gold nanostructures but to introduce a second one and generate bi-functionalized glass surfaces via a click reaction with surface presented free alkyne or azide groups (Schenk *et al.*, 2014) (Figure 9 C). In first experiments cRGD was orthogonally presented with a synergy peptide dramatically improving the adhesive properties of such surfaces (Schenk *et al.*, 2014). Further experiments used bi-functionalized surfaces with adhesive ligands and the growth factor bone morphogenetic protein-2 (BMP-2) (Posa *et al.*, 2019). However, *in vitro* quarz crystal microbalance with dissipation (QCM-D) studies showed that not only peptides or proteins can be immobilized via click reaction but also end-alkylated HA (Minsky, Antoni and Boehm, 2016). Thus such bi-functionalized glass surfaces can be utilized within the bottom-up approach where single building blocks are assembled with the aim to stepwise model the complexity of the ECM.

1.6 Aim of thesis

Wound healing is a complex, multi-step process. To be able to comprehensively examine the role of HA on re-epithelialization, it is crucial to separate re-epithelialization as the process where keratinocytes migrate and proliferate from the other processes during wound healing. The effect of HA on re-epithelialization is controversial and comparability between independent studies is hampered as HA origin, applied HA concentrations, MW of HA as well as cell systems, substrate nature (glass, plastic) and ECM composition all differ from publication to publication. Therefore, I first aimed to comprehensively compare the effect of apical presented HA of different MW and concentrations within the framework of re-epithelialization using a human keratinocyte cell line.

With the aim to further reduce the complexity of the interplay of HA with other ECM molecules it is crucial to have a wound healing system consisting of a minimal number of components with the possibility to stepwise increase complexity. Following a bottom-up approach, I employed bi-functionalized glass surfaces and altered their functional groups: Only HA and a second, integrin-addressing binding ligand were presented on an otherwise passivated background. The stages of wound healing are represented by the ECM environment. With the purpose to integrate dynamic ECM changes, as they occur with proceeding wound healing, I established a two-staged ECM model which is compatible with the presented bi-functionalized glass surfaces. Combining both systems, a human two-stage ECM wound healing model was created which can be applied in 2D cell culture as well as 3D tissue systems. The developed model has the potential to reveal HA's signaling role in cooperation with other ECM molecules on re-epithelialization in future applications.

2 Material and Methods

1.1 Materials

1.1.1 Hyaluronic acid

All hyaluronic acid (HA) applied was purchased as Sodium Hyaluronate, research grade from Lifecore Biomedical (Table 2).

Table 2: HA used in this thesis

MW [kDa]	LOT	Cat.No.
5	26570	HA5K
60	26428	HA60K
700	24367	HA700K
1800	26489	HA2M

Table 3: Osmolarity and pH utilized HA solutions (pH measured with Orion Star A211, Thermo Scientific; and osmolarity measured with Osmomat O30, Granotec).

HA [kDa]	FBS [%]	Osmolarity [osmol/L]	pH
-	1%	0.387	8.03
5	1%	0.351	7.85
60	1%	0.391	7.99
200	1%	0.380	7.99
700	1%	0.352	8.09
1800	1%	0.369	7.98
-	2.50%	0.406	8.05
60	2.50%	0.426	8.06
200	2.50%	0.406	8.03
700	2.50%	0.393	7.99
-	10%	0.390	8.07
5	10%	0.345	8.01
60	10%	0.386	8.18
200	10%	0.381	8.11
700	10%	0.346	8.07
1800	10%	0.372	8.09

For cell culture experiments HA was weighted under sterile conditions and the respective volume of dulbecco's modified eagle's medium (DMEM; # 41966, Thermo Fisher) was added to a final concentration of 1 mg/µL. Solutions were let sit overnight at 4 °C to ensure HA was fully dissolved. The next day 1 % fetal bovine serum (FBS; Sigma Aldrich) was added and serial dilutions of 5/50/500/1000 µg/mL of HA solutions were prepared. The solutions were pre-warmed and CO_2 equilibrated in the incubator before being added on the confluent monolayers of HaCaT cells. The pH and osmolarity HA solutions was determined to confirm physiological conditions (Table 3).

1.1.2 Antibodies

Primary antibodies

All primary antibodies used in this thesis are listed in Table 4.

Table 4: Primary antibodies used in this thesis

Target protein	Species	Dilution	Order number	Company
collagen I	α-mouse	1:1000	C 2456	Sigma-Aldrich
vinculin	α-mouse	1:400	V9131	Sigma-Aldrich
CD44	α-rat	1:1000	217594	Sigma-Aldrich

Secondary antibodies

All secondary antibodies used in this thesis are listed in Table 5.

Table 5: Secondary antibodies used in this thesis

Target species	Fluorophor	Dilution	Order number	Company
mouse	Alexa488	1:2000	A-11011	Thermo Fisher Scientific
rat	Alexa647	1:1000	A-21247	Thermo Fisher Scientific

Fluorescence stainings

All fluorescence affinity binders used in this thesis are listed in Table 6.

Table 6: Fluorescence stainings used in this thesis

Name	Fluorophor	Dilution	Order number	Company
Phalloidin	TRITC	1:500	P1951	Sigma-Aldrich
DAPI	-	1:000	D9542	Life Technologies

1.2 Cell Culture

All experiments involving living cells were performed under sterile conditions using a flow hood (HareSafe, Thermo Fisher Scientific).

1.2.1 Cultivation of HaCaT cells

The HaCaT cell line is a spontaneously immortalized human epidermal cell line (Boukamp *et al.*, 1988). Cells were cultured in T25 (# 50-809-257, Sarstedt) and respectively T75 (# 50-809-261, Sarstedt) culture flasks in DMEM (#41966, Thermo Fisher) supplemented with 10 % FBS (Sigma-Aldrich) at 37 °C in 5 % CO_2 and water saturated atmosphere (HeraCell240, Thermo Fisher Scientific). Medium was renewed every 3 to 4 days. Upon reaching 90-100 % confluence cells were splitted. For this cells were washed twice with phosphate-buffered saline (PBS; # D8537, Sigma-Aldrich) without Ca^{2+} and Mg^{2+}, before being incubated with trypsin/EDTA (# 25300062, Life technologies) for 8-10 min at 37 °C to withdraw bivalent cation complexes by EDTA on the one hand and on the other digest cell surface proteins to induce cell detachment. Trypsin digest was stopped by adding serum supplemented DMEM and the cell suspension was transferred in a falcon tube and centrifuged at 300 xg for three minutes. The supernatant was removed and the cell pellet re-suspended in 6 mL fresh medium. For sub-cultivation the cell suspension was either diluted 1:4 for a 75 cm^2 flask or by seeding 40000 cells/cm^2. Cell number was determined using a Neubaur chamber. The amount in seeded cells for experiments were stated accordingly. All cell experiments were carried out using passages of 15-28. Regularly mycoplasm tests confirmed mycoplasma-free culture conditions.

1.2.2 Cultivation of NHEK

NHEK (normal human epidermal keratinocytes) were purchase from Promocell. Cells were cultured in T25 (# 50-809-257, Sarstedt) and respectively T75 (# 50-809-261, Sarstedt) culture flasks in Keratinocyte Media 2 (# C-20111, Promocell) at 37 °C in 5 % CO2 and water saturated atmosphere (HeraCell240, Thermo Fisher Scientific). Medium was renewed every 3 to 4 days. Before reaching confluence cells (70-90 %) were splitted. For this cells were washed twice with phosphate-buffered saline (PBS; # D8537, Sigma-Aldrich) without Ca2+ and Mg2+, before being incubated with PromoCell DetachKit (# C-41200, Promocell) for 8-10 min. Trypsin digest was stopped by adding the Trypsin

Neutralization Solution. The cell suspension was transferred in a falcon tube and centrifuged at 220 xg for three minutes. The supernatant was removed and the cell pellet re-suspended in 1 mL fresh medium. For sub-cultivation the cell suspension was either diluted 1:4 for a 75 cm2 flask or by seeding 5000 cells/cm^2. Cell number was determined using a Neubaur chamber. All cell experiments were carried out using passages from 3 to 5.

1.3 Two-stage ECM model

1.3.1 2D epidermal models

For the generation of 2D epidermal models polycarbonate microporous membranes clamped in polystyrene inserts (# 140620, Nunc) were collagen I coated (# R011K, Gibco) using the Coating Matrix Kit (# R011K, Gibco). The coating matrix and the dilution matrix were mixed directly prior to usage in a ratio of 1:50. Per membrane with an area of 0.47 cm^2 a total coating matrix volume of 70 µL was applied and evenly distributed over the surface. Polycarbonate membranes were incubated for 30 min at RT and excess solution was removed by aspiration. Subsequently cell-culture inserts (#80209, Ibidi) were placed in 6-well plates and 30 x 10^5 HaCaT cells were seeded in 150 µL DMEM (# 41966, Thermo Fisher) with 10 % (v/v) FBS (Sigma Aldrich). To ensure sufficient nutrition supply each well was filled with 1 mL of DMEM supplemented with 10 % (v/v) FBS. Depending on the initial seeding number membranes were usually cultivated for 1-4 days before being used for experiments.

1.3.2 Membrane release and wounding

Membranes were released from the polystyrene inserts (#80209, Ibidi) using an 8 mm biopsy puncher (# 130805, Stiefel). In cases where the membrane couldn´t be released completely from the insert, a scalper was additionally used. Upon membrane release, membranes were wetted with cell culture medium to prevent drying. Membranes were cut in the middle in one movement with a rounded scalper before being placed on surfaces of interest. When working with polycarbonate membranes (# 140620, Nunc). To avoid scratching the monolayer on the membrane plastic tweezers were used. Punched wound sites were achieved by using biopsy punchers with 1 mm or 2 mm diameter.

1.3.3 Fixation strategies

Fixation with collagen I glue

Collagen I glue (# 47256, Serva) was prepared (see1.4.3) and 1 or 2 µL drops were distributed on (3-Aminopropyl)triethoxysilane (APTES) activated surfaces (see 1.4.1). 2D epidermal models were quickly transferred and placed on top of the collagen I glue drops. Collagen I glue polymerized for 10 min in a cell culture incubator. After, cell culture medium was added on top of 2D epidermal models.

Mechanical fixation via PDMS molds

Polydimethylsiloxane (PDMS; #101697, Sylgard®) was prepared by mixing 90 g PDMS and 10 g crosslinker solution. Solutions were centrifuged at 4.4 rpm to remove bubbles and stored at -20 °C until usage. To fabricate customized PDMS molds PDMS solution was poured in cell culture dishes (# D35-20-0-N, Cellvis). The dishes were put for 1.5 h in a desiccator to remove remaining bubbles. After, PDMS was polymerized for 2 h at 60 °C. Next, PDMS was released for the cell culture dish, placed on a mask with the outlines of the mold and excess PDMS was manually removed using a scalper. PDMS molds were disinfected in 70 % EtOH and dried before being used. Membranes were placed on substrates of interest, and the PDMS mold was placed on top carefully taking care that the membrane was not shifted with the cut side in the center.

Mechanical fixation via teflon molds

Customized teflon molds were designed as 3D model using the software AutoCAD2019 and were kindly fabricated by the PCI workshop according to the 3D model. Teflon molds were sterilized for cell culture application by autoclaving and stored at RT until use. Teflon molds were first placed in 6-well plates carrying the surfaces of interest and the area, where the membrane should be placed was marked with a non-permanent marker. The mold was removed and membranes were carefully placed with plastic tweezers on the substrate. In case that the membrane positioning needed to be corrected, membranes were always rather pushed than pulled to avoid any interference with the substrate. After, teflon molds were place on top of the membranes and 1 mL of DMEM (# 41966, Thermo Fisher) supplemented with 10 % (v/v) FBS (Sigma Aldrich) was added. Weight was applied for 10 min to kill cells being directly under the contact area with the teflon mold before 8 (first teflon mold generation), and respectively 6 mL (second teflon mold generation) of cell culture medium were added to fully cover the molds.

1.4 Surface Preparation

1.4.1 Cleaning and activation of glass surfaces

Coverslips (24x24 mm, # 873, Roth) or glass bottom dishes (# D35-20-0-N, Cellvis) were cleaned by sonication in 70 % (v/v) EtOH for 3 min (to remove fat), rinsed with deionized water (dH_2O), dried with nitrogen stream treated with 0.1 M sodium hydroxide solution for 5 min followed by another washing step with dH_2O. For activation coverslips were treated with 4 % (v/v) APTS (3-aminopropyl-triethoxysilane, # A3648, Sigma Aldrich,) in iso-propanol for 5 min, followed by washing with dH_2O and short drying before being treated with 1 % (v/v) gluraraldehyde solution (# 23114.01, Merck Microscopy) in dH_2O for at least 30 min. Finally, coverslips were washed thoroughly with dH_2O, dried with nitrogen air and stored upon usage (max 4 weeks).

1.4.2 Preparation of homogeneous protein coatings

For homogeneous protein coatings protein solutions are diluted in PBS (# D8537, Sigma-Aldrich) according to Table 7. For collagen I coating the coating matrix kit from Gibco was employed (# R011K, Gibco) according to the manufacturer. In short, for 1 cm^2, 0.667 of the Coating Matrix was applied. Fibronectin (# F2518, Sigma-Aldrich) and laminin 332 (# LN332, Biolamina) were applied at 5 µg/cm^2. UVO activated coverslips (24x24 mm, # 873, Roth) were placed upside-down on a drop of 40 µL coating solution. Coverslips and cell culture dishes (# D35-20-0-N; Cellvis) were coated at 4 °C overnight in a humidity chamber.

Table 7: Dilution of coating proteins

Coating protein	Protein solution	Dilution medium/PBS
Collagen I	3.84	26.16
Fibronectin	28.8	11.2
Laminin 332	17.28	22.72

1.4.3 Preparation of collagen I glue and collagen I gels

All steps for collagen I gel polymerization were performed on ice and solutions were cooled down before usage. Gels were prepared by mixing 700 µL of Collagen R solution (# 47256, Serva) with 100 µL minimum essential medium (MEM; # 2430-020, Gibco) in a sterile glass bottle. Subsequently, the pH was adjusted adding dropwise 1 M NaOH until the solution color turned into strawberry red (at pH 7) and filled up to 100 µL with dH_2O before 100 µL of PBS (# D8537, Sigma-Aldrich) are added. PDMS (#101697, Sylgard®) molds (Ø 12 mm PDMS ring, disinfected with 70 % EtOH) were placed on top of activated (see 1.4.1) glasscoverslips (24x24 mm, # 873, Roth) and were filled with 200 µl of collagen mix. Coverslips are carefully swayed to evenly cover surfaces with collagen I solution. Gels polymerized for 20 min in a cell culture incubator. After, gels were equilibrated with respective cell culture medium overnight at 37 °C and 5 % CO_2.

1.4.4 Preparation of gold-nanostructured surfaces via block copolymer micellar nanolithography

Glass coverslips (24x24 mm, # 873, Roth) were nanostructured with an average particle spacing of 52 ± 9 nm via block copolymer micellar nanolithography (BCML) as previously described (Spatz *et al.*, 2000; Lohmüller *et al.*, 2011).

Preparation of polymer solutions

A polystyrene-b-poly(2-vinylpyridine) (PS-b-P2VP) diblock copolymer (PS unit number: 501; P2VP unit number: 323; Polymer Source, Quebec, Canada) was dissolved in ortho-Xylene (5 mg/ml; 1.08298, Sigma-Aldrich**)** and stirred for 24 h at RT to ensure uniform diblock copolymer micelle formation with a hydrophobic PS coat and a hydrophilic P2VP core. The next day the amount of gold salt $HAuCl_4$ was determined to achieve a loading of 0.25 using equation (1):

$$\mathrm{m(HAuCl_4)} = \frac{\mathrm{m(Polymer)} \cdot \mathrm{M(HAuCl_4 \cdot 3H_2O)C} \cdot \mathrm{P2V}P_{units} \cdot \mathrm{L}}{\mathrm{M(Polymer)}} \quad (1)$$

with m= mass [g]; L= loading, $P2VP_{units}$= the number of P2PV units, M= molecular weight [g/mol].

Gold salt, which has low solubility in organic solvents is added to the micelle solution and stirred again for 24 h at RT to mediate diffusion of gold-precursors into the hydrophilic micelle P2VP core. Polymer solutions can be stored for several weeks under permanent stirring at RT.

Spin coating

Coverslips (24x24 mm, # 873, Roth) are cleaned in a mixture of 3:1 H_2SO_4 and H_2O_2. For this, coverslips are placed in teflon holders and transferred into a beaker. Next, H_2SO_4 and H_2O_2 are added. By this H_2SO_5 is produced, one of the strongest oxidants known. Glasses are incubated for at least 1 h at RT to remove any organic oxidants and glass surfaces activation. Surfaces are thoroughly washed with dH_2O and stored in dH_2O upon usage.

By spin coating of cleaned and activated glass coverslips with the polymer solution by centrifugal force generates uniform monomicellar films on the glass surface. For this, cleaned and activated coverslips are placed on the rotary plane of the spin coater and vacuum is switched on to tightly fixate the glass. Next, the spinning is activated and 25 mL of polymer solution are placed in the center of the coverslip. The spinning time per glass slide was 1 min at 9000 rpm for the surfaces. During this procedure, the organic solvent (ortho-Xylene) evaporates and gold loaded micelles arrange in a quasi-hexagonal pattern on the glass surface. Subsequent hydrogen plasma treatment (W10, 350 W, 0.4 mbar; 45 min) removes the entire polymer coat and reduces the gold from Au^{3+} to Au^0, resulting in a quasi-hexagonal gold nanoparticle pattern on the glass surface.

Quality control of BCML surfaces

For each new polymer solution and batch production, the inter-particle spacing as well as the size and the degree of hexagonality of gold-nanoparticles on the glass surface are determined. For this, test slides are sputter coated with a thin conductive layer of graphite before being analyzed by scanning electron microscopy (SEM). Hexagonality and average distance in between nanoparticles was determined by applying a customized IPL script (Böhm, 2008).

1.4.5 Passivation of surfaces

Basic passivation with PEG2000

The area between the gold-nanoparticles on the gold-nanostructured glass coverslips (24x24 mm, # 873, Roth) was passivated with a thin layer of polyethylene glycol (PEG) to prevent unspecific cell adhesion or protein adsorption. For this, nanostructured glass coverslips are re-activated for 10 min with ozone and then transferred (using a customized glass holder) pre-heated 80 °C 5:1:1 solution of dH_2O , 25 % ammonia (# 1.05432 Supelco**)** and 30% hydrogenperoxide (# 1.07209, Supelco**).** After, the glass holder is rinsed thoroughly with dH_2O and glass coverslips are dried in nitrogen flow. The glass holder is placed in a nitrogen flushed Schlenk containing 40 mL dried degassed toluene (# 10477172, FisherScientific) at 80 °C. Some drops of distilled degassed triethlyamine (# 11452984, FisherScientific) are added together with 3-5 mg of PEG2000 ($(CH_3O)_3Si$-PEG2000; # MF001020-2K, Biochem PEG Scientific) and allowed to react overnight at 80 °C. The next day surfaces are cleaned twice with ethylacetate, twice with methanol and shortly rinsed with dH_2O. The glass coverslips are dried with nitrogen air and used directly or stored at 4 °C upon usage.

Passivation with mPEG2000 and PEG3000azide

The passivation protocol performed was accordingly to the "Basic passivation with mPEG2000" protocol. Instead of mPEG2000silane alone a mixture of mPEG2000 (# MF001020-2K, Biochem PEG Scientific) and PEG3000azide ($(CH_3O)_3Si$-PEG3000-N_3; # 133000-5-71, Rapp Polymere) in different ratios for 0 %, 10 % and 50 % PEG3000azide to PEG2000 (# MF001020-2K, Biochem PEG Scientific) is dissolved under inert atmosphere (Table 8). A total concentration of 50 mM PEG mixture was applied in 50 mL of toluene.

Table 8: Applied PEG2000silane and PEG3000azide for different mol% ratios.

mol% PEG3000azide	PEG2000silane	PEG3000azide
0%	50 mg	0.0 mg
10%	45 mg	7.5 mg
50%	25 mg	37.5 mg

1.4.6 Functionalization of gold-nanostructured surfaces

Basic functionalization of PEG2000 passivated gold-nanostructured surfaces

Gold nanostructured and passivated glass surfaces were functionalized with peptides carrying a binding motif to address cellular integrins to enable cell adhesion and a thiol linker to immobilize peptides on gold nanoparticles. For this passivated glass cover slips are incubated with the respective peptide (25 µM in MilliQ; Table 9) for 4 h at room temperature. Passivated coverslips (24x24 mm,

873, Roth) were placed upside-down on a drop of 40 µL peptide solution in a humidity chamber and incubated for 4 h at RT, or overnight at 4 °C. To remove excess and unbound peptides surfaces are subsequently washed thrice with dH_2O and once with PBS (# D8537, Sigma-Aldrich) for 30 min directly before application. Surfaces are dried with nitrogen air.

Table 9: Overview of used peptides. All peptides were purchased from PSL (Peptide Specialty Laboratories GmbH, Germany).

Binding ligand	Mass (MH+) [Da]
c(RGDfE)-PEG6-Cysteamin	1027.50
EPDIM-PEG6-Cysteamin	998.50
3-Mercaptopropionic acid-PEG6-EPDIM	999.50

Functionalization of bi-functionalized PEG2000/PEG3000azide surfaces

Bi-functionalized glass surfaces are generated as first described by Schenk *et al.* (Schenk *et al.*, 2014). For this, surfaces are first passivated with PEG2000/PEG3000azide (# MF001020-2K, Biochem PEG Scientific/ # 133000-5-71, Rapp Polymere) as described before. After, HA is immobilized on the azide group of the PEG3000azide via a copper(I)-catalyzed azide alkyne cycloaddition (CuAAC, click reaction). The click reaction mix is generated according to Table 10 with $CuSO_4$ added at the end. Stock solutions of ascorbic acid are prepared fresh directly before the reaction. The same applies for alkylated HA. Per one glass coverslip (24x24 mm, # 873, Roth) 100 µL of reaction mix is applied. The reaction is carried out protected from light for 2 h at RT. After, the coverslips are washed two times in beakers filled with dH_2O and then dried with nitrogen air. Next, binding ligands with a thiol linker (#, Hersteller?) are bound to gold-nanoparticles as described above overnight at 4 °C . The next day, the slides are washed twice fast with dH_2O and once with dH_2O for 5 min the ultrasonic bath, before the slides are washed trice for 40 min with dH_2O, once 30 min with PBS (# D8537, Sigma-Aldrich) and dried with nitrogen air. Circles were cut out of 6- or 24-well plates and bi-functionalized glass surfaces were placed from the top and glued using a two-component glue.

Table 10: Click reaction mix.

Substance	End-concentration
Ascorbic Acid	100 mM
$CuSO_4$	1 mM
alkylated HA	1.25 mg/mL
Tris buffer pH 8.5	100 mM

1.5 Assays

1.5.1 Adhesion assays

Adhesion assay on glass surfaces

In order to determine cell adhesion on different surfaces 5 x10^4/cm^2 HaCaT cells or 1.5x10^4 cells/cm^2 NHEK were seeded in DMEM (# 41966, Thermo Fisher) supplemented with 1 % (v/v) FBS (Sigma Aldrich) and cultivated for 24 h on respective surfaces. Cell adhesion and subsequent spreading was observed by time-lapse live-cell imaging for a total recording time of 30 h. One image per hour was taken.

1.5.2 Proliferation assay

Cell proliferation was determined using the Molecular Probes™ Click-iT™ EdU Alexa Fluor™ 555 Kit (# C10338, Invitrogen) according to the manufacturer's protocol. This assay works via incorporation of the modified thymidine analogue EdU in the DNA. Only cells that underwent mitosis incorporate EdU which is visualized upon end-point staining.

For the proliferation assay 74 x 10^3 and 148 x 10^3, respectively HaCaT cells/cm^2 were seeded in one well of a 96-well plate (or 24-well plate) and cultivated for 24 h in DMEM (# 41966, Thermo Fisher) supplemented with 10 % (v/v) FBS (Sigma Aldrich). The next day cell culture medium was removed and cells were washed once with PBS (# D8537, Sigma-Aldrich). Cells were treated with 200 µL (1 mL) per well HA solutions of 5, 60, 700 and 1800 kDA at a concentration of 0, 5, 50, 500 and 1000 µg/mL were solved in DMEM (# 41966, Thermo Fisher) supplemented with 1 % (v/v) FBS (for details be referred to 1.1.1) and EdU (1:1000). In order to track cell confluence, brightfield images were taken for every condition after 0, 24 and 48 h. After 5, 24 and 48 h cells were fixed with 50 µL (500 µL) 4 % (v/v) paraformaldehyde (PFA, # P6148, Sigma Aldrich) for 15 min at room temperature (RT). Cells are washed with PBS before they were permeabilized with 50 µL (500 µL) 0.5 % (v/v) Triton X-100 (# X100RS; Sigma-Aldrich) in PBS for 20 min. After, cells are blocked with 3 % (v/w) bovine serum albumin (BSA; # 8076, Roth) in PBS while the click reaction buffer is prepared (Table 11).

Table 11: Preparation of click reaction buffer (volumes are indicated for 1 single well).

Substance	Volume [µL]
Reaction buffer	43 (1:10 diluted in PBS)
$CuSO_4$	2
Alexa Fluor	0.12
Buffer additive	5 (1:10 diluted in PBS)

Click reaction was performed with 49.8 µL (200 µL) click reaction buffer per well for 30 min at RT. Samples were washed once with PBS and a Hoechst (stock: 10 µg/mL) staining is performed by diluting the stock solution 1:1000 in 3 % (v/w) BSA in PBS.

Cells were imaged with a fluorescence microscope as described in 1.7.4. The relative proliferation rate was determined by counting EdU positive and Hoechst stained cell nuclei within a recorded area of 380 x 380 µm and dividing the number of EdU positive cells by the total cell number (number of Hoechst stained cells).

1.5.3 Migration assays

Confinement-based migration assay

Artificial wound sites were generated by using commercially available two-chambered cell-culture inserts (#80209, Ibidi). For this, UV-ozone (UVO; UV-ozone Pro Cleaner™, BioForce Nanosciences)-activated glass-bottom dishes (# D35-20-0-N; Cellvis) were collagen I -coated (# R011K, Gibco) over night at 4 °C. Subsequently, two-chambered cell-culture inserts were placed on top and 7 x 10^4 HaCaT cells were seeded in each chamber in DMEM (# 41966, Thermo Fisher) supplemented with 10 % (v/v) FBS (Sigma Aldrich) and cultivated for 24 h. Next, cell-culture inserts were carefully removed and remaining medium was removed washing twice with PBS (# D8537, Sigma-Aldrich). HA solutions of different molecular weight and concentration were added (see 1.1.1)

Migration was recorded by taking images of the artificial wound site after 5, 24 and 48 h with a Leica DMi-1 with a 10x objective. To compare initial cell density between independent experiments overviews of the confluent monolayer upon migration initiation were taken with an 40x objective.

Cell migration was analyzed by using a specifically trained classifier for the WEKA ImageJ plugin for automated segmentation of cell-covered and cell-free area (Arganda-Carreras *et al.*, 2017). Then, the size of the cell-free area was semi-automatically determined using a self-written ImageJ script. The reliability of the segmentation and cell-free area detection was evaluated prior to analysis by comparing the determined area of the semi-automatically analysis with manually determined analysis.

Scratch assay

7 x 10^3 HaCaT cells/cm^2 were seeded in one well of a 12-well plate in DMEM (# 41966, Thermo Fisher) supplemented with 10 % (v/v) FBS (Sigma Aldrich) and cultivated overnight until full confluence was reached. The next day medium was removed and a scratch was applied with a 200 µL pipette tip. Cell debris was removed by washing twice with PBS (# D8537, Sigma-Aldrich). HA solutions were prepared as described before (for details be referred to 1.1.1). HA solutions were added (900 µL/well) and cell migration was recorded after 5, 24 and 48 h by widefield microscopy.

In vitro wound healing assay

2D epidermal models (1.3.1) were released with a 8 mm biopsy puncher or a scalpel from the polystyrene insert and wounded by cutting with a scalpel. Membrane halves were transferred on surfaces of interest and fixated with customized teflon molds (1.3.3). Cell migration emerging from the cut side of the membrane was monitored at 37 °C and 5 % CO_2 within an incubator staged over a Leica DMi8 inverted fluorescent microscope (see 1.7.4). Images were taken every hour for a total image acquisition of 48 h. To visualize the whole wound site five non-overlapping tiles of optical fields were imaged. Image analysis was performed using a customized semi-automatical Fiji (Schindelin *et al.*, 2012) makro, kingly programmed by the ZMBH Imaging Facility. First, brightness and contrast was automatically adjusted. Next, images were rotated to correct the tilted cut side of the membrane. After, the migration front was manually determined. The makro measured total migration area.

1.6 (Indirect) Immunofluorescence

Cells medium is aspirated and cells are washed three times with PBS (# D8537, Sigma-Aldrich) and fixed with 4 % PFA (# P6148, Sigma Aldrich) solution for 15 min at RT, followed by PBS washing for three times. Cell monolayers were permeabilized with 0.1 % (v/v) Triton X-100 (# X100RS; Sigma-Aldrich) in PBS for 10 min at RT, washed again three times with PBS and blocked with 1% (w/v) BSA (# 8076, Roth) in PBS for 5-30 min at RT. Primary antibodies were diluted in 1 % (w/v) BSA in PBS and applied for 1 h at RT or overnight at 4 °C. Cells are washed thrice with PBS and are incubated with secondary antibodies diluted in 1 % (w/v) BSA in PBS for 1 h at RT followed by another PBS washing (3x). Samples are sealed with parafilm and stored in PBS at 4 °C upon imaging.

1.6.1 Visualizing collagen I glue

To visualize the localization of collagen I glue (# 47256, Serva) under the membranes, glass bottom dishes (#D35-20-0-N, Cellvis) were APTS-activated (see 1.4.1) and membranes were glued on top using collagen I glue (see 1.4.3). Collagen I was visualized by indirect immunofluorescence as described before, with no PFA fixation or permeabilization. Full membranes were recorded in tiles with a 10x objective (Zeiss AxioObserver Z1, see 1.7.1).

1.6.2 Cellular coverage of polycarbonate membranes

For determining HaCaT cell spreading on collagen I-coated (# R-011-K, Gibco) or non-coated polycarbonate membranes (# 140620, Nunc) 1.9 x 10^4 cells per membrane were seeded and incubated overnight. To visualize the nuclei and actin PFA (# P6148, Sigma Aldrich) fixation and permeabilization were performed as described before. After, actin was visualized using phalloidin, diluted 1:500 and 4′,6-diamidino-2-phenylindole (DAPI), diluted 1:1000 in 1 % (w/v) BSA (# 8076, Roth). Staining was

performed for 1 h at RT followed by thrice washing with PBS (# D8537, Sigma-Aldrich). Images were taken using a Delta Vision (DV) system (Applied Precision Inc.) on an Olympus IX inverted microscope, equipped with a cooled CCD camera and a 10x/0.3 NA (Olympus) objective. Cell area was determined using the actin signal, the number of cells by counting the DAPI stained nuclei. The confluence was determined by dividing the total cell area by the image area. The mean cell size was determined by dividing the total cell area by the total number of nuclei counted. Significance was tested by applying a Mann-Whitney U test (Software: Prism).

1.6.3 Live-dead staining

Live-dead staining (# L3224, Molecular Probes) was performed according to the manufacturer's protocol. In short, cells were washed three times with PBS (# D8537, Sigma-Aldrich) before being incubated with a reaction mix (Table 12) for maximum 40 min to make sure that effects on cell viability are not induced by the kit itself. After, cells were washed again thrice with PBS.

Table 12: Reaction mix for live-dead staining in 1 mL PBS.

Component	Concentration [mM]	Volume [µL]	End concentration [µM]
Ehtidium homodimer-1	2	4	2
Calcein AM	4	1	4

Live-dead staining to determine membrane coverage with HaCaT cells

Polycarbonate membranes (# 140620, Nunc) were collagen I -coated (# R-011-K, Gibco) and 6 x 10^4, 10^5 and 3 x 10^5 HaCaT cells were seeded on top. After 24, 48 and 72 h cell coverage of the membrane was determined by live-dead staining as described above.

Live-dead staining upon pressure application mediated by teflon mold

9 x 10^3 HaCaT cells were seeded per one well of a 6-well plate and cultivated for two days. Upon confluence PDMS (#101697, Sylgard®) or teflon molds were placed on top of the monolayer and a weight of 1 kg was applied for 1 and 5 min (by using a water-filled schott bottle). Directly after, live-dead staining was performed as described above and membranes were recorded using the Zeiss AxioObserver (see 1.7.1)

1.7 Microscopy

All Images were analyzed with FIJI (Schindelin *et al.*, 2012). All adjustments to image brightness and contrast were performed on the whole image. Special care was taken to not obscure any details. Zen

2.3 (blue edition; © Carl Zeiss Microscopy GmbH, 2011) or with Leica Application Suite X (© 2018 Leica Microsystems CMS GmbH) were used to combine several image tiles to one bigger overview.

1.7.1 Zeiss AxioObserver Z1

Proof of principle imaging during development of the 2D epidermal models was performed with Zeiss AxioObserver Z1 microscope equipped with an Orca R2 camera (Hamamatsu). It is controlled by the ZEN blue software. In brightfield an HAL100 LED was used and for fluorescence microscopy the sample was illuminated with three LEDs (385, 570, 555) with appropriate filters (Table 13: Fluorescence filter cubesTable 13). A 10x objective (EC Plan-NEOFLUAR, NA: 0.3) was used. To visualize 2D epidermal models after 4 days of incubations tiles were recorded to cover the full cut side. Full membrane overviews were performed either with a tile's shift of 100 % to save memory storage or for more details with an overlap of 10 %.

Table 13: Fluorescence filter cubes Zeiss AxioObserver Z1.

Filter Cube	Excitation [nm]	Emission [nm]
DAPI	BP 377/28	BP 464/100
Alexa 488	BP 470/40	BP 525/50
TRITC	BP 546/12	BP 607/80

1.7.2 Olympus DeltaVision

HaCaT cell adhesion on coated or non-coated polycarbonate membranes was investigated with a Delta Vision (DV) system (Applied Precision Inc.) on an Olympus IX inverted microscope, equipped with a cooled CCD camera. The 10x objective (NA: 0.3; Olympus) was used.

Table 14: Fluorescence filter cubes for Olympus DeltaVision.

Filter Cube	Excitation [nm]	Emission [nm]
TRITC	575/25	625/45
DAPI	390/18	435/48

1.7.3 Zeiss LSM800

Confocal images were acquired with a Zeiss LSM800 laser-scanning microscope with a 63x immersion oil objective (Plan-Apochromat 63x/1.40 Oil DIC, Carl Zeiss AG). A Z-stack starting from the cell bottom was recorded. Images at the Z-level of focal adhesions were used.

Brightness and contrast were adapted and all settings were identically applied on all images of the CD44 or vinculin channel.

1.7.4 Leica DMi8

Life cell imaging was performed on a Leica DMi8 inverted fluorescent microscope equipped with a sCMOS camera (Leica DFC9000GT) using a 10x objective (HC PL FLUOTAR, NA 0.32, PH1). The microscope was equipped with a dark incubation chamber controlling the temperature and CO_2. The LAS X software (Leica) was used to acquire images.

For cell adhesion assays five positions per well were chosen and an image was recorded every hour. The APC autofocus was activated to hold the focus during image acquisition.

For migration assays with 2D epidermal models the full wound site was recorded in five single tiles with no overlap to avoid duplets during analysis. One image per hour was recorded.

Table 15: Fluorescence filter cubes for Leica DMi8

Filter Cube	Excitation [nm]	Emission [nm]
Alexa 555	546/10	585/40
DAPI	350/50	460/50

1.8 Synthesis of end-alkylated HA

5, 10 and 60 kDa HA was end-alkylated at the reducing N-acetylglucosamine unit of HA as described before (Lee *et al.*, 2008). In short, 100 mg HA and 670 µL propargylamine (# P50900, Sigma-Aldrich; end conc. 523 mM) were dissolved in 20 mL borate buffer (100 mM, pH 8.5) together with 468 mg NaCl (end conc. 400 mM) and stirred for 2 h at RT. 251 mg sodium cyanoborohydride (end conc. 200 mM) were added and the reaction was carried out for 5 days at 40 °C. After, the reaction solution was dialyzed (MWCO: 2000 Da) against dH_2O for 2 days, lyophilized and stored at − 80 °C. The reaction solution was dialyzed first against dH_2O, containing sodium chloride and hydrochloric acid overnight. And the next two days against dH_2O containing sodium chloride with changing the dialysis solution six times. After, the reaction solution lyophilized and stored at − 20 °C.

1.9 Quartz crystal microbalance with dissipation monitoring (QCM-D)

Quartz crystal microbalance with dissipation monitoring (QCM-D) tracks changes in dissipation and normalized frequency over time. Changes in frequency as well as dissipation are recorded and indicate mass adsorption (change in frequency) as well as give insights into the viscoelastic properties and rearrangements within the monolayer (change in dissipation) (Dixon, 2008). The mass absorption

(Δm) on the QCM-D crystal can be quantified based on its frequency change. The correlation between change in resonant frequency and mass of the adhering layer is described in the Sauerbrey equation (Sauerbrey, 1959):

$$\Delta m = -\left(\frac{N_q \rho_q A}{f_q}\right)\frac{\Delta f}{f_q} \tag{2}$$

Where N_q is the quartz crystal constant and ρ_q is the density of the quartz crystal (for an AT-cut crystal: N_q= 1.668 x 10^5 Hz cm (Janata, 1989); ρ_q = 2.648 g cm^{-3} (Brice, 1985)). A is the area of deposition. f_q is the resonant frequency of the fundamental mode (Hz) and Δf is the normalized frequency change (Hz). The prefactor $N_q \rho_q A / f_q$ divided by f_q gives an estimate of the resonator's mass sensitivity, S_T (Mueller and White, 1968). For the values given above and a fundamental frequency of 5 MHz gives S_T = 9.6 ng Hz^{-1}. Taking the area of deposition into account with approximately 0.5445 cm^2 results in S_T = 17.67 ng Hz^{-1} cm^{-2}.

As the Sauerbrey equation assumes that the adhering layer does not interfere with the sensitivity of the crystal mass changes are expected to be underestimated the thicker the adhering layer gets (Stambaugh *et al.*, 2020). Stambaugh *et al.* (2020) proofed that that the energy-based method, which is based on the energy loss evoked by the adhering layer, provides a better accuracy.

$$\Delta m = -S_T \frac{f_q}{2}\left(\frac{1}{(1-\Delta f/f_q)^2} - 1\right) \tag{3}$$

Based on (3) the change in mass [ng] per active crystal area were calculated using the recorded changes in frequency. Next, Δm was scaled up to an area of 1 cm^2. Molarity was determined by using the formula $n=m/M$. By dividing n by the Avogadro constant of $6.022 \cdot 10^{23}$ and the respective MW of a single HA molecule returns the number of HA molecules per cm^2 and per μm^2, respectively. However, using the Sauerbrey equation and all derived equations to calculate the mass bound to the crystal surface during QCM(-D) measurements are only valid for oscillation in air and for rigid masses. Thus, once QCM-D measurements are made in aqueous solutions and viscoelastic films are formed the relations are more complex as the crystal's oscillation is not only affected by the adsorbed mass itself but also by mass-environment interactions such as water binding and viscoelasticity. Hence, additional variables would need to be introduced such as the shear viscosity coefficient and a shear elasticity modulus (Voinova *et al.*, 1999).

1.9.1 Quartz Crystal Microbalance to determine HA end-alkylation

QCM-D experiments were performed on a manual "E4 modul" (Q-Sense AB) with the so called "open modul". Gold coated quartz crystals (QSX301, Q-Sense AB) were used and activated for 10 min using a UVO cleaner (UV-ozone Pro Cleaner^{TM}, BioForce Nanosciences). After, the crystals are placed in the open module and the fundamental frequency and its overtones (n= 3, 5, 7, 9, 11 and 13) are determined in air until a plateau has been formed for 5 min. Next the system was equilibrated to the buffer, in which the measurement was performed. In this thesis this was either 0.1 M TRIS buffer (pH 8.5; # 4855-3; Roth) or PBS (# D8537, Sigma-Aldrich). The equilibrium is reached, once a plateau has been formed and by definition has been stable for 5 min. Adding different components, being solved in the buffer system was always followed by a washing step with the respective buffer system until once again a plateau was reached. QCM-D data was analyzed by comparing the buffer plateau before adding a new component with the buffer plateau after the component was added. For this the mean and standard deviation of Δf and ΔD for 5 min is determined.

To prove successful HA alkylation the experimental set-up of Minsky *et al.* was applied (Minsky, Antoni and Boehm, 2016). First, a mixture of OEG-alkanethiol (HS-$(CH)_{11}$-EG_3-OH; referred to as EG_3OH) and OEG-alkanethiols with a terminal azide group (HS-$(CH)_{11}$-EG_6-N_3; referred to as EG_6N_3) was used in a 1:1 ratio at a total concentration of 100 µM in TRIS buffer (100 mM, pH 8.5). This has been described to form protein-repellent, spontaneous self-assembled monolayers (SAMs) on gold surfaces upon co-adhesion (Love *et al.*, 2005). Next, 2.5 mg/mL HA was dissolved in 0.1 M TRIS buffer (pH 8.5) first withoutand later with click reaction buffer. The components, which were added on the gold crystal are summarized in Table 16.

Table 16: QCM-D experiment to prove successful HA end-alkylation. Note: the incubation times are approximated. Actual incubation times can be extracted from the graphs in the results section.

Step	Incubation time	Process
1	15'	wash with TRIS buffer
2	25'	EG_3OH:EGN_3 (50:50)
3	15'	wash with TRIS buffer
4	30'	HAend-alkylated - click reaction buffer
5	15'	wash with TRIS buffer
6	40'	HAend-alkylated + click reaction buffer
7	15'	wash with TRIS buffer
8	25'	Add 0.5 % (w/v) BSA
9	15'	wash with TRIS buffer

1.9.2 Quartz Crystal Microbalance to determine HA saturation

HA saturation upon azide presentation was determined by varying the ratio of EG_3OH and EG_6N_3 according to Table 17. The experimental design to determine the HA saturation in dependence of presented azide groups is given in

Table 18.

Table 17: Pipetting scheme for EG_3OH (5 mM) and EG_6N_3 (5 mM) for indicated mol%.

EG_6N_3 [mol%]	5 mM EG_6N_3 [µL]	5 mM EG_3OH [µL]	buffer [µL]
1	0.1	9.9	490
10	1	9	490
50	5	5	490
100	10	0	490
25	2.5	7.5	490
75	7.5	2.5	490

Table 18: QCM-D experiment to determine HA saturation in dependence of presented azide groups. *Note: the incubation times are approximated. Actual incubation times can be extracted from the graphs in the results section.*

Step	Incubation Time	Process
1	15'	wash with Buffer
2	25'	EG_3OH:EGN_3
3	15'	wash with Buffer
4	40'	HAend-alkylated + click reaction buffer
5	15'	wash with Buffer
6	25'	add aggrecan/HABP
7	15'	wash with Buffer

1.9.3 Quartz Crystal Microbalance to determine bioactivity of immobilized HA

The experimental design to determine the bioactivity of HA upon immobilization is given in Table 19.

Table 19: QCM-D experiment to determine bioactivity of immobilized HA. *Note: the incubation times are approximated. Actual incubation times can be extracted from the graphs in the results section.*

Step	Incubation Time	Process
1	15'	wash with TRIS buffer
2	25'	EG3OH:EGN3 (50:50)
3	15'	wash with TRIS buffer
4	40'	HAend-alkylated - click reaction buffer
5	15'	wash with TRIS buffer
6	30'	wash with 300 mM NaCL
7	30'	wash with PBS-- with 1mM EDTA
8	15'	wash with PBS--
9	80'	100µg/mL Aggrecan in PBS--
10	15'	wash with PBS--
11	15'	wash with TRIS Buffer

1.9.4 Cleaning Procedure

After the QCM-D measurement chambers were washed with 600 µL 2 % sodium dodecyl sulfate (SDS) for 10 min. After, chambers are rinsed with dH_2O until all SDS traces (bubbles) were removed. Gold coated QCM-D crystals were detached from the QCM-D instrument and transferred in a 2 % SDS solution, before being chemically cleaned. For chemical cleaning crystals are first rinsed with water, dried in nitrogen flow and placed into customized teflon holders. Next, an oil-bath is heated to 70 °C and a cleaning solution of dH_2O, 25 % ammonia and 30 % hydrogenperoxide (5:1:1) is prepared. The crystals are transferred into the cleaning solution and the reaction was carried out for 10 min at 70 °C. After, the crystals were rinsed thoroughly with dH_2O and dried in nitrogen flow.

3 Results and Discussion

3.1 Part I: Effect of apical HA administration on re-epithelialization

3.1.1 The effect of apical HA administration on keratinocyte migration is rather concentration dependent than size dependent

To investigate the role of apically applied hyaluronic acid (HA) on human keratinocyte migration I used the spontaneously immortalized keratinocyte cell line HaCaT. HA has been described to appear in a rod-or coil-like structure depending on the polymer's length and thus its molecular weight (MW) (Weigel and Baggenstoss, 2017). The shift of more linear polymers to more coiled polymers in solution occurs within a range of around 200 kDa (Weigel and Baggenstoss, 2017). Therefore, in order to minimize the conformational variability of HA in solution, I selected HA with molecular weights considerably smaller or considerably bigger than 200 kDa. In detail, to cover a wide range of HA sizes, HAs with a MW of 5, 60, 700 kDa and 1.8 MDa were used.

As HA is a macromolecule of repeating disaccharide units it can also be seen as a macromolecule of repeating binding motifs. Thus, as I focused on the interaction of cells with binding motifs within HA, I kept the mass concentration constant and not the molar concentration. Generally, the concentration of HA in unwounded human skin is about 400-500 µg HA/g tissue (Cowman *et al.*, 2015). Upon wounding, HA levels are increased through transcriptional activation of the HA synthases (HAS) genes (Tammi *et al.*, 2005). Simultaneously the activity of HA-degrading enzymes like hyaluronidase or reactive oxygen species (ROS) rises, resulting in fragmentation of the physiological HA (Aya and Stern, 2014). In case the total available HA has been degraded to one specific size it is thus expected that the concentration of especially smaller HA sizes increases at least to 500 µg/g. However, *in vivo* concentrations might be even higher if a wound-induced increase in newly synthesized HA is additionally taken into account. Therefore, I decided to test HA concentrations from well below to twice the anticipated physiological levels, i.e.: 5, 50, 500, and 1000 µg/mL. Control samples received culture medium without any HA.

An artificial wound site was generated by using commercially available silicone confinements. These confinements have two chambers. Cells were seeded in both chambers and cultivated until a confluent monolayer was formed. Next, the confinement was removed revealing a cell-free gap in between the monolayers. This gap mimics an artificial wound site (Figure 10 A).

To minimize the possibility that HA-induced effects might be masked by fetal bovine serum (FBS) containing medium, serum-depletion experiments were performed to identify the minimal serum amount needed for cell growth. Supplemented serum was reduced upon initiation of cell migration to 0, 0.1, 1, 2.5, 5 % (v/v) and HaCaT migration was compared to medium with 10 % (v/v FBS). Based on the results and congruent to published work an FBS concentration of 1 % was applied in all future experiments (Appendix, Figure 41) (D'Agostino *et al.*, 2015, 2017).

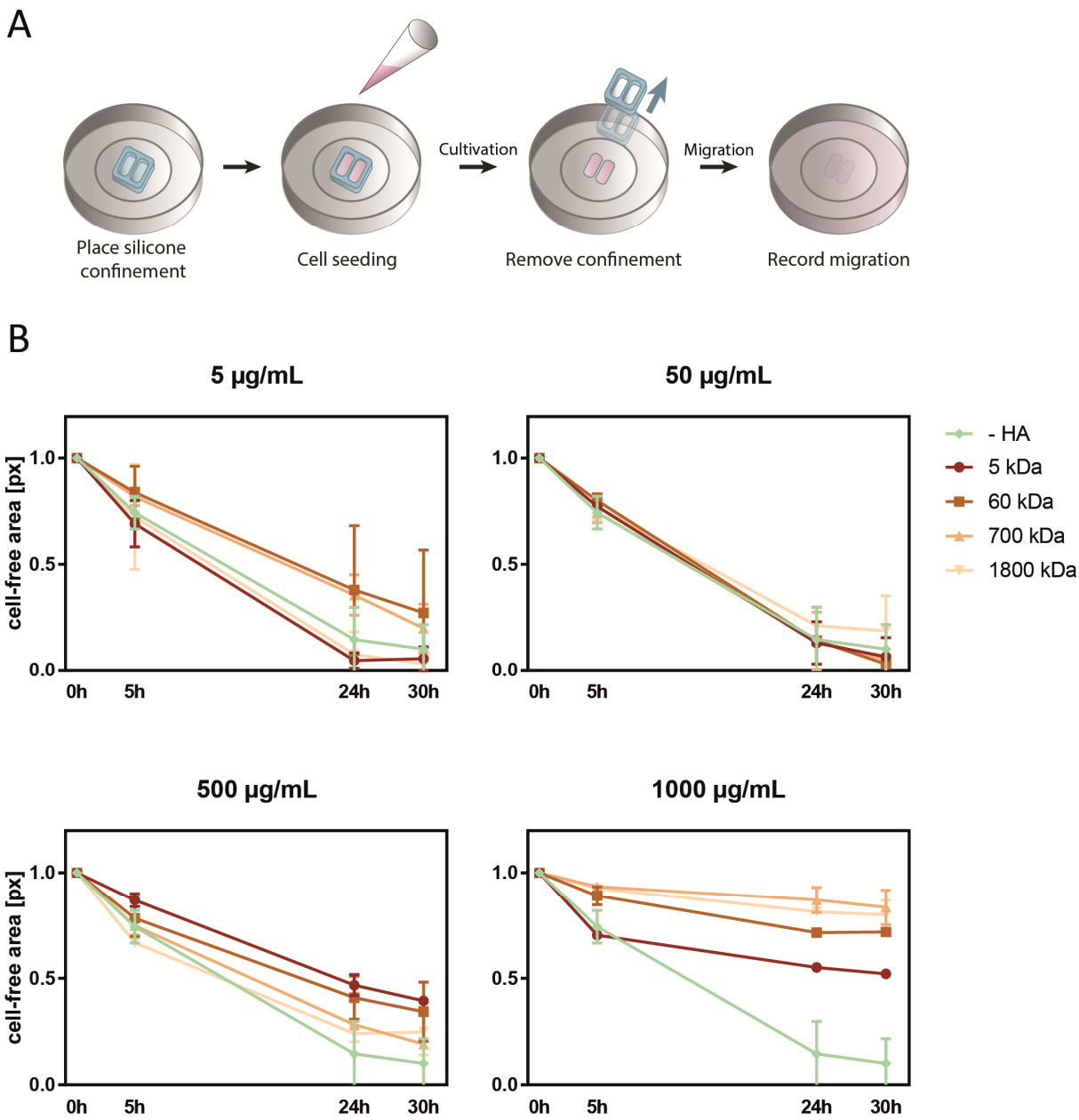

Figure 10: HaCaT migration into cell-free area in dependence of different HA sizes and concentrations over a total observation period of 30 h. (A) Schematic illustration of the *in vitro* wound healing model with silicone confinements. HaCaT cells are seeded in both chambers of a confinement and cultivated until full confluence. Upon removal of the confinement two adjacent epithelial monolayers with a cell-free gap (resembling an artificial wound site) in between them, have been formed. (B) An artificial wound site was generated by seeding 7 x 104 HaCaT cells in each chamber of a two-chambered confinement in DMEM supplemented with 10 % (v/v) FBS on collagen I-coated glass surfaces. After 24 h of cultivation the confinement was removed and cell culture media replaced by DMEM 1 % (v/v) FBS with respective HA species (5, 60, 700 and1800 kDa) in the indicated concentrations (0, 5, 50, 500 and 1000 µg/mL). Images of the artificial wound site were taken directly after confinement removal and after 5, 24 and 30 h. The cell-free area was semi-automatically determined following image segmentation. Graphs show two replicates per condition, each value represents mean ± SD. Result of one representative experiment out of three independent experiments. The cell-free area was normalized to the cell-free area directly upon HA treatment at 0 h.

HA solutions of different MWs as well as concentrations were prepared and pH and osmolarity were measured to ensure physiological conditions of experiments (Material and Methods, Table 3). To investigate the effect of apically applied HA on HaCaT migration artificial wound sites were generated

on collagen I-coated glass surfaces. HA solutions were directly applied after removal of the cell culture confinement, i.e. with initialization of HaCaT migration into the cell-free area. Closure of the cell-free area was recorded by taking images of the wound site after 0, 5, 24 and 30 h. The cell-free area was determined semi-automatically (Material and Methods, 1.5.3).

Over the time of observation, HaCaT cells migrated into the wound site leading to a decrease in cell-free area (Figure 10 B). Interestingly, at concentrations of 5, 50 and 500 µg /mL all tested HA variants showed quite similar effects independent from their MW. Overall, there was a tendency that the higher the HA concentration is, the lower is the change in cell-free area over time and thus the migration speed of the keratinocytes. Only solutions with 1000 µg/mL HA differed from control samples after 24 h, independently of the MW of the HA deployed. Figure 11 depicts the normalized data of three independent experiments, each consisting of two biological replicates after 24 h.

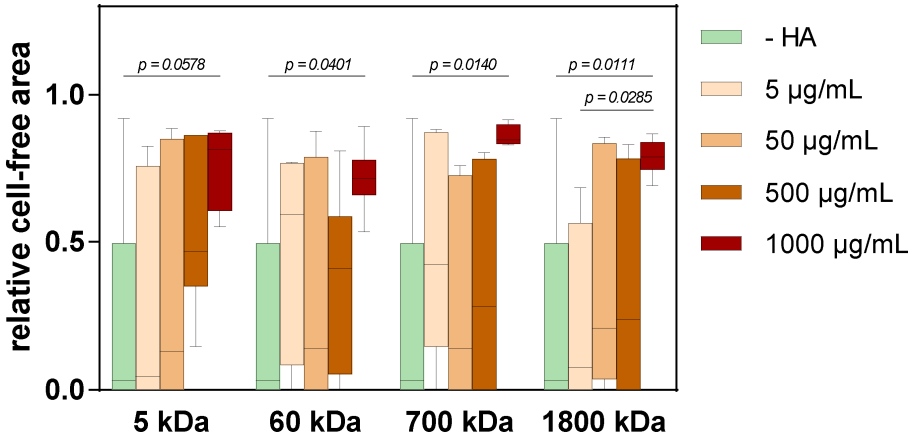

Figure 11: Relative cell-free area upon HA administration after 24 h. An artificial wound site was generated by seeding 7 x 104 HaCaT cells in each chamber of a two-chambered confinement in DMEM supplemented with 10 % (v/v) FBS on collagen I-coated glass surfaces. After 24 h of cultivation the confinement was removed and cell culture media replaced by DMEM 1 % FBS with respective HA species (5, 60, 700 and 1800 kDa) in the indicated concentrations (0, 5, 50, 500 and 1000 µg/mL). The cell-free area was semi-automatically determined following image segmentation. N= 12, and 6 for –HA and 5, 50, 500, 1000 µg/mL, respectively, from three independent experiments. The cell-free area was normalized to the cell-free area directly upon HA treatment at t0. Each box represents median ± 5-95 percentile. 2-way ANOVA test revealed indicated p-values.

Remarkable is the high variance in relative cell-free area of all samples though. initial cell seeding number was identical for all treated samples. Interestingly, this variance is lower for higher concentrations of HA independently of the MW of applied HA. For the highest concentration, 1000 µg/mL, the variance decreases the higher the MW of HA is. The smallest sample variances were observed for 1000 µg/mL of 700 or 1800 kDa solutions (Figure 11). Significant differences ($p < 0.006$) were observed for all MWs of HA between the negative control (without HA) and 1000 µg/mL HA solutions. All together these results indicate that the actual HA size has minor effects on cell migration. However, high HA concentrations negatively impact HaCaT cell migration.

Potential reasons for the high variance might be batch variances of the coating matrix as well as the mitotic activity of the HaCaT cell population at the starting period of the experiment. Additionally,

using confinements to create an artificial wound site, two confluent monolayers are facing each other. These monolayers are not limited at their edges (see Figure 10 A). Subsequently, cells could either migrate in the direction of the opposing monolayer (this movement was recorded) or migrate to the opposite direction, a movement which is not taken into account in this analysis. The recording strategy of the wound site might further negatively impact the high variances. To simplify the experimental set-up the artificial wound sites were imaged manually and not automatically by e.g. time-lapse imaging. Even though the center of the wound site was carefully located for each time point, it cannot be excluded that the recorded field of view might have shifted from one time point to another. This would eventually lead to an increase in deviation of the determined cell-free area. Interestingly, variances were clearly lower in cases where the maximum HA concentration was employed. A reduction of HaCaT migration upon treatment with high HA concentrations was reproducibly observed in all independent experiments (Appendix, Figure 42). This indicates a biological reason for the reducing variance upon usage of high HA concentrations. At low concentrations it is probably very unlikely that all available cell-bound HA receptors bind exogenously applied HA. Single samples would accordingly show divergent reactions towards the treatment, reasoning variations already in between technical replicates. Additionally, it has been reported that HA polymers of different size compete for HA binding sites of cluster of differentiation 44 (CD44). With increasing polymer length, binding avidity is increased (Lesley *et al.*, 2000). It cannot be excluded that HaCaT cells themselves deposit high MW HA. This might explain the further reduction in variance of measured cell-free area especially for higher MWs applied.

The effect of HA on re-epithelialization and migration respectively is contradictory, as experimental parameters differ from one study to another (see 1.3.5). Ghazi *et al.* investigated the effect of high molecular weight HA (HMWHA) (1000<MW<1400 kDa), medium molecular weight HA (MMWHA) (100<MW<300 kDa) and low molecular weight HA (LMWHA) (5<MW<20 kDa), each applied in a concentration of 2 mg/mL, on HaCaT migration. They observed a pro-migratory effect of HA only for MMWHA. HMWHA and LMWHA had no significant effect on HaCaT migration compared to control samples (Ghazi *et al.*, 2012).

D'Agostino *et al.* observed an increase in HaCaT migration for 6, 15, 50, 100, 500, 1400 and 1800 kDa within the first 10 hours by performing scratch assays on collagen I-coated cell culture plastic surfaces (D'Agostino *et al.*, 2017). The higher the MW of applied HA, the stronger was this effect. However, the researchers did not compare different concentrations of HA but performed their experiment with a constant concentration of 1 mg/mL HA dissolved in cell culture medium supplemented with 10 % (v/v) FBS. Comparing these results with my results for 1 mg/mL HA solutions at different MWs, no clear indication of a size dependent effect of HA was revealed. However, in contrast to my experiment, D'Agostino *et al.* supplemented their medium with 10 % (v/v) FBS and used collagen I -coated cell culture plastic as substrate (D'Agostino *et al.*, 2017).

This raises the question about the impact of the substrate nature (plastic or glass) and of FBS supplementation on HA's impact on HaCaT migration. To reproduce the results of d'Agostino *et al.*, I adapted my experimental set-up: using only 1 mg/mL HA solutions, collagen I-coated cell culture plastic surfaces as well as cell culture medium supplemented with 10 % (v/v) FBS. To examine the impact of the wounding strategy I additionally compared HaCaT migration in wounds generated by scratch (as has been performed by d'Agostino *et al.*) and using confinements to produce two adjacent confluent monolayers. These adaptations were sufficient to revert HA's effect on cell migration. Compared to control samples without HA dissolved in medium the treatment with any of the HA sizes led to an increase in reduction in cell-free area over the observation period, independently of the wounding strategy and vol% of supplemented FBS (Appendix, Figure 43). Higher FBS supplementation generally increased migration velocity, recognizable by a faster wound closure. Wound closure for samples supplemented with 10 % (v/v) FBS occurred within 24 h, whereas samples with 1 % (v/v) FBS were not fully closed after 48 h. This is in in accordance with previous data of me and others (Appendix, Figure 41)(Wu *et al.*, 2017). Besides amino acids, sugar and lipids FBS contains growth factors, as well as hormones. Some of these, such as the growth factors EGF and KGF, have been reported to stimulate keratinocyte migration and proliferation *in vitro* (Tammi *et al.*, 2005). Moreover, EGF and KGF also increase HA synthesis (Karvinen *et al.*, 2003; Pasonen-Seppänen *et al.*, 2003). As the exact composition of FBS is never known it is therefore important to reduce the amount of FBS to a minimum in order to have a controllable model system.

Comparing the applied wounding strategies – scratch assay vs confinement-based artificial wounds – there was a tendency of stronger positive effects of HA administration in using a scratch instead of confinements. In principle, this is quite logical as confinements do not inflict a real wound but are a suitable tool to examine cell migration independently of wounding. Contrary to that, cells are damaged upon performing a scratch assay and thus a more complex process is initiated resembling *in vivo* wound healing. Therefore, it can be presumed that effects upon HA administration observed in my experiments might be stronger if a real wound, e.g. by a scratch assay, was applied.

Figure 10and Figure 41 both coincide using collagen I as coating matrix. Though the underlying substrate was the same, D'Agostino *et al.* performed their migration experiments on cell culture plastic while glass surfaces were used in my experiments. Both surfaces, standard cell culture plastic as well as glass, lay beyond substrate stiffness which can be distinguished by cellular sensation (standard cell culture plastic: ~1 GPa; glass: ~70 GPa (Garland *et al.*, 2014). Nevertheless, surfaces prerequisites affect collagen I coating in regard to coating efficiency and topography (Damiati *et al.*, 2018). Thus, I was interested whether the coating itself might be responsible for the opposing effect of HA during HaCaT migration.

3.1.2 The ECM environment influences the migration capacity of keratinocytes

To determine the impact of the extracellular matrix (ECM) environment on the effect of HA on keratinocyte migration, I applied the same experimental set-up with confinements and with 1 % (v/v) FBS as described before. This time, not only collagen I-coated glass surfaces but also fibronectin as well as laminin 332-coated surfaces were used. Laminin 332 forms a main part of the basement membrane which separates the epidermis from the dermis. Thus, keratinocytes typically face laminin 332 in unwounded healthy tissue. Collagen I and fibronectin are both components of the granulation tissue formed during wound healing. To simulate the transfer from HMHA to LMWHA upon wounding I applied 1800 kDa HA as well as 5 kDa HA. The physiological HA size is 4000-6000 kDa in unwounded human skin (Cowman *et al.*, 2015). Upon wounding HA is fragmented by hyaluronidases and ROS. Therefore, it is expected that the concentration of especially smaller HA sizes increases. Thus, 5 kDa HA at a high concentration of 500 µg/mL was used. In order to keep the number of binding motifs comparable, 1800 Da HA was applied at its lowest concentration tested (5 µg/mL).

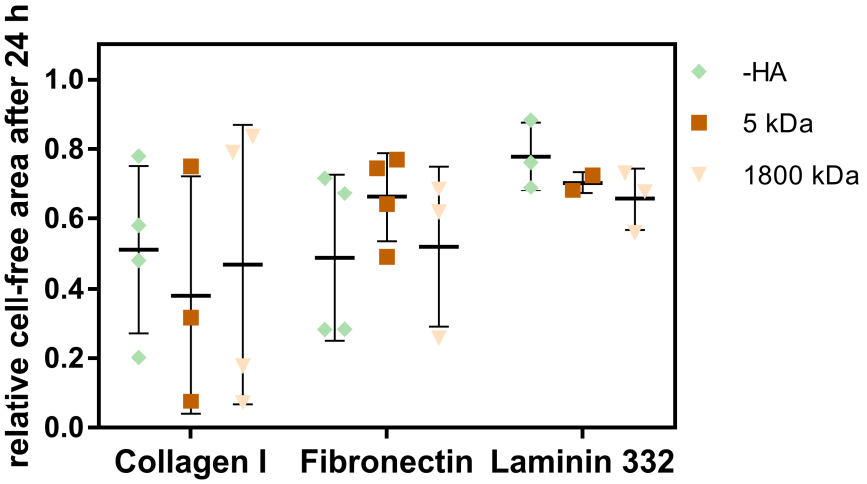

Figure 12: Impact of the ECM on HaCaT migration upon apical HA administration after 24 h. An artificial wound site was generated by seeding 7 x 104 HaCaT cells in each chamber of a two-chambered confinement in DMEM supplemented with 10 % (v/v) FBS on collagen I, fibronectin and laminin 332-coated glass surfaces. After 24 h of cultivation the confinement was removed and cell culture media replaced by DMEM 1 % (v/v) FBS with respective HA species 5 kDa (500 µg/mL) and1800 kDa (5 µg/mL)). The cell-free area was semi-automatically determined following image segmentation. Data of two independent experiments with N≥2. The cell-free area was normalized to the cell-free area directly upon HA treatment at t0. Each bar represents mean ± SD.

Comparing only the non-treated samples after 24 h hints to an effect of the underlying ECM towards different HaCaT migration capacity (Figure 12). The mean migration of HaCaT on collagen I (0.511 ± 0.24) and fibronectin-coated (0.0.488 ± 0.24) surfaces was similar. For laminin 332-coated surfaces, migration was substantially slower (0.778 ± 0.1). In all set-ups, the additional HA administration did not lead to differences compared to control groups. Interestingly, variances were higher for HaCaT migration on collagen I and fibronectin than on laminin 332-coated surfaces.

The migration capacity of HaCaT cells generally depends on the ECM substrate itself. As expected, HaCaT cells migrated more on collagen I- and fibronectin-coated than on laminin 332-coated surfaces. This was expected as both, collagen I and fibronectin contribute to the ECM of the granulation tissue, which is the substrate for migrating keratinocytes upon wounding and during re-epithelialization. In contrast, laminin 332 naturally occurs in the basement membrane and is associated with non-activated keratinocytes under non-wounded conditions (Rousselle, Montmasson and Garnier, 2019). This is also in accordance to other reported data, where laminin 332 was shown to generally hamper cell migration, whereas fibronectin and collagen I support keratinocyte migration (O'Toole *et al.*, 1997). Due to the high variances (for reasons see 3.1.1) an HA dependent effect on HaCaT migration depending on the underlying substrate can neither be verified nor excluded.

3.1.3 The effect of apical HA administration on proliferation depends on the cell density

During re-epithelialization both active migration into the wound site as well as proliferation occur simultaneously (Safferling *et al.*, 2013). The latter serves to provide new cell material to restore and maintain the cellular barrier function. The confluence differs throughout the wound area. Directly at the wound site, cells face an open space reducing the cell density of the epidermis whereas in the unwounded part of the epidermis, the density is high with cells facing a higher intercellular stress (Vishwakarma *et al.*, 2018). That is why the relative proliferation rate of HaCaT cells upon HA administration was determined in dependence on the density. The before-mentioned sizes and concentrations of HA were applied to examine their effect on proliferation after 5, 24 and 48 hours. To measure the proliferation of HaCaT cells a DNA-based proliferation assay was performed. This assay works via incorporation of the modified thymidine analogue EdU in the DNA (please refer to the Material and Methods section for details). Subsequent end-point staining of EdU reveals cells that underwent mitosis during the course of the experiment. Cells were seeded at a lower (2.5×10^4) and a higher (5×10^4) density – in the following referred to as "low" and "high" density – in one well of a 96-well plate.

Figure 13 depicts the relative proliferation normalized to untreated samples after 24 h depending on cell density as well as applied HA sizes and concentrations. Under conditions of high density proliferation was not affected by most of the applied HA solutions. Solely 60 kDa HA at a concentration of 5 and 50 µg/mL showed the tendency to impair cell proliferation. Contrary to that, for cells seeded at low density almost all HA sizes and concentrations led to an increase in proliferation, compared to untreated control samples. For 5 kDa HA this effect seemed to rise with rising concentration. For 60, 700 and 1800 kDa HA the proliferation enhancing effect initially rose with rising concentration before it slightly reduced at 1000 µg/mL.

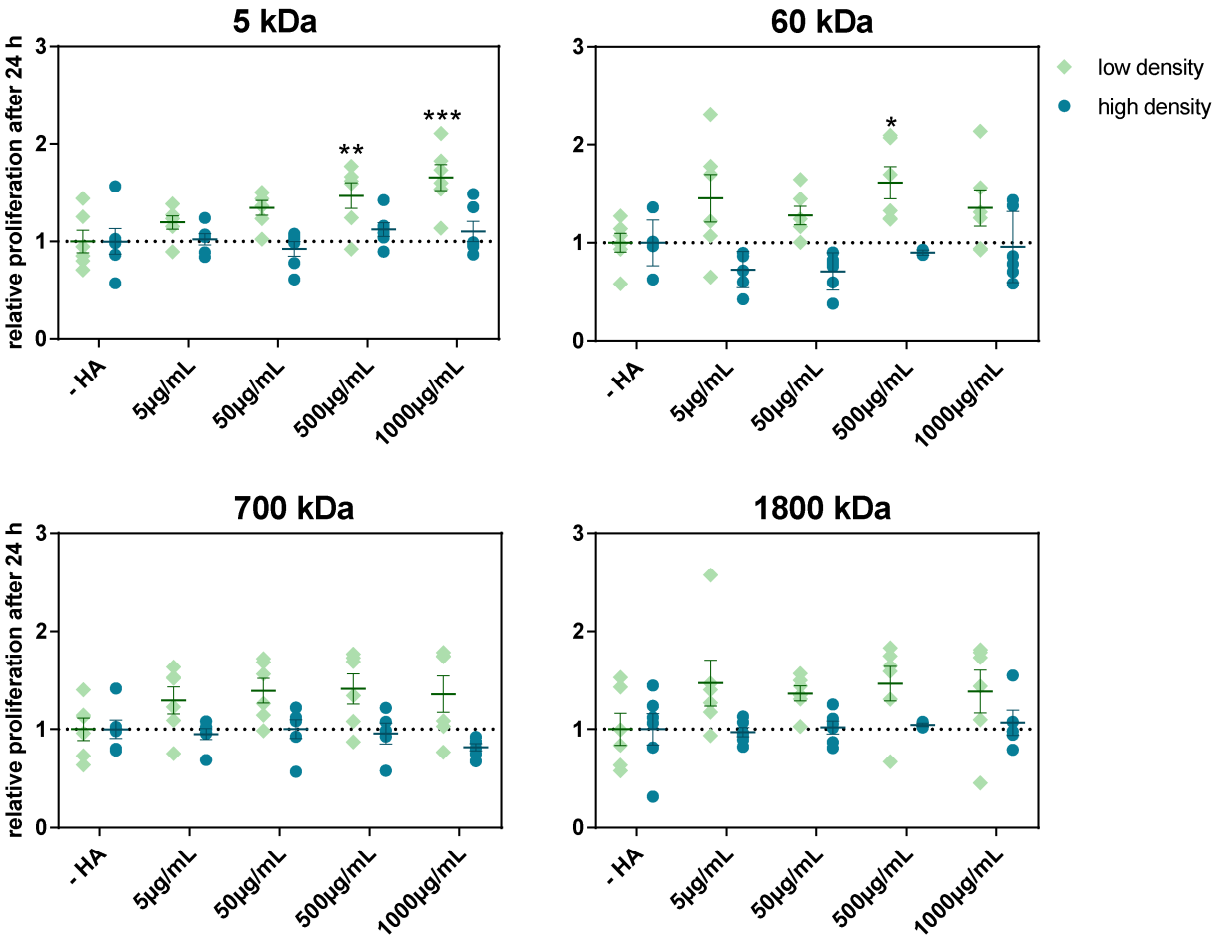

Figure 13: Cell proliferation in dependence of different HA sizes and concentrations as well as confluence over a total observation of 48 h. 5 x 104 ("high" density) and 2.5 x 104 ("low" density) HaCaT cells were seeded in DMEM supplemented with 10 % (v/v) FBS in one well of a 96-Well plate. After 24 h of cultivation cell culture media was replaced by DMEM 1 % (v/v) FBS with respective HA species (5, 60, 700 and1800 kDa) in indicated concentrations (0, 5, 50, 500 and 1000 µg/mL) together with EdU. Relative proliferation rate was determined by dividing the number of EdU stained cells by the number of Hoechst stained cells in an analyzed area of 380 x 380 µm. Data was normalized to mean proliferation –HA after 24 h of respective cell density. Six replicates per condition of two independent experiments each value represents mean ± SEM. Statistical differences was performed applying a 2-way ANOVA test revealed statistical significant differences to control samples (*p<0.1, **p< 0.01, *** p ≤ 0.001).

Over a recording time of 48 h HA did not increase HaCaT proliferation under high density conditions (Appendix, Figure 44 A). For cells seeded at low confluence all HA sizes and concentrations tested led to an increase in proliferation, compared to untreated control samples within 24 hours. After 48 hours the proliferation of untreated and treated samples converged at around 0.8, probably due to reported contact inhibition of epithelial cells upon reaching a specific cell density (Perrais *et al.*, 2007) Appendix, Figure 44 B). In summary, this shows that under conditions of low cell density HA in all concentrations and sizes tested sped up proliferation compared to untreated control samples.

3.1.4 The effect of HA on proliferation in dependence of the ECM environment

HA has been shown to accelerate proliferation under conditions of low density on cell culture plastic surfaces. In order to investigate the impact of the ECM on the effect of HA on HaCaT proliferation I prepared coated glass surfaces. As the ECM itself already possibly affects HaCaT proliferation and to ensure that initial cell seeding number allows for proliferation over a total cultivation time of 48 h without reaching full confluence, HaCaT cells were seeded at low density on collagen I-, fibronectin and laminin 332-coated glass surfaces. Confluence was determined after 5, 24 and 48 h (Appendix, Figure 45). Cells cultivated on collagen I or fibronectin -coated glass surfaces reached a confluence of 50 % and on laminin 332 30 %. Generally, the examination of confluence by phase contrast microscopy indicated a slower proliferation rate compared to cells seeded on cell culture plastic (compare with 3.1.3).

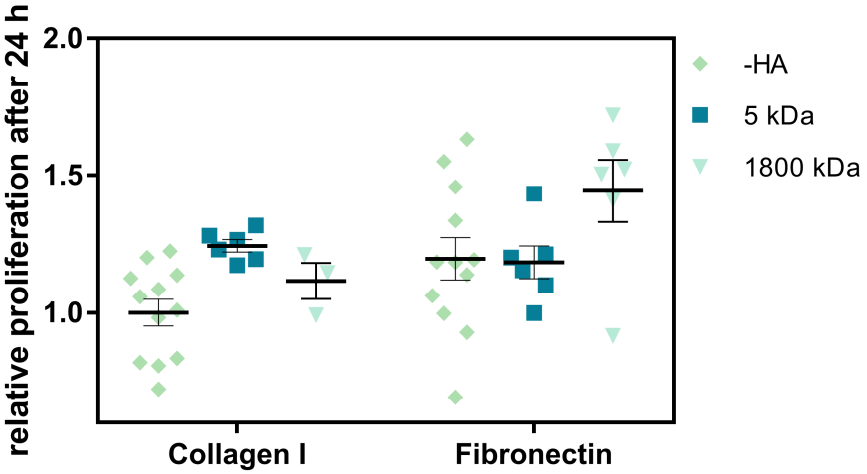

Figure 14: HaCaT proliferation upon apical HA administration on varying substrates after 24 h. 2.5 x 104 ("low" density) HaCaT cells were seeded in DMEM supplemented with 10 % (v/v) FBS in one well of a 96-Well plate. After 24 h of cultivation cell culture media was replaced by DMEM 1 % (v/v) FBS with respective HA species (5 (500 µg/mL) and1800 kDa (5 µg/mL)). together with EdU (1:1000). After 24 h cells were PFA fixed and proliferated cells (which have incorporated EdU) were fluorescently stained via click chemistry and nuclei counterstained with Hoechst. Relative proliferation rate was determined by dividing the number of EdU stained cells by the number of Hoechst stained cells of an area of 380 x 380 µm. Data was normalized to mean proliferation – HA after 24 h on respective coatings. Data of two independent experiments. Each value represents mean ± SEM. A 2-way ANOVA test revealed no statistically significant differences between groups.

As observed in 3.1.2 laminin 332 did not mediate cellular processes occurring during re-epithelialization such as migration. Only collagen I and fibronectin, representing ECM components of the granulation tissue and thus mimicking the typical ECM environment during the process of re-epithelialization, were tested on a combined effect of ECM substrate with HA. For this, HaCaT cells were cultivated overnight to properly attach and adapt to the respective substrates before being treated with 5 kDa and 1800 kDa HA, the same HA species as used in 3.1.2. Relative proliferation was determined after 24 h.

For collagen I-coated glass surfaces both HA sizes led to an increase in proliferation (5kDa: 1.243 ± 0.055; 1800 kDa: 1.115 ± 0.113) compared to untreated cells (-HA: 1.000 ± 0.168). For fibronectin-coated glass surfaces, only 1800 kDa slightly increased proliferation (Figure 14). However, differences were not statistically significant. Differences in proliferation capability in regard to underlying substrates were not observed as both control samples without HA showed a similar non-normalized relative cell proliferation of 0.627 for collagen I and 0.603 for fibronectin (Appendix, Table 25).

Different assays to determine proliferation are available. Generally, one can distinguish between metabolism-based and DNA-based assays. Metabolism-based assays work on the principle that metabolic activity is a direct indicator of the number of cells: the more cells there are, the higher is the metabolic activity. These tests come with the advantage that they typically work on the basis of metabolic indicators, often conserved reducing agents usually synthesized by cells. Thus, these assays can be performed in live cells. However, as HA as a polysaccharide has been reported to potentially contribute to the energy supply of cells, the possibility that HA administration alone might be sufficient to affect cellular metabolic activity cannot be excluded. Moreover, an increase in metabolic activity upon HA administration has been shown for stem cells (Lambrichta *et al.*, 2014). Additionally, a direct comparison between both assay strategies, metabolic-based or DNA-based, revealed discrepancies between both (Quent *et al.*, 2010). Therefore, a DNA-based proliferation assay was favored over a metabolic-based one to determine HA's effect on HaCaT proliferation. The applied EdU assay comes with the advantage of having an internal reference of the initial cell number (i.e. the number of Hoechst-only stained cells).

The relative proliferation upon HA administration was examined on different surfaces: cell culture plastic, with no ECM proteins presented, or glass coated with collagen I and fibronectin. As expected differences occurred depending on the density of treated cells on cell culture plastic. All HA sizes and concentrations accelerated proliferation under conditions of low confluence. However, cells with a high density did not respond to HA in terms of proliferation. In the case of 60 kDa, HA proliferation was rather hampered. Interestingly, without any HA applied proliferation was higher for high density than for low density in 3 of 4 cases within the first 24 h of observation (Appendix, Figure 44). Generally, fold change in proliferation upon HA administration is higher for HaCaT cells cultured on cell culture plastic than on protein-coated glass surfaces. One reason might be the contribution of ECM proteins on keratinocyte proliferation (Dawson *et al.*, 1996). The ECM environment can differ between cell culture plastic and coated glass surfaces regarding composition as well as binding ligand density. A way to better distinguish the influence of those parameters would be by varying the concentration of coated proteins on glass surfaces.

As mentioned before, Ghazi *et al.* investigated the effect of HMWHA (1000<MW<1400 kDa) MMWHA (100<MW<300 kDa) and LMWHA (5<MW<20 kDa), each applied in a concentration of

2 mg/mL, on HaCaT migration but also on proliferation. They showed an increase in cell proliferation upon HA administration only for a MW ranging from 100-300 kDa. For HA lower than 20 kDa or exceeding 1000 kDa, no effect on proliferation was observed. Contradictory to that, another study on primary keratinocytes examined a clear increase in keratinocyte proliferation upon topical administration of HA sizes of 27 kDa and only small effects upon administration of HA of 200 to 1000 kDa, all applied at a concentration of only 50 µg/mL (Bourguignon *et al.*, 2013). In my experiments I observed an accelerated proliferation under conditions of low cell density for all HA sizes and concentrations tested. As past studies observed a transition of HA mass to HA diameter within the range of 150-250 kDa, I chose sizes of HA which were distinctly higher or lower (Weigel, 2017).

Again, as already observed for the migration assay (see 3.1.1), rather high variances between independent experiments were observed. Within one experiment, variability was lower in the proliferation assay compared to the migration assays. A potential reason might be the Hoechst staining serving as an internal control in case of the proliferation measurements.

To sum up, for the first time a comprehensive study of a wide range of HA sizes applied in different concentrations within one and the same experimental set-up was performed for HaCaT cells. I showed that HA's role on migration is rather concentration-dependent, whereas in terms of proliferation, effects seem to be rather size-dependent in the framework of my experimental set-up. This seems contradictory at first sight as in the migration assay, proliferation would contribute to cell migration when newly proliferated cells push anterior cells into the wound site. However, the section with low HaCaT density in the migration assay and thus the number of cells which respond to HA administration in a pro-proliferative way is rather small. Therefore, it is possible that in this experimental set-up, HA-induced effects on proliferation (which cannot be excluded) are masked by the stronger anti-migratory effect of HA. A strategy to separate proliferation from migration would be to utilize proliferation inhibiting substances, e.g. by a preceding mitomycin C treatment (Pastar and Stojadinovic, 2010).

As has been shown, the effects of HA on cellular processes are diverse and different studies show contradictory results even within defined processes such as migration or proliferation. There might be various reasons for this: different cell types, cell lines or primary cells, different surface coatings as well as their topography and proteolytic processing, different surfaces (gels, plastic or glass) with aberrant mechanical properties, different concentrations of HA and finally different sizes of HA. Several studies indicate that HA's effects are influenced by all of these parameters (e.g. Tammi *et al.*, 2005; Ghazi *et al.*, 2012; Damodarasamy *et al.*, 2014; Frenkel, 2014; D'Agostino *et al.*, 2017). Additionally, typical experimental set-ups such as migration assays or proliferation assays are designed combining several parameters resulting in an uncontrolled interdependence between HA and e.g. the extracellular environment. Often, cells are apically treated with HA by dissolving the polymer in cell culture medium. Since an active uptake of HA (labeled by [^{3}H]-HA) through mouse and human skin was shown, proving an active transport of HA and no passive diffusion (Brown, Alcorn and Fraser, 1999), solved HA indeed

is capable of inducing intracellular signaling cascades. Often, concentration-dependent effects of HA are neglected and the focus is on HA's polydispersity by comparing deviating effect of different MWs. However, HA polymers can form intra- as well as inter-polymer hydrogen bounds which affect their conformation and 3D appearance. This in turn might negatively affect HA-receptor interactions (Cowman *et al.*, 2005). For example, divalent cations such as Ca^{2+} and Mg^{2+}, typical additives in cell culture medium, can act as some kind of cross-linkers which favor intermolecular HA interactions (Gao *et al.*, 2018). Such events shift the uniform distribution of HA molecules within cell culture medium and these local concentration gradients in turn might affect the actual HA concentration faced by the cell.

Taken together, to annotate specific cellular reactions unambiguously to HA it is decisive to have a highly defined ECM system available where all parameters can be well-controlled.

3.2 Part II: Development of bi-functionalized glass surfaces

To establish a highly defined ECM system to examine the role of HA on processes occurring during re-epithelialization, a system is needed, which provides HA on the one hand and, an adhesive background to mediate cell adhesion and subsequent migration on the other hand Figure 15). Additionally, to control the amount of HA presented to the cell HA should be immobilized orthogonally to cell binding ligands. Such bi-functionalized glass surfaces are generated by using gold-nanostructured glass surfaces. These surfaces are first passivated with a mixture of two polyethylene glycol (PEG) species (PEG2000/PEG3000azide), one of them possessing an azide group (Schenk *et al.*, 2014). Next, specific binding ligands with a thiol linker are bound to the surface via a thiol-gold interaction. After, alkylated HA is immobilized to the azide group of PEG3000azide via click chemistry. Tuning the ratio of PEG2000 to PEG3000azide directly regulates the number of HA molecules bound to the surface.

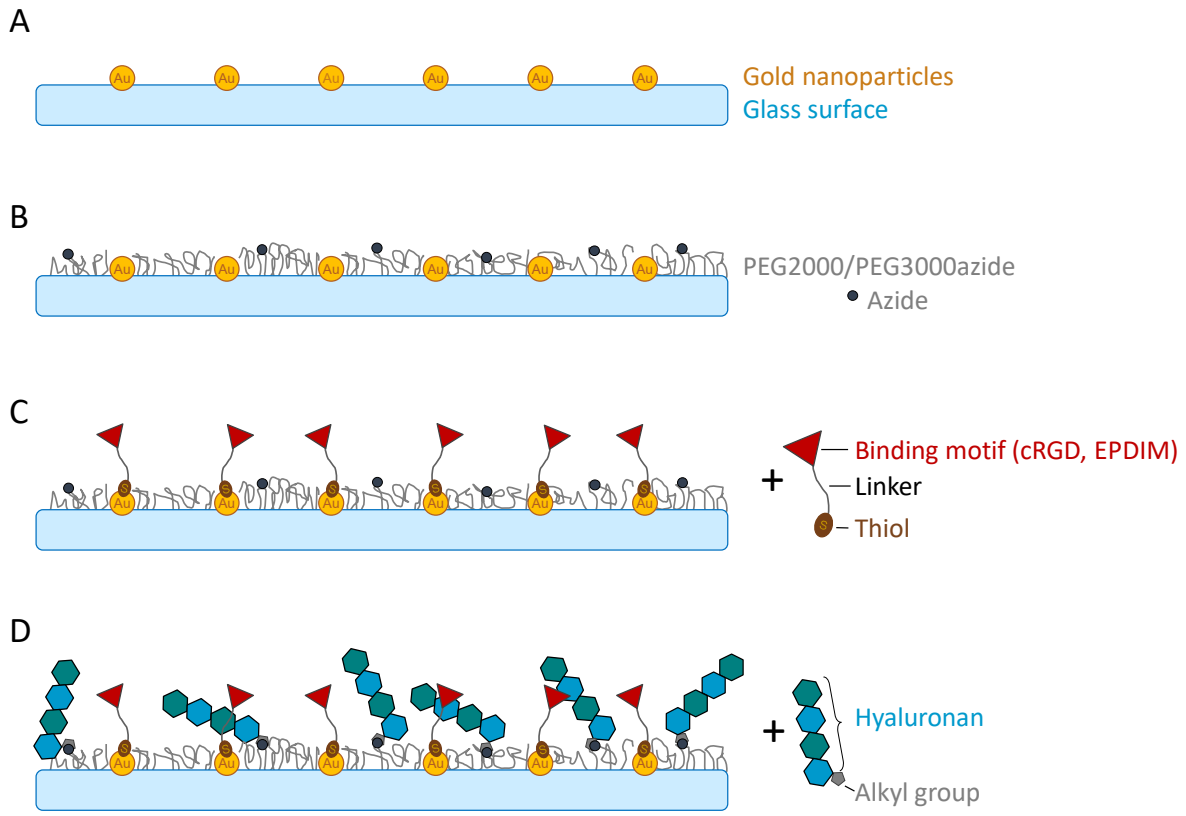

Figure 15: Schematic illustration of bi-functionalized glass surfaces. (A) Gold-nanostructured glass surfaces (generated by BCML) are (B) passivated with PEG2000 and PEG3000azide. (C) Next, cell binding motifs of interest such as cRGD or EPDIM are bound to the gold nanostructures via a thiol linker. (D) Finally, end-alkylated HA is immobilized on the azide groups of the PEG3000 via a copper-mediated click reaction. By modifying the PEG2000 to PEG3000 azide ratio the amount of immobilized HA can be tuned.

3.2.1 Adhesive surfaces – integrin addressing peptidomimetics

According to Figure 15 gold-nanostructured glass surfaces need to be first generated by block copolymer micelle nanolithography (BCML) (see 1.5). It has been reported that a spacing of gold-nanoparticles and inter ligand distance between 28 and 58 nm is necessary to induce integrin-mediated adhesion of several different cell types (Arnold *et al.*, 2004; Lohmüller *et al.*, 2011; Oria *et al.*, 2017). A spacing above 73 nm prevents cell adhesion and subsequent spreading. Therefore, I aimed for a spacing in between 28 and 58 nm. As proved by scanning electron microscopy (SEM) images I successfully optimized experimental conditions to generate glass surfaces with a gold spacing of 52 ± 9 nm and a hexagonality as high as 69 % (Figure 16). The average gold particle diameter was 10.9 ± 1.8 nm.

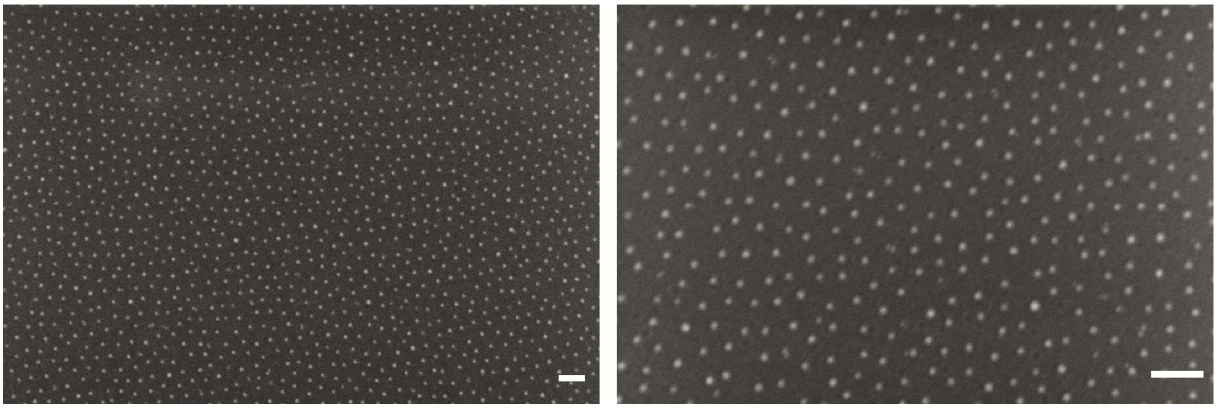

Figure 16: SEM images of gold-nanostructured glass surfaces manufactured via BCML. Representative images of test samples. Samples were carbon-sputtered and imaged via SEM at different magnification (left 50,000 and right 100,000x) to analyze interparticle distance and order parameter. Mean gold-nanoparticle spacing is 52 ± 9 nm with a hexagonality of 69 %. Average gold particle diameter is 10.9 ± 1.8 nm. Scale bar 100 nm.

As binding motifs within the ECM are limited, often one and the same binding motif can be recognized by different integrin heterodimers. Therefore, I decided to focus on integrin families (i.e., fibronectin and laminin family) rather than single integrins. To address integrins of the fibronectin binding family I chose c(RGDfV). c(RGDfV), in the following referred to as cRGD, is a modification of the preserved and highly conserved RGD peptide, the general binding motif of fibronectin, which also occurs in other ECM molecules such as collagen I. Also, cRGD has been employed as a binding ligand in gold-nanostructured glass surfaces (Cavalcanti-Adam *et al.*, 2006). For the laminin binding family, no evaluated peptidomimetics are described. According to literature the peptide sequences EPDIM and NKDIL, both binding motifs of the transforming growth factor β (TGF-β) dependent cell adhesion molecule βig-h3, might be promising synthetic ligands. Both have been shown to sufficiently mediate cell adhesion via α3β1 on coated glass surfaces (Kim *et al.*, 2000; Bae *et al.*, 2002). However, so far both peptides have only been used for simple surface coating without being further processed.

Therefore, I first aimed to test whether EPDIM can be recognized by cells after functionalization and thus can serve as a cell binding ligand in my future experiments.

To ensure an open and active conformation of the adhesive peptidomimetic EPDIM and to prevent steric hindrance in between different adjacent ligands bound to the same gold-nanoparticle, an additional spacer had to be added to the adhesive peptide (Mas-Moruno *et al.*, 2016). Different spacers are commonly used. As previous successful studies of our research group relied on the immobilization of cRGD via a PEG spacer, I decided to also use a pegylated EPDIM peptide. For the linear peptide EPDIM, its functionality can be differentially affected, depending on an N- or C-terminal linker installation.

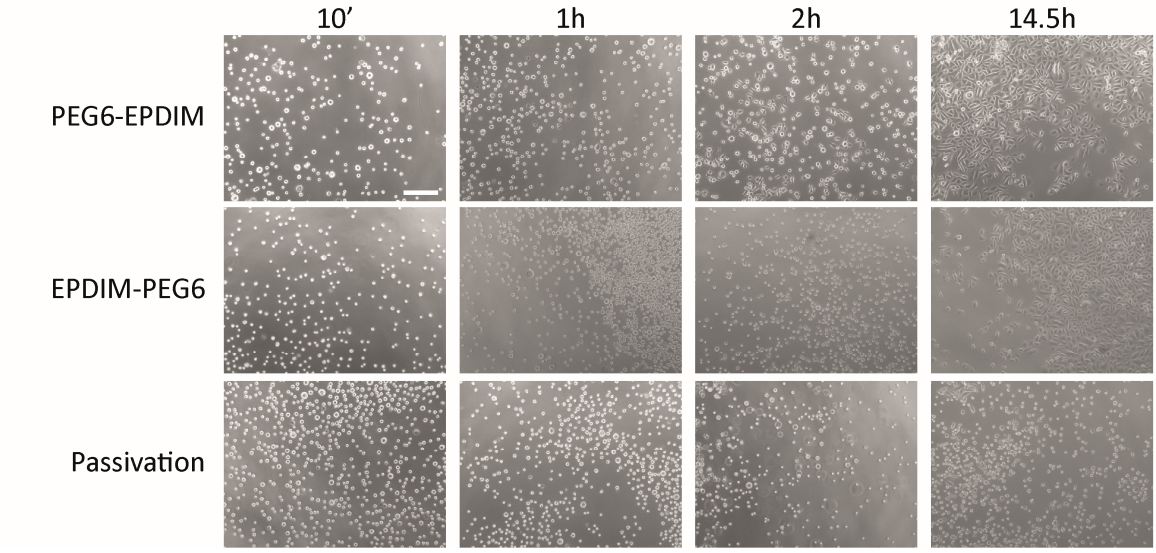

Figure 17: Spreading of NHEK cells over time on EPDIM functionalized glass surfaces. Gold-nanostructured glass surfaces were PEG2000 passivated and functionalized with either PEG6-EPDIM or EPDIM-PEG6. 1.5 x 104 cells/cm2 (NHEK, primary keratinocytes) were seeded and cell adhesion and subsequent spreading was observed for a total of 15 h. Scale bar: 200 µm.

In order to identify the functionality of EPDIM, which so far has not been used as a binding ligand in such kind of experimental set-up, I tested in preliminary experiments if EPDIM peptide functionalized glass surfaces enable the adhesion of relevant cells. EPDIM peptides were immobilized on gold nanostructured surfaces either via their C- or N-terminus. Bae *et al.* recorded in prior experiments cell adhesion on EPDIM-coated surfaces (with EPDIM not being attached to a linker). For this, they used primary keratinocytes (normal human keratinocytes, NHEK) (Bae *et al.*, 2002). Accordingly, I investigated the adhesive properties of EPDIM with analogous keratinocytes. Gold-nanostructured glass surfaces were prepared, PEG2000 passivated and functionalized with the two different EPDIM variants, with the spacer either linked on the N- or C-terminus: (1) PEG6-EPDIM and (2) EPDIM-PEG6 (Material and Methods, (Table 9). Glass surfaces were glued into prepared well plates. 15 x 104 cells/cm2 were seeded into each well and NHEK adhesion and subsequent spreading was observed. NHEK cells attached within the first hour and spreading started between 1-2 h after seeding independently of

employed EPDIM species. However, cells seeded on PEG6-EPDIM functionalized surfaces spread slightly faster compared to cells attached on EPDIM-PEG6 (Figure 17). No cells spread on passivated surface where no binding ligand was provided, proving the binding ligand specific surface interaction of NHEKs. Based on these results the N-terminal pegylated EPDIM was used in all following experiments.

Next, nanostructured glass surfaces were functionalized with cRGD or EPDIM to directly compare HaCaT cell adhesion and spreading on these different surfaces. To additionally compare the adhesion quality of the two implemented binding ligands with their respective full ECM proteins, I additionally prepared surfaces which were coated with laminin 332 (which interacts with α3β1 integrins, as has been shown for the EPDIM binding motif) and fibronectin or collagen I (which both contain the RGD binding motif). Furthermore, I provided collagen I gels which more resemble a dermal environment and have been successfully deployed in past experiments as a substrate to mediate keratinocyte migration (Safferling *et al.*, 2013). In principle, all applied ECM proteins represent different stages of wound healing (see 1.2.1). Figure 18 depicts HaCaT cell adhesion over a total recording time of 30 h. I observed that a first cell adhesion starts within the first two hours after seeding. Subsequent cell spreading is initiated from 5 h on. After 15 h, HaCaT cells being seeded on laminin 332 and cRGD are fully spread. Cells on collagen I, fibronectin and EPDIM spread after 20 h. HaCaT cells seeded on collagen I gels exhibited a smaller cell area at the end of the adhesion experiment indicating that these cells do not spread as widely as cells examined on the other substrates. This is in accordance with published experiments where cell spreading correlates with substrate rigidity. The softer the substrate, the less cells are spread (Li, Han and Zhao, 2014; Oria *et al.*, 2017).

To conclude, successful HaCaT cell adhesion on functionalized gold-nanostructured glass surfaces was verified by a cell adhesion assay. Therefore, cRGD as well as EPDIM were shown to be suited binding ligands in a minimalized system where the full ECM proteins are replaced by their binding motifs.

cRGD has been successfully utilized as an adhesive ligand for fibroblasts on functionalized gold-nanostructured glass surfaces in the past (Cavalcanti-Adam *et al.*, 2007). The peptide EPDIM so far has only been used for simple surface coatings, without being further processed (Kim *et al.*, 2000; Bae *et al.*, 2002). In order to immobilize EPDIM on gold nanostructured glass surfaces, it needs to be further modified: First with a thiol functionalization for immobilizing the peptide on the gold-nanostructured surfaces. And second with a spacer to prevent sterical hindrance between different adjacent ligands bound to the same gold-nanoparticle, and to ensure an open, active conformation of the adhesive peptidomimetic (Mas-Moruno *et al.*, 2016). Cell adhesion experiments with NHEK proved functionality of the EPDIM sequence with an N- or C-terminal PEG6 linker. The experiments further showed that the peptide with an N-terminal linker mediated a faster cell spreading compared to a C-terminal linker and

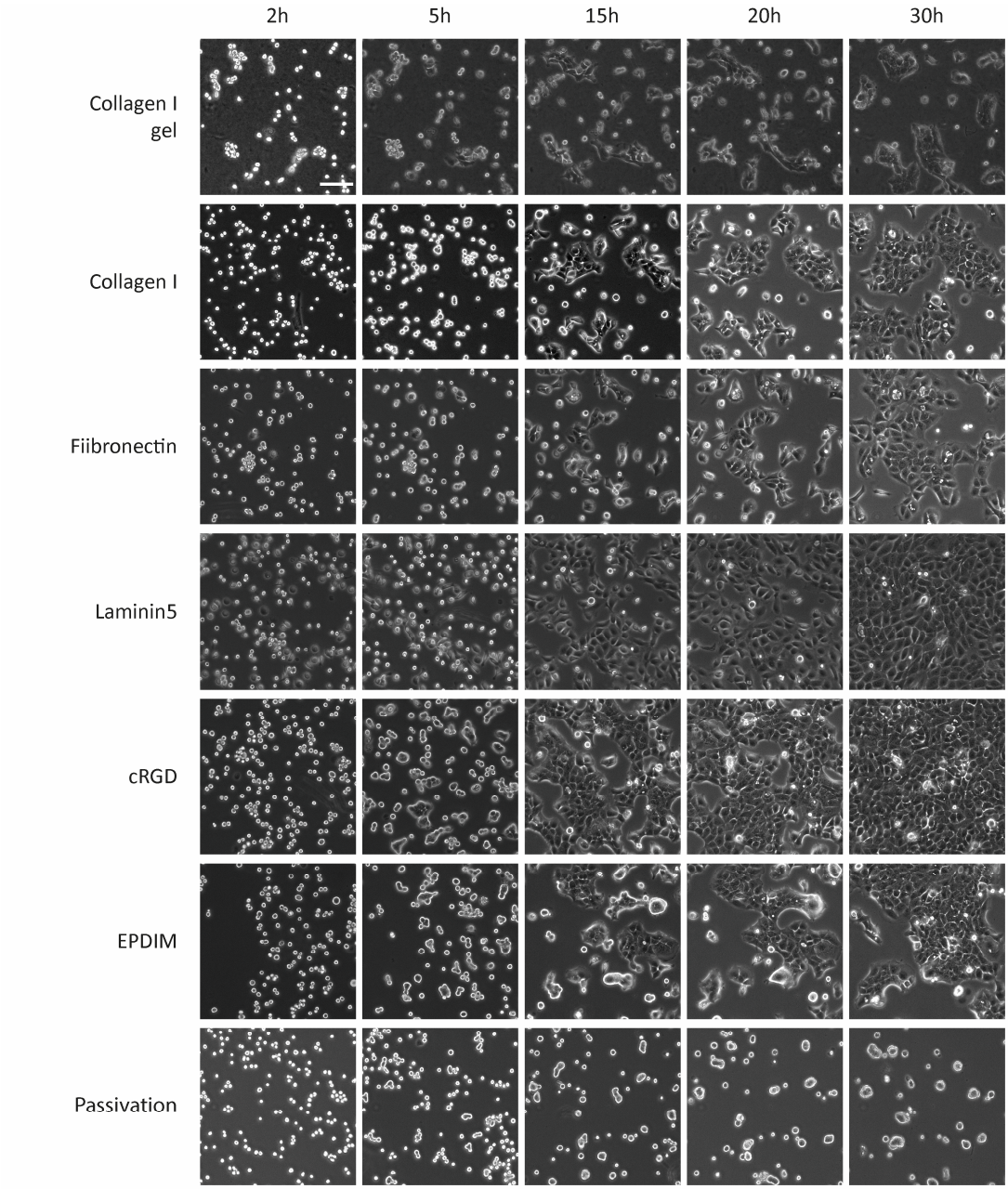

Figure 18: Spreading of HaCaT cells over time on collagen I gels, differently coated or gold-nanostructured and functionalized glass surfaces. Indicated substrates were prepared and 5 x 103 cells/cm2 were seeded for each condition. Cell adhesion and spreading was observed via live-cell phase contrast time-lapse imaging. Scale bar: 100µm. *Note: due to the 3D structure of the collagen I gel the background in these samples is higher leading to a lower contrast to the cells.*

thus has slightly better adhesive properties (Figure 17). Former research results indicate that Asp as well as Ile are essential for EPDIM's adhesive properties (Kim *et al.*, 2000). Thismight give a hint towards the improved adhesive properties of PEG6-EPDIM compared to EPDIM-PEG6. For the latter, only one additional amino acid separates Asp and Ile from the PEG-linker, whereas the former has a distance of two amino acids and this might be sterically advantageous for cell recognition and interaction.

Comparing the two binding ligands cRGD and EPDIM directly showed, despite a similar time needed for a first adhesion, a faster full spreading of cells having been seeded on cRGD than on EPDIM

functionalized surfaces. cRGD is an improved adhesive ligand based on the highly conserved RGD motif. cRGD's D-amino acid residue as well as its cyclisation lead to a high stability as well as activity, both essential for biological applications of several days (Aumailley *et al.*, 1991; Mas-Moruno *et al.*, 2016). In adhesion inhibiting studies cRGD outcompetes its linear form by 20-100 fold, depending on the substrate and cell line (Aumailley *et al.*, 1991). Compared to that, EPDIM as an adhesive ligand is a linear amino acid sequence, which has not been further processed and thus it is not surprising that in its present form it does not mediate cell adhesion in an optimized manner.

3.2.2 End-alkylated HA binds to free azide groups

According to Minsky *et al.* alkylated HA can be immobilized via a copper(I) catalyzed click reaction (copper(I)-catalyzed azide alkyne cycloaddition) to surface-bound azide groups (Minsky, Antoni and Boehm, 2016). Hence, in order to click HA on PEG2000/PEG3000azide passivated glass surfaces, an alkyl group is first introduced into HA. Due to the number of disaccharides needed for HA receptor recognition and increasing conformational complexity with rising MW of HA accompanied with exacerbated hyaladherin recognition (for details please be kindly referred to the introduction), I aimed to immobilize short HA of 5 kDa (about 13 disaccharide units) and 10 kDa (about 26 disaccharide units). By this, potential conformational effects of longer HA polysaccharides are circumvented, and only one hyaladherin per HA polymer is addressed.

To prove that HA was successfully end-alkylated and thus binds to surface-bound azide groups via a copper(I) catalyzed click reaction, label-free quartz crystal microbalance with dissipation monitoring (QCM-D) was performed. First, a spontaneous self-assembled monolayer (SAM) consisting of a mixture of the oligoethylenglycols (OEGs) EG_3OH and EG_6N_3 was formed on gold coated QCM-D crystals. Changes in frequency (Δf) from 0 to -17 Hz after 16 min indicate the successful formation of the SAM (Figure 19). Next, end-alkylated 5 kDa HA (5kDaHAeAlkylated) and 10 kDa HA (10kDaHAeAlkylated) respectively were added, first without click reaction buffer and after with click reaction buffer in order to catalyze the copper(I)-catalyzed azide-alkyne cycloaddition. Without click reaction buffer, the frequency only slightly decreased (about 10 Hz) for 5kDaHAeAlkylated and no change was observed for 10kDaHAeAlkylated. Only upon provision of the click reaction buffer a clear decrease in frequency (50 Hz for 5kDaHAeAlkylated and more than 74 Hz for 10kDaHAeAlkylated) and increase in dissipation was observed. Addition of 0.5 % (w/v) bovine serum albumin (BSA) did not change (Δf) nor dissipation (ΔD). Thus, BSA was not adsorbed on the surface and the passivated background of the OEG SAM was therefore maintained despite binding of HA for both alkylated 5 and 10 kDa HA (Figure 19). This is in accordance to Harder *et al.* who showed that a minimum of three repeating units of EGs were sufficient to inhibit protein adsorption (Harder *et al.*, 1998).

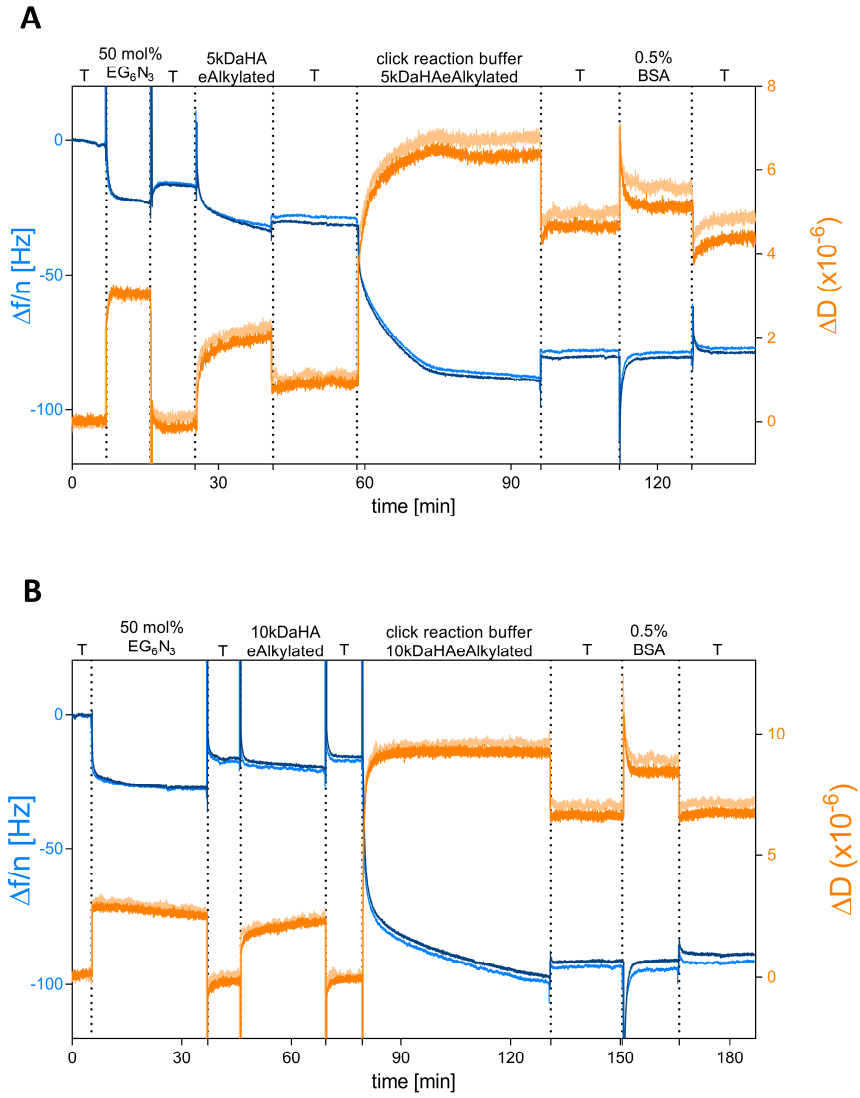

Figure 19: 5 and 10 kDa end-alkylated HA binds to EG_3OH/EG_6N_3 layers. SAMS of EG3OH and EG6N3 (1:1 mol%) were adsorbed on gold QCM-D sensors. Next, 2.5 mg/mL end-alkylated 5 kDa HA (5kDaHAeAlkylated, A) or 10 kDa (10kDaHAeAlkylated, B)) was added first without click reaction buffer and then with click reaction buffer in order to catalyze the copper(I)-catalyzed azide-alkyne cycloaddition. QCM-D graph of the seventh overtone (n=7), change in frequency (Δ f/n, shades of blue) and dissipation (Δ D, shades of orange) were monitored over time. T: 0.1 M TRIS buffer pH 8; depicted are two replicates (visualized by different color shades).

The frequency for end-alkylated HA alone (without the addition of click reaction buffer) decreased because the cycloaddition can occur spontaneously. However, this reaction is much slower than it would be in presence of copper(I), as can be observed in Figure 19 and Figure 46 (Appendix) (Li and Zhang, 2016). Interestingly, this Δf is higher for 5kDaHAeAlkylated than for 10kDaHAeAlkylated (or 60kDaHAeAlkylated, Appendix, Figure 46). A potential explanation for this observation is that the probability that the HA-bound alkyne group meets the azide group and thus the uncatalyzed azide-alkyne cycloaddition takes place is higher for the shorter 5 kDa polymer than for the longer 10 kDa (or 60 kDa HA) due to sterical hindrance.

For 5 kDa HA, the shortest amount of time was needed until Δ f/n and Δ D reached a stable plateau upon administration (defined as no measured increase or decrease in Δ f/n and Δ D for 5 minutes). Here, the plateau was reached within less than half an hour. In contrast, 10 and 60 kDa needed more time until a plateau was established. Again, this might be due to sterical interference, which is higher for 10 or 60 kDa and lower for 5 kDa HA. As expected, due to the hygroscopic properties of HA, the higher the MW of HA is, the higher the effect on viscoelastic properties of HA on surface is, which is expressed by higher Δ D upon HA binding (5kDa: 4 x 10^6; 10 kDa: 7 x 10^6; 60 kDa: 15 x 10^6).

To conclude, this experiment proved successful alkylation of both, 5 kDa and 10 kDa HA as well as its successful immobilization on terminal azide groups via a copper(I)-catalyzed azide-alkyne cycloaddition. BSA administration had no effect on Δf or ΔD, thus the SAM passivating capacities are preserved, despite immobilization of HA. These results are in accordance with and an extension of previously published data. Minsky *et al.* showed that 10 kDa HA specifically binds to surface bound azide groups via an introduced alkyl moiety, whereas non-functionalized HA did not (Minsky, Antoni and Boehm, 2016).

3.2.3 Number of azide groups determines surface-bound HA concentration

As illustrated in Figure 15 the surface bound HA and thus its concentration on the surface is regulated via the number of azide groups presented by the glass surface. However, due to differences in the radius of gyration (R_g) it is expected that the correlation between free azide groups and the number of HA molecules bound to the surface is not linear. Instead, the surface is eventually saturated with the larger HA molecules. QCM-D measurements were performed to determine at what azide ratio the surface would be saturated with HA molecules. For this purpose, the amount of surface-bound azide groups was varied and the resulting saturation was traced by comparing the Δ f (as well as Δ D) upon administration of alkylated HA.

By varying the ratio of EG_3OH to EG_6N_3 on the QCM-D sensor, the theoretical number of alkylated HA molecules bound to the surface was directly affected, which was in turn expressed in frequency and dissipation changes. Gold QCM-D sensors with nine different EG_6N_3 mol% ratios were prepared and end-alkylated HA (5 and 10 kDa) was immobilized via a copper(I)-catalyzed azide-alkyne cycloaddition directly performed on the QCM-D crystal. Figure 20 depicts the frequency and dissipation changes in relation to the EG_6N_3 ratio.

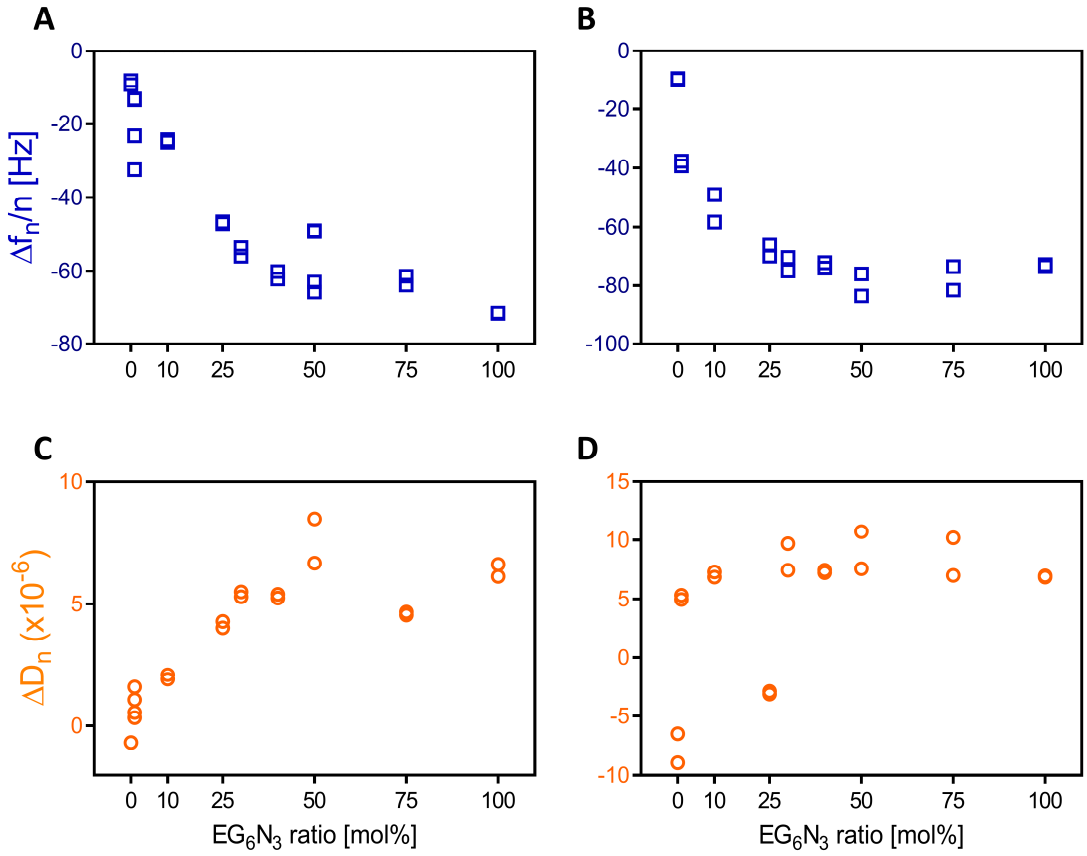

Figure 20: Binding of end-alkylated 5 kDa and 10 kDa HA to surfaces with varying ratios of EG_3OH/EG_6N_3 layers. SAMS of EG3OH and EG6N3 (with EG6N3 ratios varying from 0 to 100 mol%) were adsorbed on gold QCM-D sensors. Values depict the differences in mean frequency (Δ f/n; graph A, B) and dissipation (Δ D, graph C, D) before and after addition of end-alkylated 5 kDa HA (A, C) and 10 kDa (B, D). QCM-D graph of the seventh overtone is used for analysis. Each mean is calculated by a time interval of 5 minutes. Duplicates for each condition.

As expected, azide presenting surfaces were eventually saturated with HA molecules bearing an alkyl moiety. Comparing 5 and 10 kDa HA reveals a higher change in frequency for 10 kDa than 5 kDa upon saturation, most probably due to the higher MW (Figure 20 A, B). Interestingly, saturation in terms of ΔD occurred faster for 10 kDa (at ~10 mol% EG_6N_3) than for 5 kDa (at ~25-30 mol% EG_6N_3) (Figure 20 C, D). This observation most likely emerges from the different lengths of both HA species with the 10 kDa being about twice as long as 5 kDa. Due to the increased polymer length more energy is dissipated with less molecules bound to the surface, compared to the shorter 5 kDa HA. Thus, saturation was reached faster (as regards number of azide groups) for 10 than for 5 kDa HA. Moreover, saturation in dissipation occurred for 10 kDa already at half the amount of the azide groups than for 5 kDa, representing the doubled length of 10 kDa once again. Additionally, more energy was dissipated in case of the longer 10 kDa HA compared to the 5 kDa HA, leading to higher maximally measured ΔD.

Table 20:Values for measured frequency shifts and mass changes for end-alkylated 5 kDa (A) and 10 kDa (B) HA adsorbed to QCM-D gold crystals with varying ratios of EG_3OH/EG_6N_3. Δ m was calculated based on Δf by applying the energy method. For ΔD and Δf mean ± standard deviation (SD) are stated. m, n and HA/µm² are calculated from the mean for Δ f of the seventh overtone. If not stated differently calculated values are per cm².

HA [kDa]	EG_6N_3 [mol%]	ΔD (x10⁶)	Δf [Hz]	Δ m [ng]
5	0	-0.68 ± 0.00	8.75 ± 0.56	154.38 ± 9.91
	1	0.88 ± 0.48	20.60 ± 7.93	363.35 ± 139.99
	10	1.99 ± 0.09	24.62 ± 0.34	434.27 ± 5.93
	25	4.16 ± 0.13	46.81 ± 0.22	825.91 ± 3.89
	30	5.39 ± 0.10	54.78 ± 1.13	966.52 ± 20.02
	40	5.32 ± 0.08	61.12 ± 1.05	1078.32 ± 18.57
	50	5.68 ± 2.00	56.73 ± 7.69	1000.87 ± 135.69
	75	4.61 ± 0.06	62.61 ± 1.21	1104.53 ± 21.33
	100	6.37 ± 0.25	71.62 ± 0.14	1263.63 ± 2.48
10	0	-0.64 ± 0.47	9.52 ± 1.14	167.89 ± 20.11
	1	5.15 ± 0.17	38.51 ± 0.77	679.32 ± 13.57
	10	7.08 ± 0.22	53.68 ± 4.60	947.12 ± 81.22
	25	7.82 ± 1.36	67.77 ± 3.47	1195.63 ± 61.27
	30	8.58 ± 1.12	72.68 ± 2.28	1282.24 ± 40.29
	40	7.34 ± 0.11	73.04 ± 0.92	1288.56 ± 16.27
	50	8.71 ± 2.00	79.75 ± 3.82	1406.96 ± 67.37
	75	8.61 ± 1.59	77.46 ± 4.04	1366.63 ± 71.33
	100	6.91 ± 0.05	73.10 ± 0.32	1289.60 ± 5.73

As described in detail in 1.9 (Material and Methods) the absorbed mass can be determined based on the change in frequency. Table 20 summarizes ΔD, Δf and respective calculated absorbed mass, Δm. Correlating with the measured Δ f, the Δ m on the quartz crystal increased with increasing EG_6N_3 mol%. For 5 kDa, Δ f and thus Δ m rose from 0 to 100 mol% EG_6N_3, indicating that complete saturation of the surface might not be reached and thus the number of HA molecules bound to the surface is continuously increasing with increasing azide moieties presented. Albeit, the decrease in frequency slows down at higher EG_6N_3 mol%. In contrast, Δ D are saturated from around 30 mol% EG_6N_3 (ΔD = 5.39 ± 0.10) on.

Applying 10 kDa HA on the surfaces revealed a saturation at a Δ f of about 70 Hz, which was reached upon 25-30 mol% EG_6N_3 corresponding to a mass of 1195.63 to 1282.24 ng. Δ D were saturated from 10 mol% EG_6N_3 on and ranged within 7.08 (x10⁶) to 8.71 (x10⁶).

Based on these results, OEG-azide and respectively PEG-azide ratios of 0, 10 and 50 mol% are employed for future (cell) experiments to cover the dynamic range of surface saturation. Additionally, by using short HA but in a high density the number of binding sites per area can be increased and thus theoretically a longer polymer can be elegantly mimicked. It must be experimentally determined though, whether the low persistence length and thus the high rigidity of especially small HA polymers would allow for enough spatial flexibility to mimic a longer polymer and e.g. mediate cellular receptor cluster formation.

The Sauerbrey equation and all derived equations to calculate the mass bound to the crystal surface during QCM(-D) measurements are only valid for oscillation in air and for rigid masses. Additionally, molecules bound to the quartz crystal are presumed to have the same properties as quartz (Stambaugh *et al.*, 2020). Once experiments are performed in an aqueous solution with the formation of viscoelastic films, relations are much more complex, as the crystal's oscillation is not only affected by the adsorbed mass itself but also by mass-environment interactions such as water binding and viscoelasticity. HA is highly hygroscopic and can trap high amounts of water which can be up to 100 fold of its weight (Anderegg, Simon and Averbeck, 2014). Thus, Δm derived from QCM-D measurements cannot solely lead back to HA but are the sum of HA, charged ions as well as other components which might be entangled in the HA network.

3.2.4 Immobilized HA is bioactive

Hyaladherins interact with HA via its different side moieties. By immobilizing HA on surfaces, these moieties need to be chemically modified beforehand and by this, recognition sites might be sterically masked upon immobilization, thus providing only poor accessibility for hyaladherins. As bi-functionalized glass surfaces are meant to elucidate the interplay between HA and other ECM molecules and its effect on cellular processes, it is crucial that HA can be recognized by cellular hyaladherins, such as CD44, despite its immobilization. HA with a MW of 5 kDa as well as 10 kDa is expected to have a linear conformation (Weigel and Baggenstoss, 2017), which is not affected by the alkylation strategy applied, as the modification is introduced at the end of the polysaccharide. Hence, binding motifs within immobilized HA are supposed to be accessible even though no additional linker is used to relax potential sterical hindrance. The accessibility of binding motifs within surface-bound HA can be proved by performing QCM-D measurements. Aggrecan is a hyaladherin which interacts with HA via its link binding domain. Therefore, binding of the hyaladherin aggrecan was elucidated employing SAMs with 0, 10 and 50 mol% EG_6N_3 and subsequent HA immobilization. Interestingly, no aggrecan binding was observed in initial measurements following the established protocol. Only upon adding two additional washing steps, with 300 mM NaCl and 1 mM EDTA in PBS. a slow but steady increase in dissipation of 0.375×10^6 and respectively 0.500×10^6 was found for surfaces with 10 and 50 mol% EG_6N_3 and

5kDaHAeAlkylated within 82 minutes. For surfaces with 10 and 50 mol% EG_6N_3 and 10kDaHAeAlkylated a dissipation of 0.450 x 10^6 and respectively 0.425 x 10^6 was observed within 99 and 85 minutes, respectively (Figure 21).

Thus, binding sites for hyaladherins were accessible in the presence of immobilized 5 kDa and 10 kDa HA respectively. As expected, no ΔD was observed for surfaces with 0 mol% of EG_6N_3 because due to the lack of azide groups no alkylated HA could bind to the surface (Figure 21).

The minimal HA length needed to mediate aggrecan binding has been shown to be ten disaccharide units (Omelyanenko, Ilyich and Pavlovich, 2016). 5 kDa HA has around 13, and 10 kDa around 26 disaccharides. Thus for both MWs the polymer is long enough to enable aggrecan binding. It is reported that due to the size of aggrecan (about 210-250 kDa) the proteoglycan only binds every 50-60 disaccharides in biological systems (Omelyanenko, Ilyich and Pavlovich, 2016). Therefore, it is expected that only one aggrecan molecule can bind per HA for both, 5 and 10 kDa. It is pivotal to mention that due to the multivalent character of HA, aggrecan binding can be shifted alongside the 10 kDa HA polymer but not the 5 kDa, as the 5 kDa HA holds the minimal number of disaccharide units needed for binding.

Upon binding of aggrecan to the HA network, aggregates are formed leading to an increase in viscosity and, thus, loss of energy, i.e. dissipation rises, as observed in the above described experiments (Omelyanenko, Ilyich and Pavlovich, 2016) (Figure 21). Dissipation upon aggrecan adhesion for immobilized 5 kDa HA rises the more HA is presented on the surface (about 30 % from 10 % HA to 50 % HA). In contrast, for 10 kDa dissipation is comparable between 10 % and 50 % HA. This observation could be explained by a saturation with aggrecan already upon a 10 % surface decoration of 10 kDa HA, but not 5 kDa, with half the polymer length of 10 kDa (assuming a rod-like only structure of HA). Therefore, distances in between 5 kDa HA and hence the number of binding sites for aggrecan is higher and subsequently saturation is reached later.

To sum up, I showed aggrecan binding to immobilized 5 and 10 kDA HA presented at different surface concentrations and thus bioactivity of immobilized HA. This observation is in accordance to previously published data (Minsky, Antoni and Boehm, 2016). Moreover, I showed that the aggrecan-based bioactivity assay for immobilized HA can be performed directly on the QCM-D crystal. For this, simply two additional washing steps with NaCl and EDTA needed to be integrated to successfully change the buffer system directly on the crystal. Beyond previous results, I showed the bioactivity of immobilized 5 kDa HA and the correlation between bioactivity and concentration of immobilized HA. For all parameters no additional linker within the chemically modified HA polymers was needed to preserve bioactivity of immobilized, end-alkylated HA. The data presented revealed a saturation with surface-bound aggrecan already at a surface decoration of 10 % of 10 kDa HA. On the contrary, 5 kDa HA increases aggrecan interference with the adsorbed HA network from 10 to 50 %. Therefore, all

further experiments were performed with 5 kDa HA to conserve the feature to fine tune the set-up in regard to hyaladherin-HA interactions.

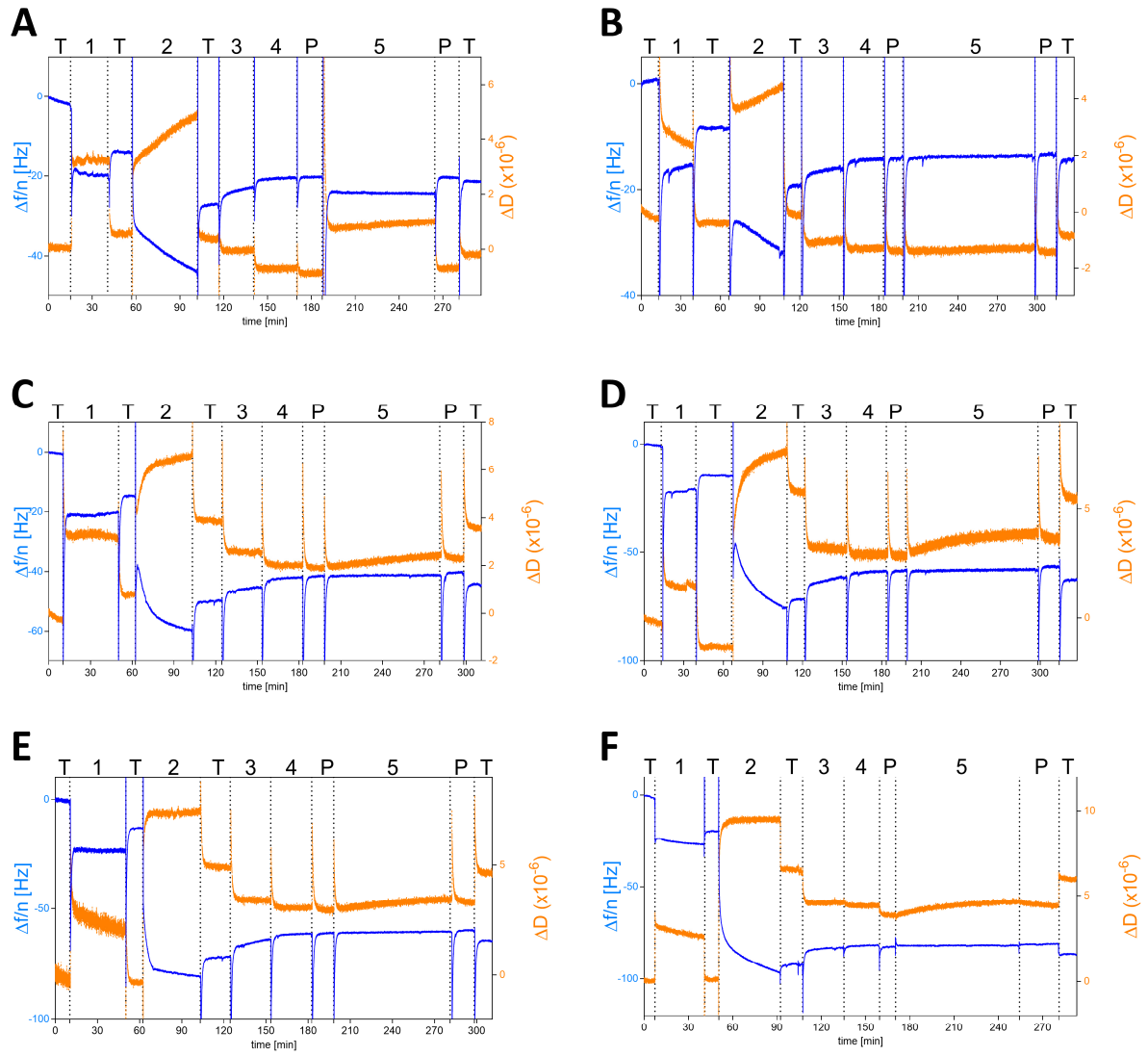

Figure 21: Aggrecan binding on immobilized end-alkylated 5 and 10 kDA HA. (A, B) 0 mol% EG6N3, (C,D) 10 mol% EG6N3 and (E,F) 50 mol% EG6N3. SAMs of varying EG3OH to EG6N3 ratio were adsorbed on gold QCM-D sensors. Next, end-alkylated 5 or 10 kDa HA (2.5 mg/mL) dissolved in click reaction buffer was immobilized on the surface. Washing with 300 mM NaCl and 1 mM EDTA in PBS was folllowed by addition of 100 µM aggrecan to examine the accessibility of hyaladherin binding sites. QCM-D graph of the seventh overtone, change in frequency (Δ f/n) and dissipation (Δ D) were monitored over time. T: 0.1 M TRIS buffer pH 8, P: PBS, 1: mol% EG6N3 (A, B: 0 mol%; C,D: 10 mol%; E, F: 50 mol%), 2: click reaction buffer with 5 kDa HA (A, C, E) and 10 kDa (B, D, F), 3: 300 mM NaCl, 4: 1 mM EDTA, 5: 100 µM aggrecan in PBS; representative data of two replicates per condition.

It has been shown that CD44, the main receptor for HA in keratinocytes needs a minimum of ten disaccharide units, identical to aggrecan (Day and Prestwich, 2002). Thus, it is expected that bioactivity

of immobilized HA, proven by aggrecan binding, can be transferred to CD44 as well as to other hyaladherins with comparable polymer lengths needed for recognition.

3.2.5 How many end-alkylated HA molecules would theoretically bind to azide presenting glass surfaces?

In order to generate bi-functionalized glass surfaces where cells only interact with presented binding motifs, the space in between binding motifs needs to be filled with a cell-repellent polymer layer. To successfully prevent cell adhesion, PEG of 2000 Da or an equivalent with higher MW is sufficient (Blümmel *et al.*, 2007). With the aim to transfer the findings of immobilized HA on gold-coated QCM-D crystals to glass surfaces where PEG2000 and PEG3000azide are covalently bound to glass via a silane moiety, a theoretical calculation is made to determine the number of end-alkylated HA molecules bound to PEG2000 and PEG3000azide passivated glass surfaces and hence calculate the number of HA molecules per area. Therefore, a theoretical model which describes the experimental results (see 3.2.3) achieved by applying the OEGs EG_3OH and EG_6N_3 on gold-coated QCM-D crystals needs to be created. To determine the theoretical expected number of end-alkylated HA molecules on surfaces decorated with a mixture of EG_3OH and EG_6N_3, a few approximations are made. First, the arrangement of EG_3OH and EG_6N_3 chains is expected to be vertically-only, leading to a brush-like arrangement of the polymers, where longer polymers protrude shorter polymers as suggested by Mehne *et al.* (2008). Second, calculations are made assuming a mono-molecular surface coverage with EG_3OH and EG_6N_3 chains where the gyration radius is taken to be identical for both PEG species. For this, the dimensions of EG_6N_3, as the molecule with the reactive species (N_3) are applied. Third, molecular interactions only occur in between the functional groups (alkyne and azide), no additional chemical or physical interactions take place and surface coverage with PEG or HA is achieved by a perfect layering of an HA monolayer on top of the PEG monolayer. And fourth, an interaction between the functional groups of respective molecules (HA-alkyne and PEG-azide) is expected to occur always in their centers, all involved molecules are assumed to be rigid, hence HA species perfectly orient vertically on top of azide groups bearing PEG molecules.

The R_g for PEG chains increases with rising chain-length due to increased helicity (Oelmeier, Dismer and Hubbuch, 2012). In order to determine R_g, I applied the following formula for PEG in water (Devanand and Selser, 1991; Kawaguchi *et al.*, 1997), which has been shown to be in good accordance with simulated radii of gyration for different PEG lengths (Lee *et al.*, 2009; Oelmeier, Dismer and Hubbuch, 2012).

$$R_g[nm] = 0.02(MW_{(PEG)})^{0.58} \quad (4)$$

Subsequently, R_g of EG_6N_3 with a MW of 414 Da is 0.659 nm. Therefore, the area captured by a single EG_6N_3 molecule is 1.32 nm in diameter. Next, the number of PEG molecules which is needed to fully cover a plane squared surface (like a glass surface) is determined. For this, the area of a squared surface of a defined area of 1 μm^2 is divided by the area of a single PEG molecule (5)

$$A_{\mathrm{EG6N3}}[nm^2] = \pi R^2_{g(\mathrm{EG6N3})} \tag{5}$$

This leads to a maximal molecule number of 732066 EG_6N_3 molecules per μm^2. The grafting density (i.e. surface coverage) of ethylene glycol (EG) depends on its polymer length. Zhu *et al.* found a grafting density of 92 % at a MW of around 300 Da and of 35 % at a MW of 1000 or 2000 Da (Zhu *et al.*, 2001). Consequently, for EG_6N_3 538800 molecules are calculated. Since the EG_6N_3 molecules will be employed at a ratio of 10 or 50 mol%, the number of molecules is calculated accordingly. The yield of a copper(I)-catalyzed azide alkyne cycloaddition is very high and ranges within 70-80 % (Aflak *et al.*, 2019). The protocol applied has been optimized within the group (Schenk *et al.*, 2014). Thus, an efficiency of 80 % was assumed, further reducing the number of EG_6N_3 molecules on the surface (Figure 22 A). Assuming that all molecules would be perfectly evenly distributed over the surface, the distance between adjacent molecules would be identical for all molecules (i.e. hexagonal distribution). Connecting adjacent molecules would give regularly ordered equilateral triangles with a side length *d*, representing the intermolecular distance (Figure 22 B).

As $A_{triangle}$ [nm^2] << A_{square} [μm^2] it is valid that

$$\sum_{i=1}^{n} A_{i,triangle} \approx A_{square} \tag{6}$$

with n = number of molecules per μm^2, $A_{i,triangle}$ the area of the equilateral triangles and A_{square} the area of the square covered by triangles. Inserting the formula for area calculation of an equilateral triangle gives equation (7) :

$$\sum_{i=1}^{n} \frac{\sqrt{3}}{4} \times d_i^2 \approx A_{square} \tag{7}$$

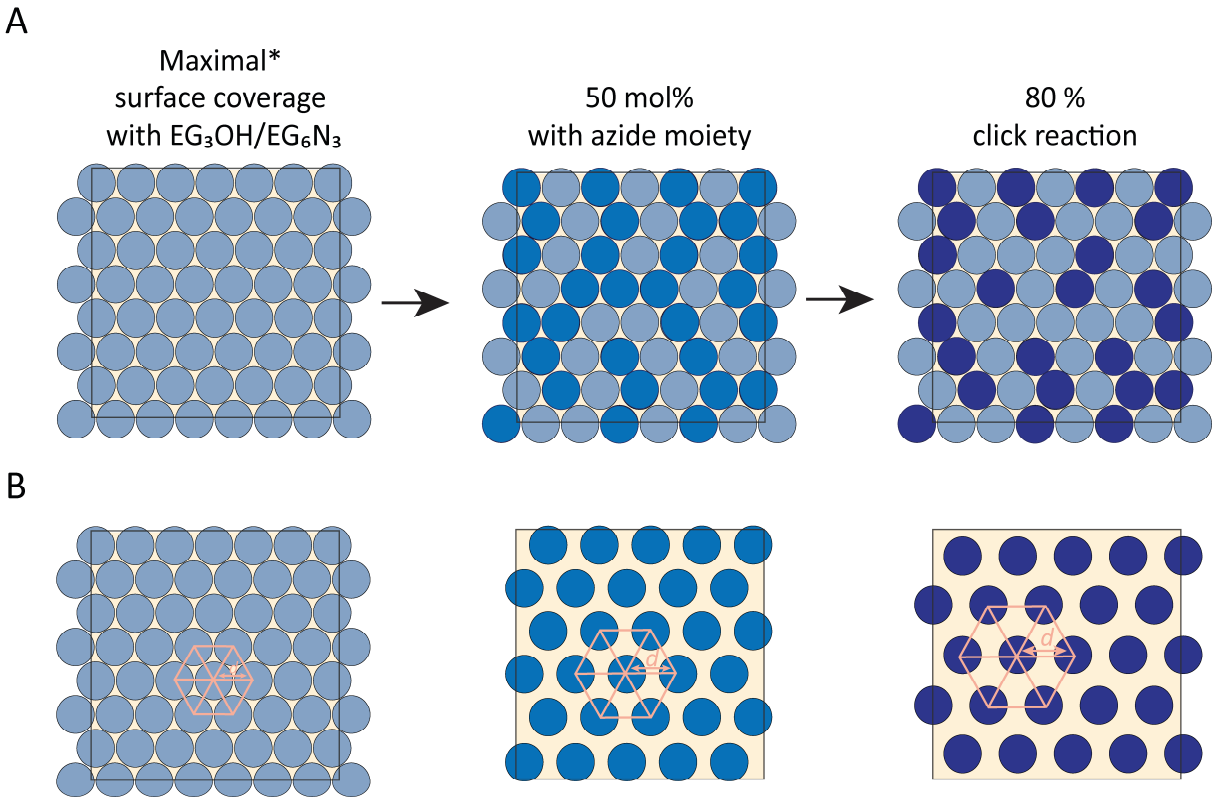

Figure 22: Scheme for calculation of molecule distances in relation to the total number of reactive molecules. (A) EG6N3 molecules arrange on a squared surface, resulting in a 92 % surface coverage. As only 50 mol% of all molecules carry an azide moiety only those can react with end-alkylated HA (blue circles). Additionally, assuming a click reaction efficiency of 80 %, only 80 % of those molecules with an azide moiety will react with end-alkylated HA (dark blue circles). (B) Assuming that all molecules would be perfectly evenly distributed over a squared surface (grey box), the distance in between adjacent molecules would be identical for all molecules (i.e. hexagonal distribution). Thus, connecting the center of adjacent molecules would give regularly ordered equilateral triangles, with a side length, and consequently the distance in between adjacent molecule centers of d. Note: molecules are assumed to be perfectly circular in the top view. d: distance; yellow: passivating background: EG3OH and non-reacting EG6N3.

As all triangles are assumed to be identical $d_i = d$. Thus, d can be calculated by:

$$d = \sqrt{\frac{A_{square}}{n} \times \frac{4}{\sqrt{3}}} \tag{8}$$

The resulting distances between PEG molecules of different lengths according to their surface coverage are listed in Table 21.

Table 21: Calculated number of molecules per µm² based on their R_g and 10 or 50 mol% surface coverage of molecules bearing azide groups. $N_{80\%}$ gives the number of reactive molecules assuming a click reaction yield of 80 %. Distance d in between molecules according to their surface coverage was calculated based on equation (8)**(9)**. Note that "max. coverage" is defined as a PEG grafting density of 93 % (indicated by asterisk).

Surface coverage	N per µm²	$N_{80\%}$ per µm²	d [nm]
Max. coverage*	1231548.90	538800.64	2.07
50 mol%	615774.45	269400.32	2.93
10 mol%	123154.89	53880.06	6.55

Following the approach of Bagby *et al.* (Bagby *et al.*, 2012), the R_g for 5 and 10 kDa HA is calculated based on the fitted equation from Takahashi *et al.* (1999):

$$R_g[nm] = 2.35\ [MW]^{0.57} \tag{9}$$

Thus, the R_g is 5.88 nm for 5 kDa HA and 8.73 nm for 10 kDa, which corresponds to a diameter of 11.76 nm for 5 kDa HA and 17.46 nm for 10 kDa. The hypothesis is that as soon as the diameter of HA exceeds the distance between EG molecules, a case of HA saturation is reached which is independent from the number of azide moieties bound to the surface. However, comparing the determined diameter of HA with the distance in between EG reveals that HA exceeds the distance of EG molecules for all calculated molecule numbers (see Table 21). This would mean that a saturation would already be reached at a surface coverage of 10 mol%. This is not in accordance with the measured data (Figure 20).

Therefore, assumed parameters are adjusted to make the model fit to the experimental data. However, if an EG coverage of only 40 % (instead of 92 % "full coverage") is assumed and based on the supposition that the click reaction efficiency is only 30 % (i.e. alkylated HA would only bind to 30 % of all available azide moieties), the model would partially describe the experimental observations as *d* is smaller than the diameter of HA only for 50 mol% but not for 10 mol% (Table 22) in case of 5 kDa HA but not 10 kDa.

Table 22: Calculated number of molecules per µm² based on their R_g and 10 or 50 mol% surface coverage of molecules bearing azide groups. N30% gives the number of reactive molecules assuming a click reaction yield of 30 %. Distance d in between molecules according to their surface coverage calculated based on equation (8)**(9)**. *Note that "max. coverage" is defined as a PEG grafting density of 40 % (indicated by asterisk).*

Surface coverage	N per µm²	$N_{30\%}$ per µm²	*d* [nm]
Max. coverage*	292826.43	87847.93	5.13
50 mol%	146413.22	43923.96	7.25
10 mol%	29282.64	8784.79	16.21

As mentioned above, the efficiency of a copper(I)-catalyzed azide alkyne cycloaddition is very high and reaches after optimization values of up to 80% (Schenk *et al.*, 2014). Hence it is very unlikely to assume a click reaction with an efficiency of only 30 %.

In the system presented a mixture of two EG species (EG_3OH and EG_6N_3) of different MW and thus of different radii should be arranged in a way to optimally cover a squared glass slide. This issue is a typical mathematical packing problem. To avoid a complex modelling procedure a simplification in the mathematical modelling was introduced by assuming all molecules to have the same size. Therefore, it cannot be excluded that true molecular distances are longer in reality.

Based on the assumptions of a maximal surface coverage of 92 % and a click reaction efficiency of 80 % I determined the theoretical number of EG molecules within 1 μm^2. A hexagonal molecule arrangement was assumed where the distance in between molecules was always identical (Figure 22). The distance between molecules was calculated by equation (6). There, the number of triangles was equated to the number of molecules. This is a simplification as for triangles at the boundary three molecules are needed to form a triangle. However, afterwards, only one additional molecule is needed to form another triangle (see Figure 23). Comparing the boundary cases to the total number of EG molecules (> 1 mio), this condition was neglected.

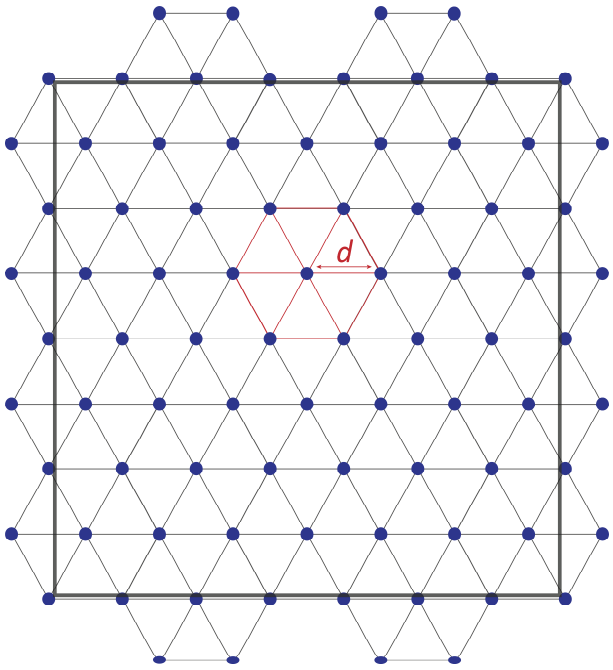

Figure 23: Needed molecule number to form an equilateral triangle with side length *d*.

Takahashi *et al.* calculated the R_g for HA with a MW from 59.4 to 6270 kDa based on data received from dynamic light scattering analysis (Takahashi *et al.*, 1999). This data results in the fitted equation (9) and was the basis to determine the gyration radius of end-alkylated 5 and 10 kDa HA. As

mentioned before, the conformation of HA shifts from a more rod-like structure to a more coiled-like structure with rising MW (Weigel, 2017). As the equation (9) is based on higher MWs of HA than applied in my experiments, it can be assumed that the gyration radii for smaller more rod-like HAs are rather overestimated. Additionally, the R_g of HA highly depends on the solvent and ion concentration (Kennedy *et al.*, 2000). As Takahashi *et al.* dissolved HA in 0.2 M NaCl while my experimental set-up requires Tris buffer as working solvent. Overall, it cannot be excluded that equation (9) cannot be applied to develop a model to describe my generated data.

Therefore, another theoretical approach was followed. This approach is based on the observation that the saturation region for end-alkylated HA of both 5 and 10 kDa is entered from 40 mol% EG_6N_3 on (Figure 20 and Table 20). This means that from 40 mol% EG_6N_3 on the diameter of 5 and 10 kDa HA exceeded the distance between adjacent EG_6N_3 molecules. Applying the before defined parameters a surface coverage of maximal 92 % and a click reaction efficiency of 80 % would result in 3.27 nm for *d* (Table 23). This means that according to the experimental data and upon application of the set parameters one end-alkylated HA polymer occupies an area with a diameter of 3.27 nm.

Table 23: Calculated number of molecules per µm² based on their R_g and 10 or 50 mol% surface coverage of molecules bearing azide groups. N80% gives the number of reactive molecules assuming a click reaction yield of 80 %. Distance d in between molecules according to their surface coverage based on equation (8)**(9)**.

Surface coverage	N per µm²	$N_{80\%}$ per µm²	*d* [nm]
40 mol%	269400.32	215520.25	3.27

Next, *d* was calculated for surfaces decorated with PEG2000/3000azide. Again, the MW of the molecule (3000 Da) with the reactive species (N_3) was utilized to determine R_g according to equation (4) to be 2.08 nm. Then, the number of surface-covering molecules was determined based on the assumption that the grafting density for higher polymer lengths is 35 % (Zhu *et al.*, 2001) before *d* could be calculated based on equation (8)(9). Estimated numbers of immobilized end-alkylated HA polymers and their respective *d* are modelled for several mol% and listed in (Figure 24 A). For all simulated values for *d,* the distance between reactive molecules is bigger than the estimated diameter for end-alkylated HA (Table 23), contrary to EG_6N_3 decorated surfaces. This is due to the more than 3 times higher diameter of PEG3000azide than EG_6N_3. Thus, varying the mol% directly affects the distance in between adjacent HA molecules without an HA-derived saturation effect. Figure 24 B illustrates the development of modelled distances (*d*) depending on the mol% of applied reactive polymers.

A

Surface coverage	N per µm²	$N_{80\%}$ per µm²	*d* [nm]
Max. coverage*	25786.80	20629.44	10.58
90 mol%	23208.12	18566.50	11.15
80 mol%	20629.44	16503.55	11.83
70 mol%	18050.76	14440.61	12.65
60 mol%	15472.08	12377.67	13.66
50 mol%	12893.40	10314.72	14.96
40 mol%	10314.72	8251.78	16.73
30 mol%	7736.04	6188.83	19.32
20 mol%	5157.36	4125.89	23.66
10 mol%	2578.68	2062.94	33.46

B

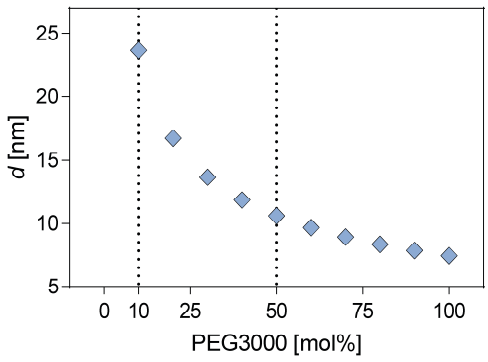

Figure 24: Estimated *d* in dependence of surface coverage. (A) Calculated number of molecules per µm2 based on their R_g and indicated mol% surface coverage of molecules bearing azide groups. N80% gives the number of reactive molecules assuming a click reaction yield of 80 %. Distance d in between molecules according to their surface coverage based on equation (4). (B) Calculated d depending on of PEG3000 mol%. Calculated values according to model derived from experimental data. *Note that "max. coverage" is defined as 35 % coverage of the surface (indicated by asterisk). Calculated d in dependence of PEG3000 mol%. Calculated values according to model derived from experimental data. Dotted lines highlight 10 and 50 %mol.*

As expected and congruent to experimental data, the higher the mol% of the azide carrying polymer the shorter is the distance between reactive azide moieties and thus the distance of surface clicked HA. The graph resembles an exponential decay curve. The maximal slope occurs within the range between 10 and 50 mol% PEG3000azide. The simulation calculates an over 2-fold increase in the inter-molecular distance from 50 to 10 mol%. That is why 50 and 10 mol% were applied for surface generation in further cell culture experiments.

As the diameter which is occupied by HA according to the experimental data (Ø 3.27 nm) does not exceed the distance in between reactive molecules, the number of molecules per µm² according to Figure 24 A directly correlates with the number of HA molecules bound to the surface. Based on these simulations it is possible to determine the number of HA molecules bound to the surface (Table 24).

Table 24: Calculated surface concentration of 5 and 10 kDa HA upon 10 and 50 mol% PEG3000azide.

Surface coverage	Distance between $PEG3000_{azide}$ molecules [nm]	HA molecules per µm²	N_{HA} [mmol]	5 kDa HA [ng/cm²]	10 kDa HA [ng/cm²]
50 mol%	14.96	10314.72	1.74	8.56	17.13
10 mol%	33.46	2062.94	0.16	1.71	3.43

Thiolated OEGs have been applied in the past to form SAMs on gold-coated QCM-D crystals. SAMs with terminal azide groups represent a powerful tool for controlled surface immobilization of HA (Minsky, Antoni and Boehm, 2016). PEGs and OEGs, utilized for SAM formation take either a brush-like conformation or a coil-like conformation depending on their polymer length. The conformation in turn correlates with its grafting density. A direct comparison of MW-depending grafting density was

drawn by Zhu *et al.* for different PEG sizes. They measured a grafting density of 92 % at a MW of around 300 Da and 35 % for MWs of 1000 or 2000 Da (Zhu *et al.*, 2001). Sauter *et al.* also determined the grafting density. In their work they applied mPEG2000-urea-triethoxysilane, which is sterically slightly less favorable than mPEG-silane and determined a grafting density of around 10 % (Sauter *et al.*, 2013). In the thesis presented here mPEG2000-silane is applied, which resembles more the approach of Sauter *et al.* However, as here no direct comparison in between different PEG polymer lengths was drawn, I used the experimentally determined grafting densities of Zhu *et al.* as basis for my modelling.

To differentiate between the mol% of applied PEG3000azide species and the concentration of immobilized HA which correlates to the number of presented azide groups, but is not necessarily identical, from here on HA50% (HA0%, HA10%, respectively) is defined as the amount of immobilized HA upon 50 mol% (0%, 10%, respectively) PEG3000azide employment.

3.2.6 Functionalization procedure does not affect passivation stability

Bi-functionalized glass surfaces mediate cell adhesion via specifically presented binding ligands only. Therefore, binding ligands were immobilized on gold nanoparticles via a thiol linker and the space between them was passivated with a mixture of PEG2000 and PEG3000azide. During the course of surface production gold-nanostructured and PEG2000/3000azide passivated glass surfaces were thus incubated with adhesive ligands. Afterwards, surfaces were washed several times to remove any non-specific bound ligand, e.g. peptides which got entangled in the PEG network. To assess the effectivity of the washing protocol, additionally glass surfaces without gold-nanoparticles were PEG2000/3000azide passivated, incubated with respective linkers and washed several times with H_2O and PBS. Finally, cell-binding repellent capacities were evaluated by a HaCaT cell adhesion experiment. As stated before, HaCaT are an epithelial cell line. Due to their epithelial character cells always form tightly connected cell sheets. The occurrence of single cells is highly atypical and would *in vivo* hint towards a neoplastic cell. Even so, the seeding density of HaCaT cells was slightly reduced for the adhesion experiment (compared to long-term cultivation) to better resolve the spreading behavior of HaCaT cells. Figure 25 depicts HaCaT cell adhesion after 3, 8 and 19 h. As no cells spread during the time of observation, passivation stability was confirmed. Additionally, these results confirm that no unspecific binding of cRGD or EPDIM takes place on PEG2000/3000azide passivated surfaces without gold-nanoparticles.

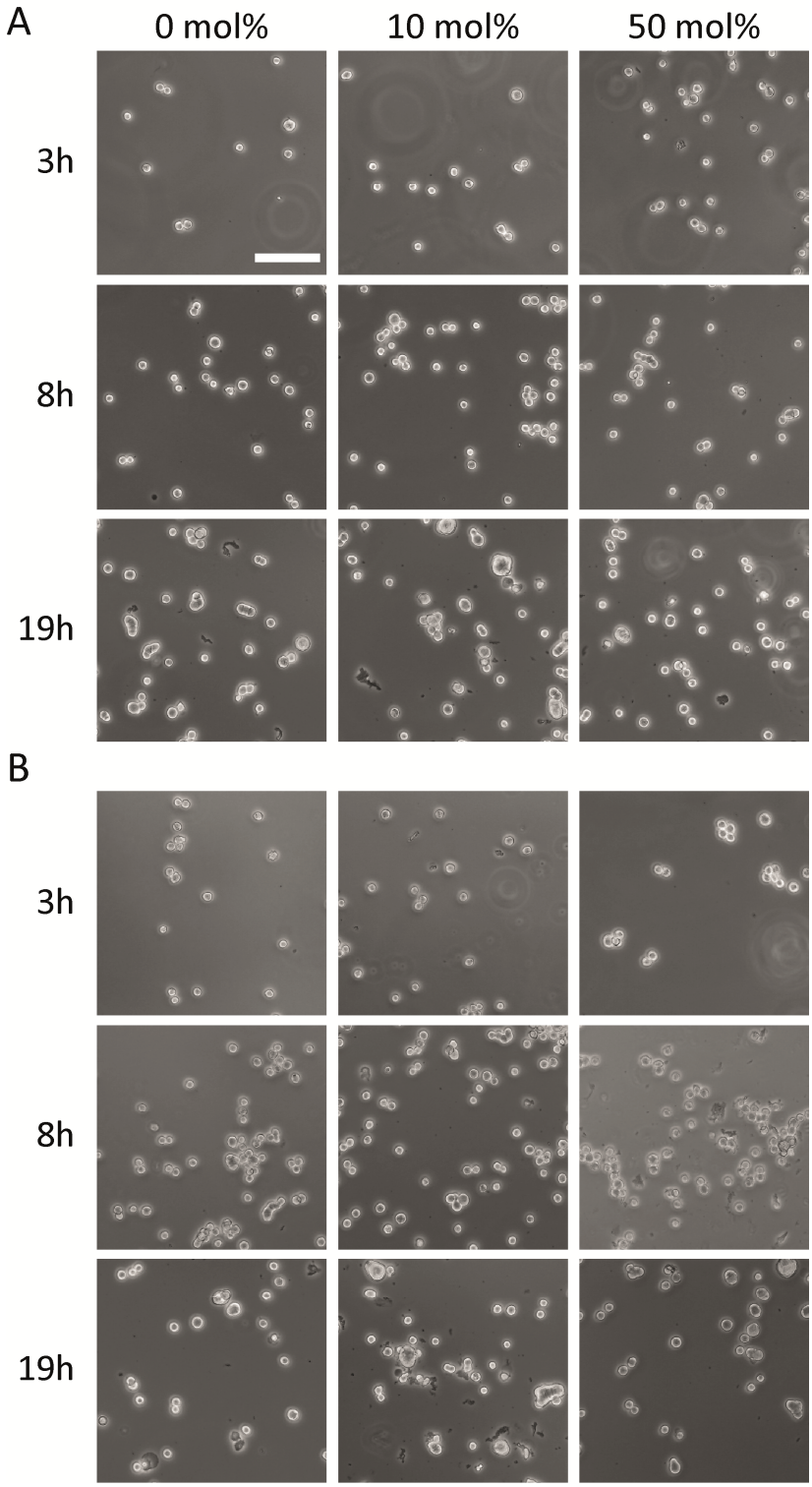

Figure 25: HaCaT cell adhesion on PEG2000/PEG3000azide passivated glass surfaces. 2.5 x 104 cells/cm2 HaCaT cells were seeded on surfaces with 0, 10 and 50 mol% PEG3000azide, incubated with (A) cRGD and (B) EPDIM and washed with H2O and PBS. Cell adhesion and spreading was observed after 3, 8 and 19 h, respectively. Scale bar: 100 µm. *For a wider surface overview please be kindly referred to Figure 47, appendix.*

3.2.7 HA presentation without adhesive ligands does not mediate HaCaT cell spreading

To determine whether HaCaT cells adhere to surfaces which only present HA, glass surfaces were passivated with a mixture of PEG2000 and PEG3000azide at different mol%, before end-alkylated 5 kDA HA was clicked on the azide moieties. HaCaT cells were seeded and cell adhesion was recorded for 19 h (Figure 26). The results proved that HA alone is not sufficient to mediate HaCaT cell spreading, however, cells seemed to attach and eventually migrate towards each other as cell aggregates increased during the recording time.

3.2.8 HaCaT cells adhere on bi-functionalized glass surfaces

Finally, bi-functionalized surfaces were evaluated for their cell adhesive properties. To test whether presentation of adhesive ligands (cRGD and EPDIM) on surfaces functionalized with HA0%, HA10% and HA50% is able to mediate cell adhesion, HaCaT cells were seeded and adhesion and subsequent spreading was monitored for a total recording time of 19 h (Figure 27). A first spreading of single cells was observed after a cultivation of 8 h. After 19 h, cells were fully spread on all surfaces, independently of surface concentration of HA or applied cell binding ligand.

All together, the presented results confirmed that bi-functionalized glass surfaces with different amounts of immobilized 5 kDa HA together with cRGD or EPDIM mediate HaCaT cell adhesion and spreading within 19 h (Figure 27). Passivated glass surfaces which were incubated with cRGD or EPDIM, but had no gold-nanoparticles did not mediate cell spreading, indicating that cRGD and EPDIM specifically bound to gold-nanoparticles (Figure 25). Passivated glass surfaces which were functionalized with HA alone without adhesive ligands had no cell-adhesive capacities (Figure 26).

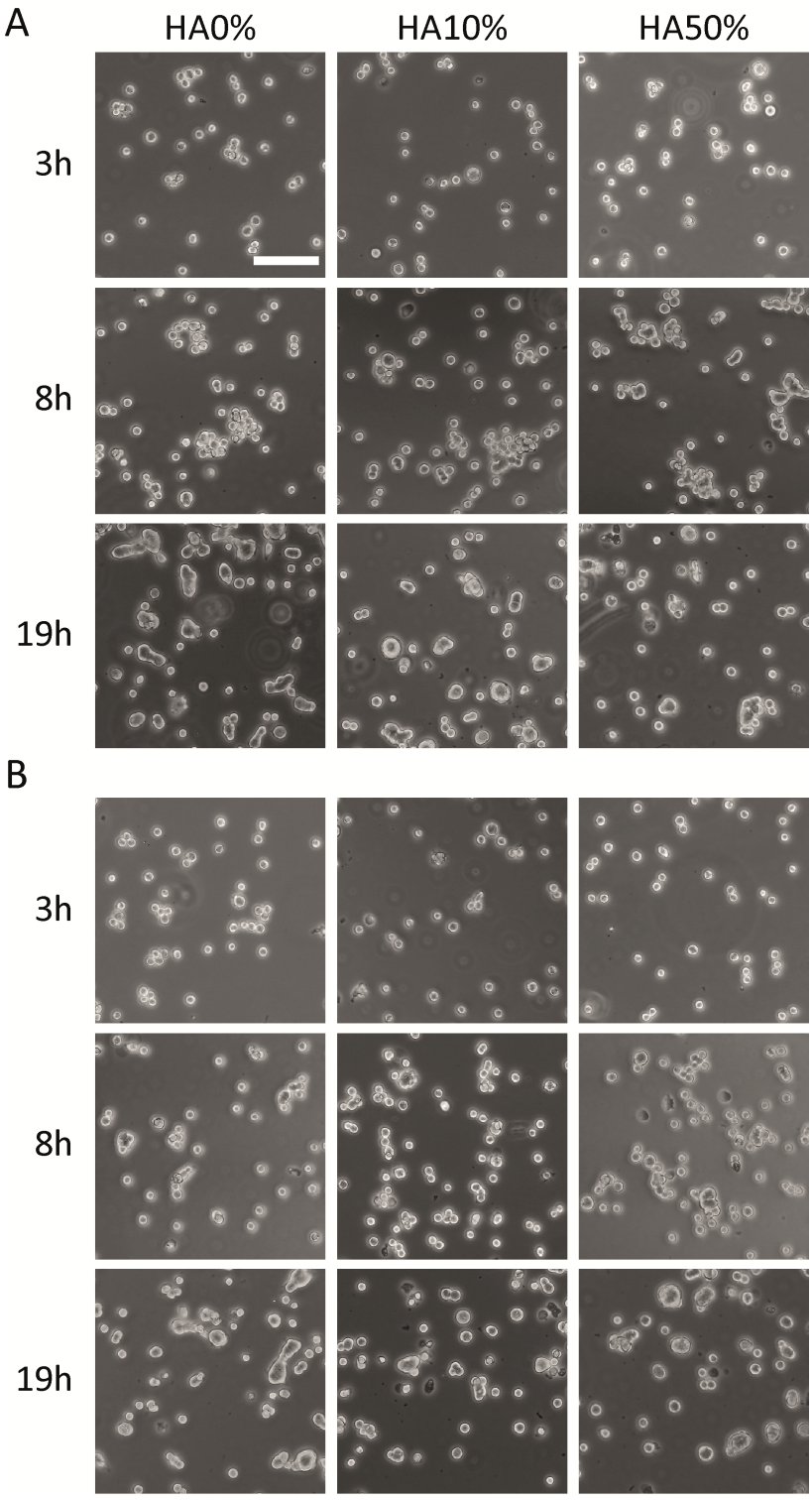

Figure 26: HaCaT cell adhesion on PEG2000/PEG3000azide passivated and HA immobilized glass surfaces. 2.5 x 104 cells/cm2 HaCaT cells were seeded on surfaces with 0, 10 and 50 mol% PEG3000azide, functionalized with 5 kDa HA, incubated with (A) cRGD and (B) EPDIM and washed with H2O and PBS. Cell adhesion and spreading was observed after 3, 8 and 19 h, respectively. Scale bar: 100 µm. Note: To differentiate between the mol% of applied PEG3000azide species and the concentration of immobilized HA, HA50% (HA0%, HA10%, respectively) is defined as the amount of immobilized HA upon 50 mol% (0%, 10%, respectively) PEG3000azide employment. *For a wider surface overview please be kindly referred to Figure 48, appendix.*

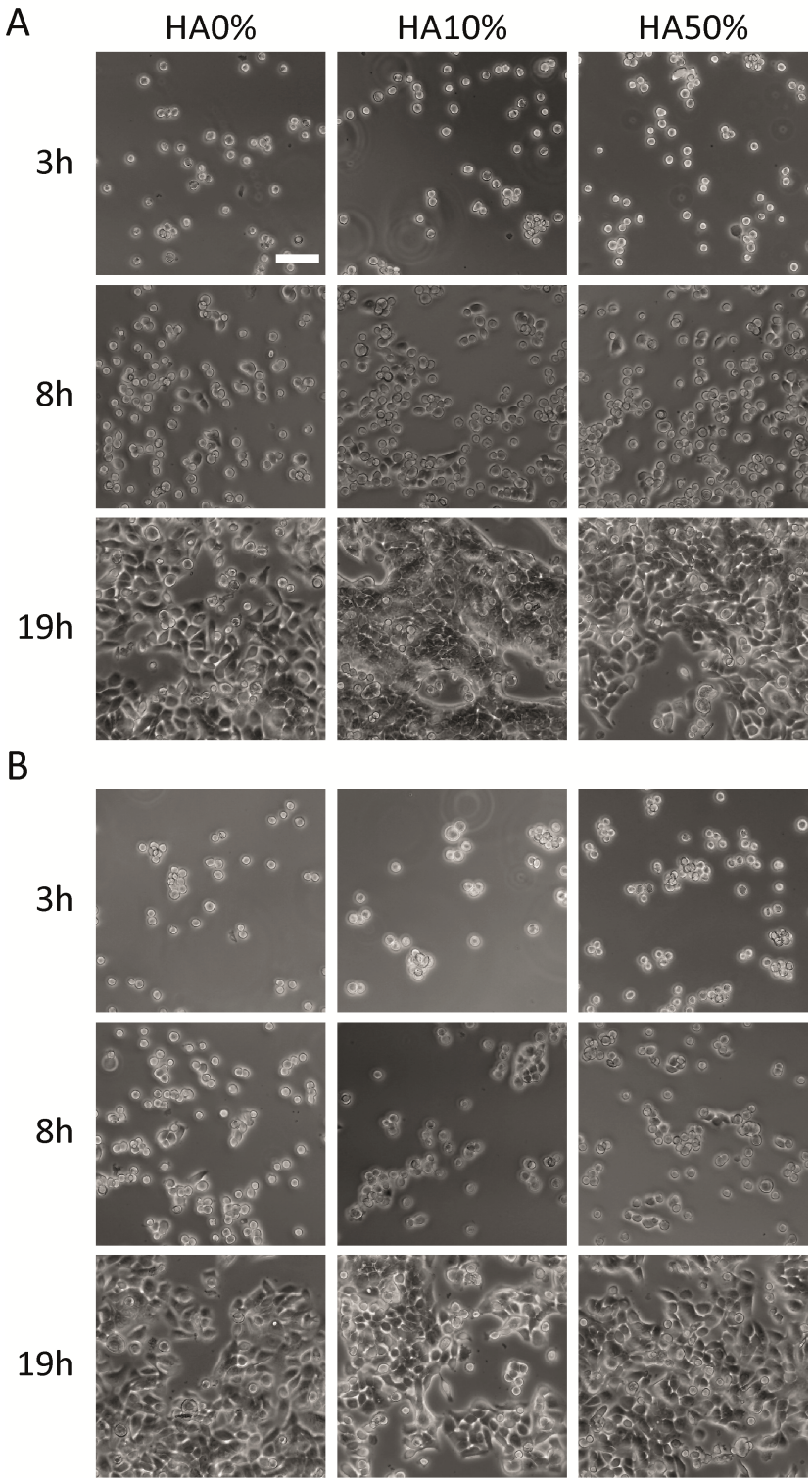

Figure 27: HaCaT cell adhesion on PEG2000/PEG3000azide passivated, HA immobilized glass surfaces and functionalized gold-nanostructured glass surfaces. 2.5 x 104 cells/cm2 HaCaT cells were seeded on surfaces with 0, 10 and 50 mol% PEG3000azide, functionalized with 5 kDa HA and (A) cRGD and (B) EPDIM Cell adhesion. Spreading was checked after 3, 8 and 19 h, respectively. Scale bar: 100 µm. *Note: To differentiate between the mol% of applied PEG3000azide species and the concentration of immobilized HA, HA50% (HA0%, HA10%, respectively) is defined as the amount of immobilized HA upon 50 mol% (0%, 10%, respectively) PEG3000azide employment. For a wider surface overview please be kindly referred to Figure 49, appendix.*

3.2.9 HA presentation on bi-functionalized glass surfaces with varying binding ligands and HA concentration affects cell-ECM interaction

CD44 is the main signal transducing HA receptor in the epidermis and involved in cell adhesion as well as cell migration. Cells interact with their environment via integrins. Integrin clustering eventually leads to formation of focal adhesions, a multi-protein complex which mediates cell adhesion to the surface. Thus, in order to examine a cellular response towards basal HA presentation cells were seeded and cultivated on bi-functionalized glass surfaces and localization of CD44 as well as vinculin, used as a marker for focal adhesions, were visualized by indirect immunofluorescence (Figure 28).

CD44 mainly localizes in between cells and at the edges of cell cluster. There, more intense signals for CD44 were observed, indicating a clustering of the HA receptor. For cRGD and EPDIM-functionalized glass surfaces no correlation between CD44 intensity and immobilized HA was observed. Vinculin revealed the formation of focal adhesions especially at the edges of the cell clusters. No co-localization between CD44 and focal adhesions occurred. Interestingly, the intensity and number of focal adhesion rose (qualitatively) with rising HA immobilization density. This was seen for both, cRGD and EPDIM functionalized glass surfaces, with a stronger effect for EPDIM functionalized surfaces (Figure 28).

In earlier studies a role of HA in surpassing mechanical information from the extracellular environment has been postulated (Chopra *et al.*, 2014). Also other studies observed an increased adhesiveness of cells upon HA administration (Tavianatou *et al.*, 2019). Chopra *et al.* also observed focal adhesion formation which corresponded with HA availability in the substrate (Chopra *et al.*, 2014). The more HA was presented the larger focal adhesions were formed. This is in accordance with my observations. Future quantitative analysis of number and extent of focal adhesions in my system will shed light on HA's role on focal adhesion formation and how HA contributes to focal-adhesion dependent cell adhesion. As CD44 and vinculin did not co-localize in my experiments it will be interesting whether HA's effect on focal adhesion formation is CD44-mediated or not.

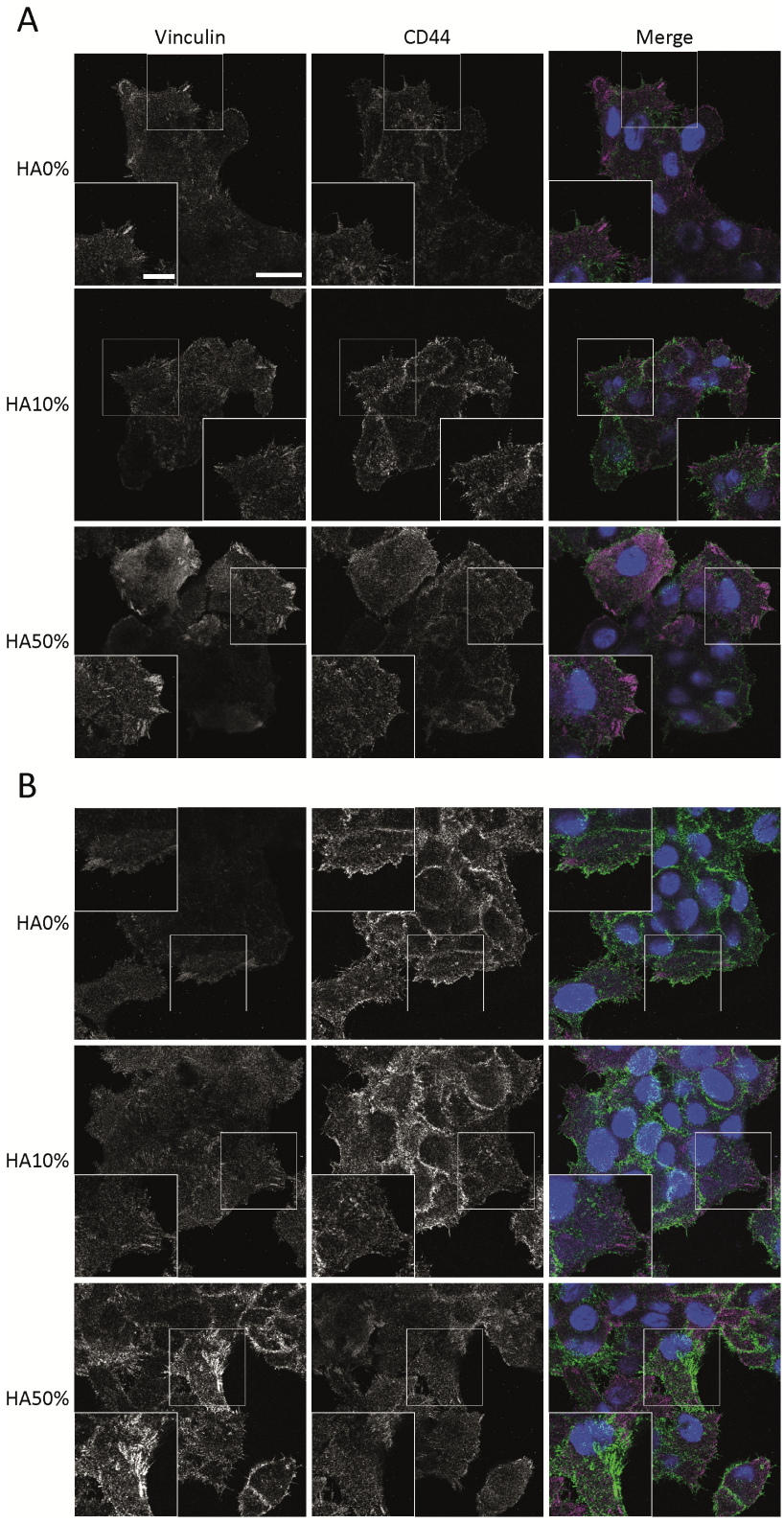

Figure 28: Confocal fluorescence images of HaCaT cells on PEG2000/PEG3000azide passivated, HA immobilized and cRGD/EPDIM functionalized gold-nanostructured glass surfaces. Confocal fluorescence images of basal side of HaCaT cells cultivated on surfaces with 0, 10 and 50 mol% PEG3000azide, covalently immobilized with 5 kDa HA and functionalized with (A) cRGD and (B) EPDIM stained for CD44 (green), vinculin (magenta) by indirect immunofluorescence. Nuclei were visualized by DAPI staining (blue). 63x oil objective lense. Scale bar: 20 µm; Scale bar insert: 20 µm *Note: To differentiate between the mol% of applied PEG3000azide species and the concentration of immobilized HA, HA50% (HA0%, HA10%, respectively) is defined as the amount of immobilized HA upon 50 mol% (0%, 10%, respectively) PEG3000azide employment.*

The aim of the development of bi-functionalized glass surfaces was to produce highly defined and controlled ECM mimicking substrates of reduced complexity where HA and an integrin-addressing binding ligand are orthogonally presented. The adhesive properties of functionalized gold-nanostructured glass surfaces and their effect on cell spreading as well as intracellular integrin clustering have been reported thoroughly in the past (e.g. (Arnold *et al.*, 2004; Cavalcanti-Adam *et al.*, 2007). A new dimension in ECM mimicking substrates was introduced by the possibility to dual-functionalize surfaces via click reaction. Such surfaces have been optimized to co-present adhesive ligands with a synergistic peptide to demonstrate improved cell adhesion (Schenk *et al.*, 2014) or to orthogonally present full proteins such as the growth factor bone morphogenic protein 2 (BMP-2) (Posa *et al.*, 2019). Here, I generated bi-functionalized glass surfaces where adhesive ligands were bound to gold-nanoparticles and the polysaccharide HA on the other hand was immobilized via click chemistry (contrary to Minsky, Antoni and Boehm, 2016). For developmental reasons I used 5 kDa HA in varying concentrations with two different binding ligands, EPDIM and cRGD at a constant gold-nanoparticle spacing of 52 ± 9 nm. Depending on the chosen binding ligands, different time points during wound healing can be addressed as well as the level of severeness of the wound: binding motifs of fibronectin (cRGD) would represent a wound affecting both dermis as well as epidermis whereas binding motifs of laminin 332 (EPDIM) would account for a wound only affecting the skin's epidermis or a more progressed wound healing respectively. Moreover, the here introduced bi-functionalized glass surfaces hold the advantage to fine-tune several additional parameters according to the underlying research question:

(1) particle distance of binding motif
(2) nature of binding motif
(3) spacing and concentration of basally presented HA
(4) alkylation side of HA: end- or side-alkylated
(5) MW of HA
(6) simulate a large HA polymer with LMW HA by applying a very low spacing

3.3 Part III: How to Mimic Dynamical Changes in ECM Composition during Re-epithelialization

Re-epithelialization is not a static but a highly dynamic process. Upon wounding and throughout the whole wound healing process the ECM in the wound site is strongly remodeled, mostly by dermal fibroblasts. Thus, keratinocytes are recurrently forced to adapt their integrin expression to the new ECM environment in order to close the wound. With the aim to simulate those dynamics I integrated the bi-functionalized glass surfaces into an ECM wound model system where cells are primed in a first stage towards a highly defined ECM environment ("ECM 1") before they face a second stage ECM environment ("ECM 2") of an artificial wound site which can be systemically modulated (Figure 29 A).

In order to realize such a two-stage ECM wound model, cell culture inserts with microporous membranes were used as a support for HaCaT monolayers. A wide range of microporous membranes differing in their material as well as pore size are commercially available. In a first step appropriate microporous membranes needed to be identified and their even coating with ECM molecules ("ECM1") of interest needed to be ensured. Next, the coated membranes must not interfere with the physiological appearance of utilized cell lines. In case of epidermal keratinocytes, the formation of a confluent monolayer resembling a functional epithelium should be enabled. In order to work as a wound healing model, it is important that keratinocyte migration is initiated upon wounding of the monolayer and that their collective migration character is kept. After introducing a wound site by simply cutting the membranes they were placed and fixed on desired surfaces with varying complexity. For instance, collagen I gels or surfaces coated with full length proteins would resemble more the *in vivo* situation, whereas by using (bi-) functionalized gold nanostructured glass surfaces it is possible to present a highly defined and controlled ECM environment where single integrin families can be specifically addressed (Figure 29 B). Hence, it would be possible to specifically unravel the combined effect of HA together with integrin binding families on processes occurring during re-epithelialization.

By using membranes as a support for keratinocyte monolayers, keratinocytes on the membrane could face a different ECM environment than the ones in the wound site as they were fabricated separately from the artificial ECM environment. Additionally, and in contrast to scratch assays surfaces comprising a highly defined artificial ECM environment ("ECM 2") are not mechanically impaired as the wounding procedure was not performed on the substrate but in a separated step before the assembly of the cell-cultivated membrane and surface. Altogether, this ensures a clean, highly defined and well-controllable ECM environment.

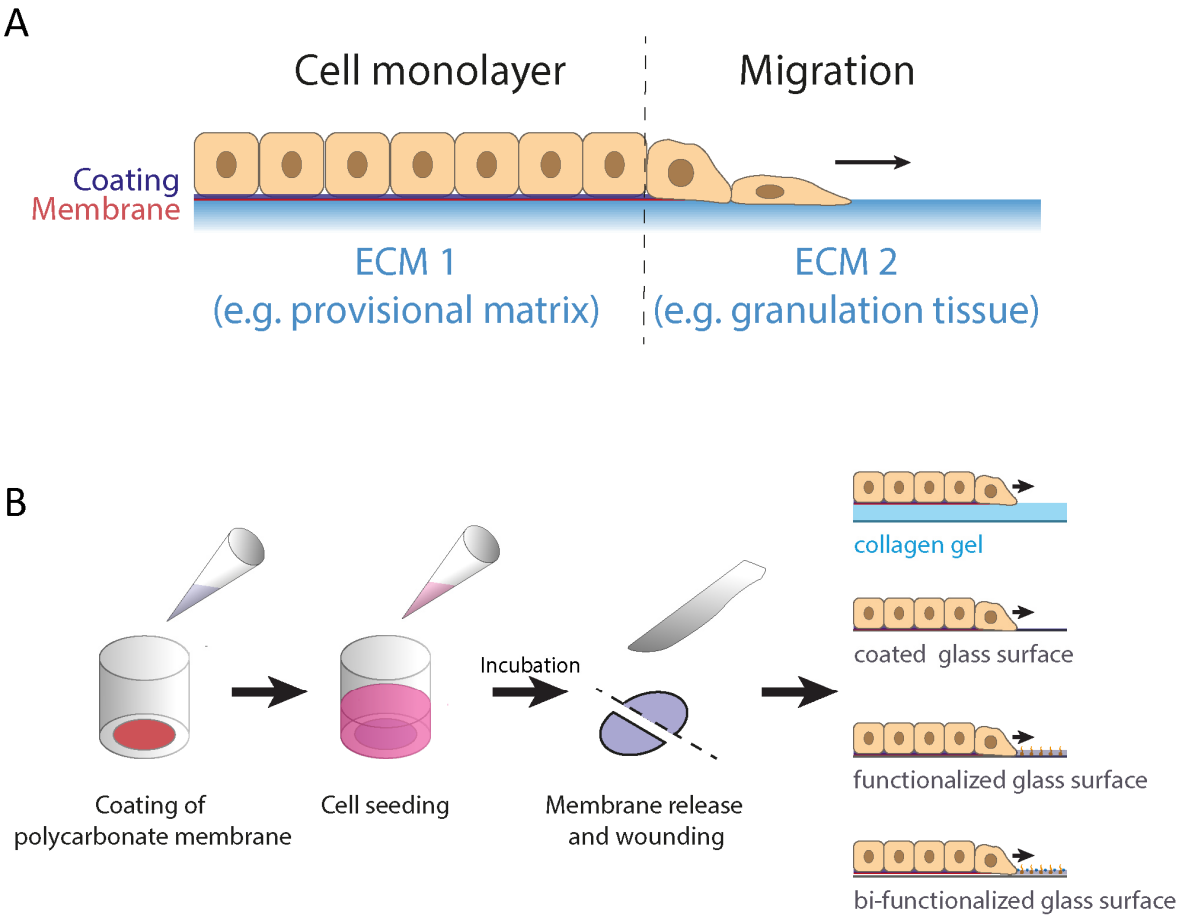

Figure 29: Schematic illustration of a two-stage ECM wound model. (A) The membrane coating features a first ECM environment, e.g. the intact wound-adjacent epidermis or the wound site, which is already invaded by keratinocytes at an early stage of re-epithelialization (ECM 1). Upon membrane transfer cells face a second substrate providing a second ECM environment (ECM 2). This substrate for instance mimics ECM proteins of interest emerging in the provisional matrix or in the granulation tissue as re-epithelialization proceeds. (B) Polycarbonate membranes in cell culture inserts are coated with ECM molecules of interest. Next, cells are seeded and cultivated until a confluent monolayer is formed. After, membranes are released from cell culture inserts and a wound is introduced by cutting the membrane. The membrane works as a support matrix for an epidermal full confluent monolayer, which can be placed on matrix gels, coated surfaces as well as surfaces with a highly defined one- (functionalized glass surface) or two-component (immobilized HA together with adhesive ligand) ECM environment

3.3.1 Collagen I coating improves HaCaT cell adhesion on polycarbonate membranes

Table 27 (Appendix) gives an overview of different, commercially available microporous membrane systems for cell culture application focusing on a pore size of 0.4 µm. Due to their stiffer material properties, which make handling easier polycarbonate membranes with a diameter of 7.7 mm were chosen (if not otherwise stated “membrane” always refers to polycarbonate membranes). For the establishment of the two-stage ECM wound model, I decided to use collagen I as a priming ECM molecule for HaCaT cells. Collagen I is widely used for keratinocyte culturing and has been reported to mediate adhesion and subsequent spreading of human epidermal keratinocytes (Ponce *et al.*, 2017). HaCaT cells were seeded on collagen I-coated or non-coated polycarbonate membranes with a pore size of 0.4 µm. After 24 h of cultivation in complete medium the phenotype of HaCaT cells was analyzed

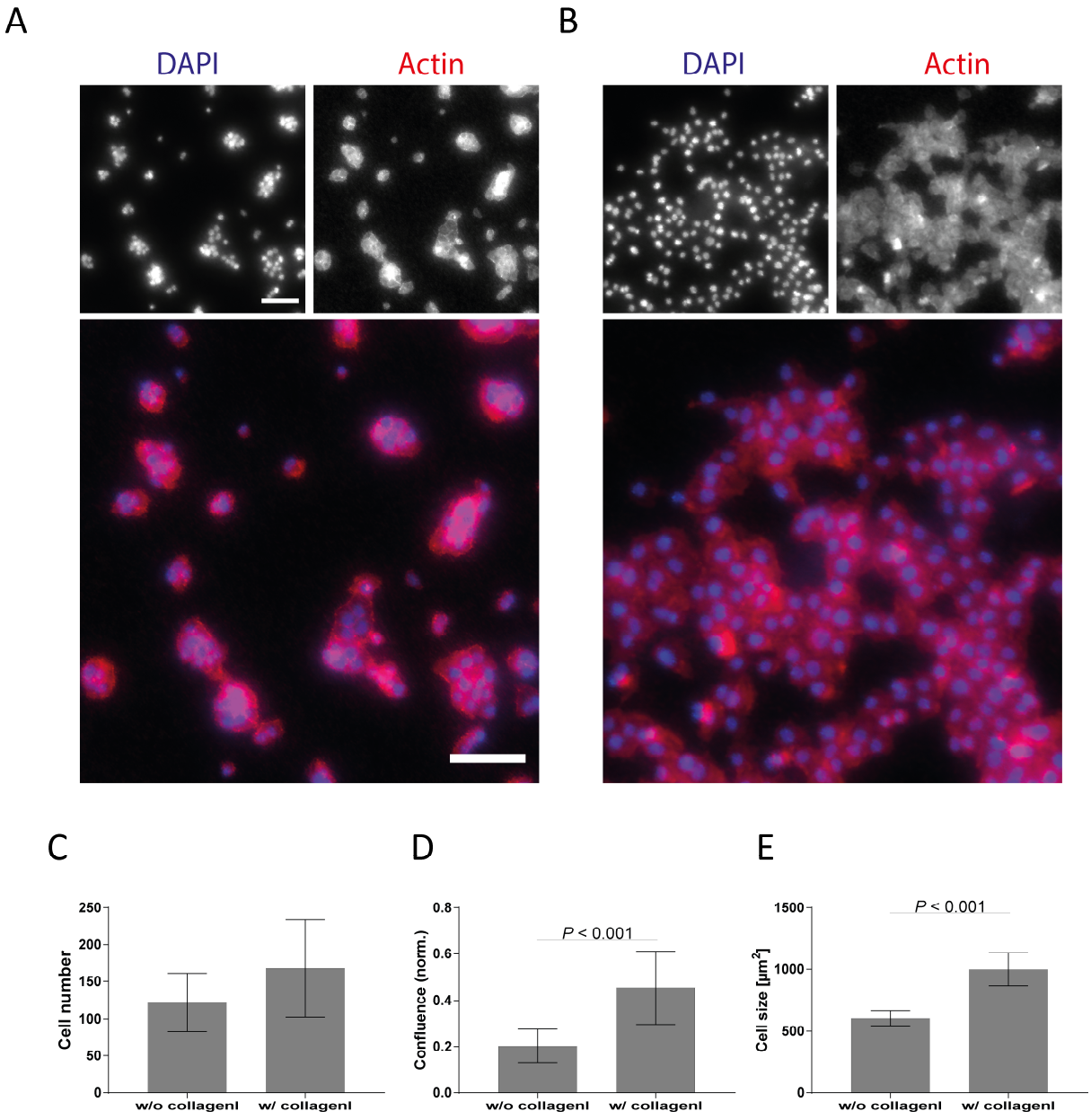

Figure 30: Collagen I coating improves HaCaT cell adhesion on polycarbonate membranes. HaCaT cells were seeded (1.88 x 104) on (A) non-collagen I-coated or (B) coated polycarbonate membranes and cultivated for. Nuclei were visualized with DAPI (blue) and actin by TRITC-phalloidin (red). (C) Cell area was determined using the actin signal, the number of cells by counting the DAPI stained nuclei. (D) The confluence was determined by dividing the total cell area by the image area. (E) The mean cell size was determined by dividing the total cell area by the total number of nuclei counted. The data represents mean ± SD of a recorded total area of 3024 x 3024 µm. Mann-Whitney U test showed that the confluence (D) and cell size (E) significantly differed in dependence on the collagen I coating. Scale bar: 100 µm. *Note: cryptic lamellipodia are not taken into account for determination of the cell area. Thus, the cell area is rather seen as an approximation than an absolute value.*

using immunofluorescence. As the polycarbonate membrane itself is light-impermeable, cell nuclei were stained with DAPI to determine the cell number. For cell shape analysis the cytoskeleton was visualized using TRITC-labelled phalloidin (Figure 30 A, B). I found that HaCaT cells on non-coated polycarbonate membranes adhered on the substrate. Cells formed multilayered cell clusters, as visualized by the DAPI staining. This indicates only poor cell spreading (Figure 30 A). However, providing collagen I-coated substrates increased both, cell adhesion and cell spreading (Figure 30 B).

This observation was confirmed by determining the mean cell number on both surfaces. After 24 h of cultivation 122 ± 39 cells per region of interest were counted on non-coated and 168 ± 65 cells per region of interest on collagen I-coated substrates even though initial cell seeding density had been identical (18.8 x 10^3 cells/membrane) (Figure 30 C). In accordance with this observation the confluence for cells analyzed on collagen I-coated surfaces was significantly higher compared to cells on non-coated surfaces (Figure 30 D). Calculating the mean cell size reveals a significantly higher cell size of 999.09 ± 134.80 µm^2 for cells facing a coated substrate than on non-coated substrates (606.20 ± 60.99 µm^2), indicating a better spreading of HaCaT cells upon provision of collagen I coating (Figure 30 E).

To sum up, the applied polycarbonate membrane is a good substrate to present ECM proteins to HaCaT cells, mediating both cell adhesion as well as spreading.

3.3.2 HaCaT cells form confluent monolayers on microporous membranes

To identify the initial cell seeding number necessary to reach a confluent cell monolayer within a defined period of time, HaCaT cells were seeded at different cell numbers in collagen I-coated cell culture inserts before being cultivated. In order to resolve cells cultivated on the light-impermeable polycarbonate membranes, HaCaT cell viability and density was determined using a live-dead staining after 24, 48 and 72 h, respectively. The staining revealed cell clusters as well as formation of confluent epithelial monolayers, depending on the initial seeding density as well as the cultivation time (Figure 31). Confluent viable monolayers were formed upon an initial seeding number of 1 x 10^5 cells per cm^2 within 48 h and 3 x 10^5 cells per cm^2 within 24 h (Figure 31 and Figure 50, appendix).

In order to keep the contribution of keratinocyte-derived ECM molecules as little as possible the duration of cultivation was kept at a minimum. Therefore, cells were cultivated for 24 h with an initial seeding number of 3 x 10^5 cells per membrane in further proceedings.

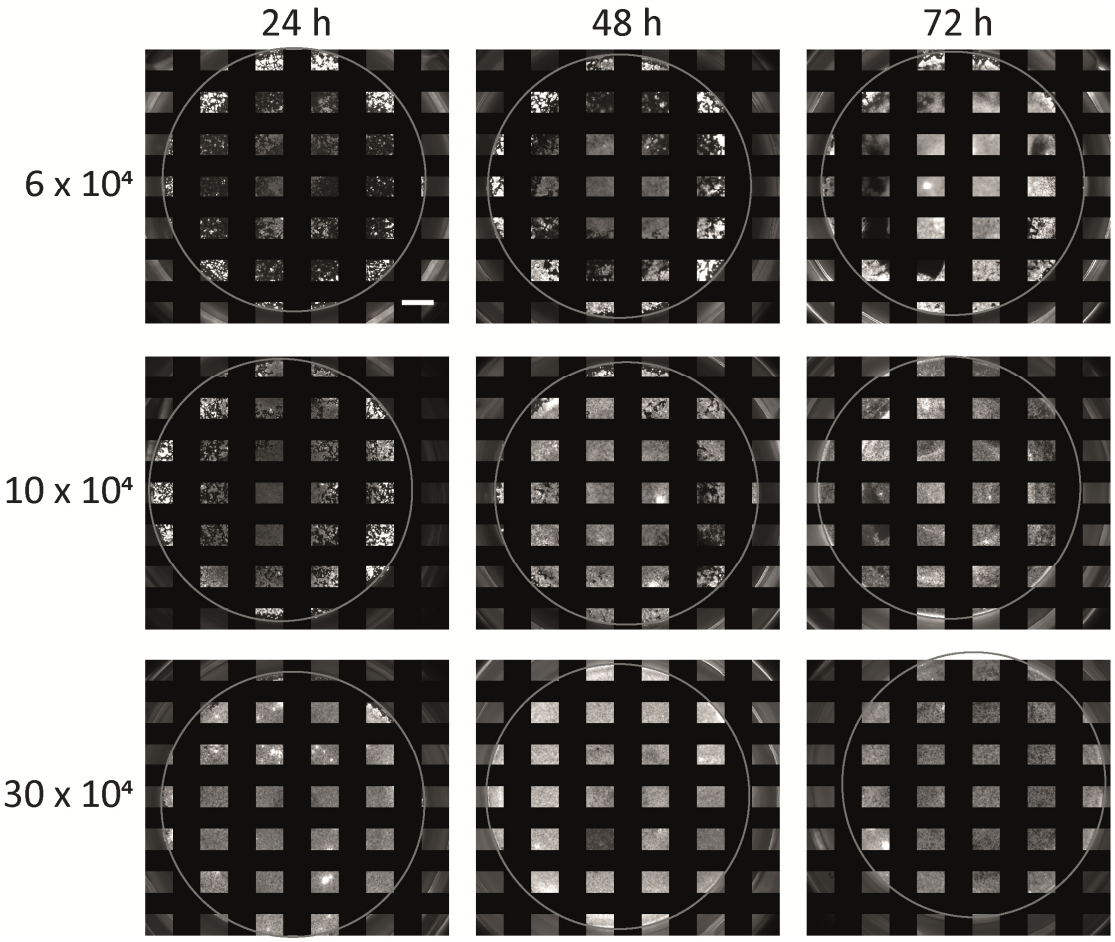

Figure 31: Membrane cell coverage upon seeding different numbers of HaCaT cells and cultivation for 24/48/72 h. Membranes were collagen I-coated and initial HaCaT cell seeding number per membrane was 6 x 104, 105 and 3 x 105, respectively. Living cells were visualized by calcein-AM to determine membrane cultivation after 24, 48 and 72 h in DMEM supplemented with 10 % (v/v) FBS. Full membrane area was recorded at 10x magnification with a tiles shift of 100%. Membrane boundaries are indicated in grey. Representative images of 2 replicates. Scale bar: 1000 µm.

3.3.3 Membrane-cultivated HaCaT cells migrate upon wounding

To test whether migration of membrane-cultivated keratinocytes can be induced upon wounding the cell-bearing membranes were cut (Figure 29). Therefore, the HaCaT cultivated membranes were released from their cell culture inserts. For this, different approaches, using a scalper or a puncher, were pursued. In the end the application of 8 mm biopsy punches was advantageous to scalpels as for the latter the risk of membrane rupture or unfolding was explicitly higher. Upon release, membranes were placed on clean and smooth surfaces and draining of cells was prevented by wetting the monolayer carrying membrane with cell culture medium. A wound site was attained by cutting the monolayer carrying membrane with a scalper into two equal halves. To examine migration capabilities of wounded monolayers generated in this way, the cut membranes were placed on different surfaces of interest. For reasons of proving the concept the ECM environment was kept constant: as the membranes initially were coated with collagen I, the new substrate also presented collagen I. Even though the binding ligand was kept constant, mechanical variances from ECM 1 (membrane) to ECM 2 (glass) could not be

excluded. Therefore, two substrates with different mechanical properties were provided: collagen I -coated glass surfaces and surfaces with collagen I gels. Fluorescence imaging of 2D epidermal models cultivated for four days on collagen I gels and on collagen I-coated glass surfaces, respectively revealed HaCaT migration into the open space in front of the cut and thus the "wound" site (Figure 32). HaCaT cells which migrated on collagen I gels showed a cell-free area within the migrated monolayer, as well as cell clusters which were completely isolated from the monolayer. This indicates that the monolayer did not collectively migrate but showed a more single-cell migration character. In contrast, HaCaT-covered membranes placed on collagen I-coated surfaces mediated collective migration with no cell-free areas within the collective, indicating that cell-cell contacts were not interrupted during the migration process. Additionally, even the formation of leader cells at the front edge, characterized by their large lamellipodia, could be observed.

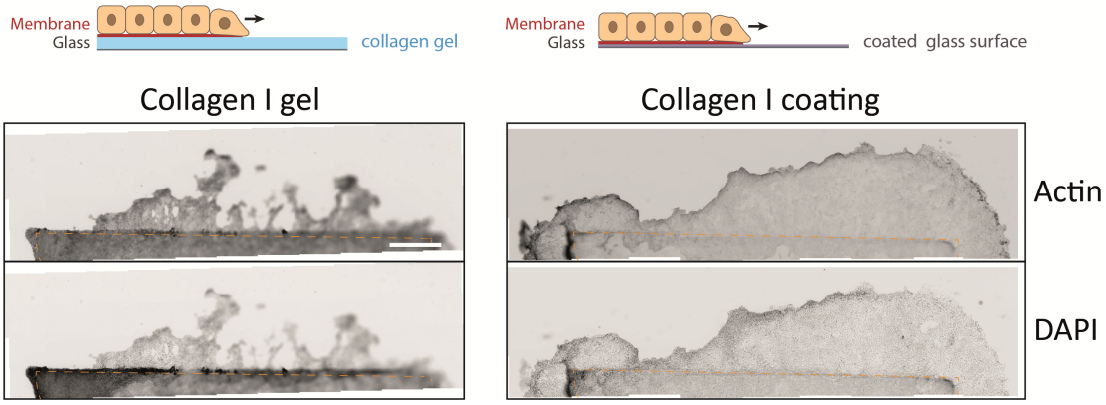

Figure 32: HaCaT migrate from a polycarbonate membrane on collagen I presenting substrates. 2D epidermal models were cut in the middle and placed on collagen I gels and collagen I -coated surfaces. After 4 days cells were PFA-fixed and nuclei were visualized with DAPI and actin by TRITC-phalloidin. Top view on membranes; dotted line indicates membrane border. Scale bar: 1000 µm

Taken together, this shows that HaCaT cell migration can be induced upon cutting of HaCaT-cultivated membranes and that the migration behavior depends on the underlying substrate. With this, a 2D epidermal model has been successfully established.

3.3.4 Collagen I glue masks ECM molecules presented in the wound site

Wounded membrane-cultivated keratinocyte monolayers need to be tightly linked to the top of respective surfaces. A motion between the membrane and the underlying substrate, even if only minor, would perturb migration processes of keratinocytes from the membrane "down" the substrate. Unpolymerized collagen I ("collagen I glue") has been reported to properly fixate human epidermal full thickness skin cultures *in vitro* (Safferling *et al.*, 2013). Upon polymerization of the glue the cell-cultured membranes are tightly linked to the surface. Hence, in Figure 32 collagen I glue was used to fixate own cell-cultured membranes on top of surfaces. To investigate the localization of collagen I glue,

non-coated and non-cultivated polycarbonate membranes were cut in halves and were fixated with collagen I glue on top of APTES-activated glass dishes (Material and Methods, 1.4.1). Different gluing patterns with varying parameters were applied, such as the number of collagen I drops, volume and membrane placing on top of these drops or pushing of the membrane into pre-placed glue drops. Figure 33 shows the location of collagen I glue after its polymerization on the surface via indirect immunostaining. Collagen I occurs in front of the cut site for all tested strategies with a slightly lower risk of surface coverage if membranes are pushed into collagen I drops (Figure 33). This showed that due to the glue's low viscosity the risk cannot be excluded that parts of collagen glue unintentionally end up in the wound site and thus mask ECM molecules presented there. Since collagen I is only visualized upon immunostaining membrane and not while placing the membrane or during the migration process itself, effects of collagen I on the cellular behavior could also not be excluded.

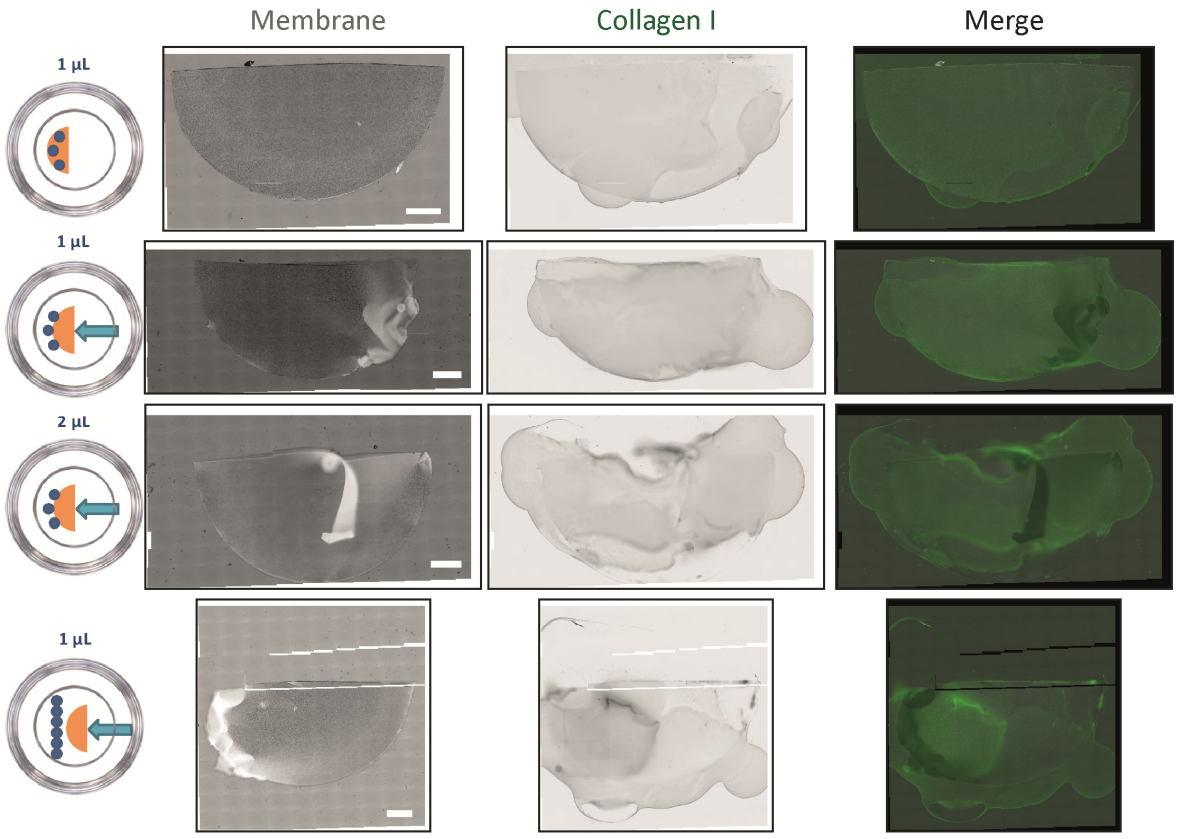

Figure 33: Collagen I glue localizes in wound site. Indirect immunostaining of polymerized collagen I glue under cut membranes. Membrane halves were fixated on activated glass surfaces using unpolymerized collagen I ("collagen I glue"). For this, drops of collagen I glue of indicated volumes were placed in different patterns on surfaces before membranes are placed directly on top of the drops or pushed into the drops (indicated by arrow). Upon collagen I polymerization collagen I (green) localization under and around the membranes (grey) is visualized by indirect immunostaining. Scale bar: 1000 µm.

To sum up, collagen I glue is a well-working and straight-forward strategy to immobilize HaCaT cultivated membranes on collagen I derived substrates and has been used as such to properly fixate human epidermal full thickness *in vitro* skin cultures (Safferling *et al.*, 2013 and own experiments, not shown). However, applying collagen I glue holds the risk that adhesive ligands bound to the surface are

covered and thus the presentation of only one single binding ligand (if it was not collagen I) is not possible. Additionally, in cases where binding ligands are presented on glass substrates the glue as a viscoelastic substrate would add another level of complexity. Therefore, in order to set up a two-stage ECM model with a highly-defined and well-controllable ECM environment, the use of collagen I glue is not appropriate.

3.3.5 Mechanical fixation conserves a controllable ECM environment

As the intention was to set up a two-stage ECM wound model with functionalized glass surfaces presenting only specific adhesive ligands, it was crucial that the "wound site" and its binding motifs, respectively are kept free of collagen I glue. Hence, different strategies were developed to mechanically fix the epidermal models on the surface using customized molds. Those molds were either polydimethylsiloxane (PDMS)- or teflon-based (Figure 34). The idea behind was to design customized molds which tightly fit in cell culture dishes and are placed on top of the cut membrane. By the tight fitting of the mold in the cell culture dish the membrane should be kept at the bottom-side.

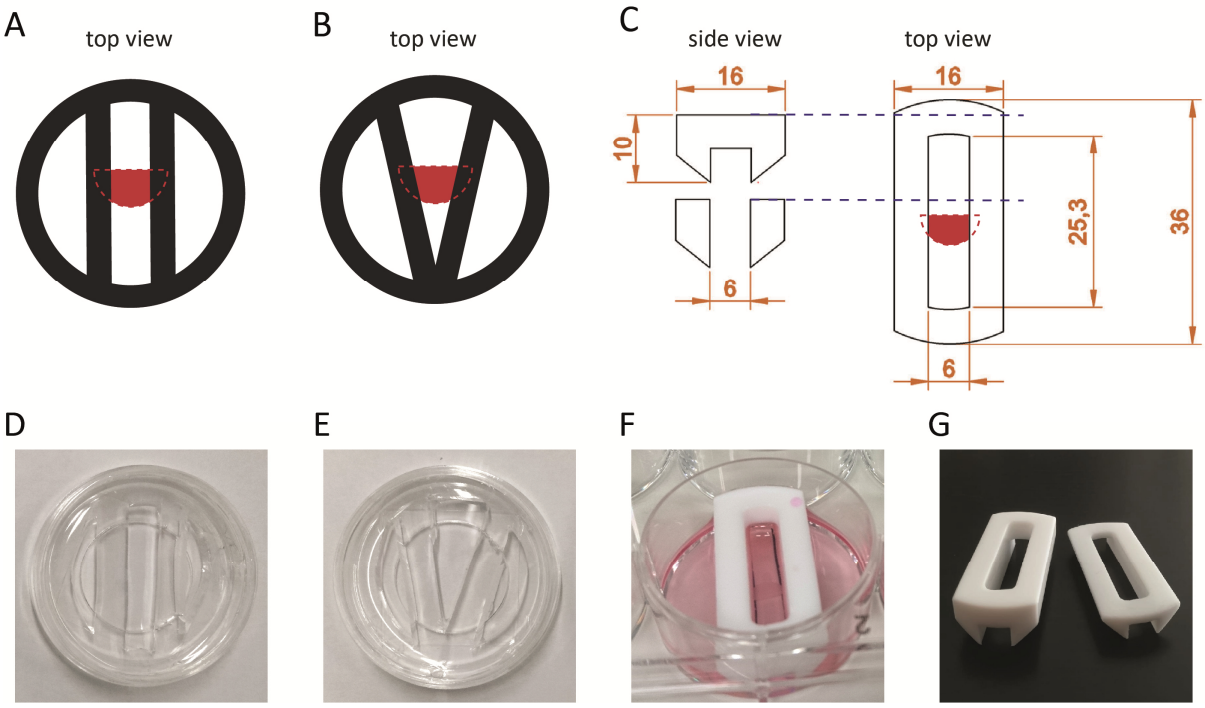

Figure 34: PDMS and teflon-based molds to immobilize 2D epidermal models on cell culture dishes. (A), (B) Top view on schemes of two different PDMS mold shapes; (D), (E) corresponding pictures. (C) Technical drawing of teflon mold (first generation), dimensions in mm; (F) picture of teflon mold. Teflon molds of (G) first (left) and second (right) generation in direct comparison. Semicircle and dotted line in red indicate membrane and sites where the membrane is clamped.

First, PDMS molds were deployed in order to mechanically fasten membranes carrying wounded HaCaT monolayers on glass surfaces (Figure 34 A, B, D, E). To fabricate such PDMS molds, PDMS was first poured into respective cell culture dishes, cut manually in the desired shape and disinfected

using 70 % EtOH. HaCaT monolayers carrying membranes were placed on surfaces and the customized, in the cell culture dishes tightly fitting PDMS molds were placed on top to press down the membrane to the surface. It was expected that cells directly under the PDMS molds received a continuous mechanical pressure which might affect their signaling towards adjacent cells. This in turn might affect cellular behavior due to the permanent pressure from the top-side and potential forwarding of such signaling throughout the confluent epidermal monolayer may occur. In order to avoid this scenario, penetrated cells should be mechanically killed to prevent any prolonged signal transmission. Within this approach it was accepted that burst cells potentially release some signaling factors as this even resemble the natural wounding process- Moreover, this signaling is temporally limited, in contrary to the alternative approach in which cells are exposed to a continuous pressure. In a first attempt I used the PDMS molds on top of cut HaCaT monolayer carrying membranes. HaCaT monolayers were placed either on collagen I gels or on collagen I -coated glass surfaces. Subsequently, a force of 9.8 N (based on the weight of a filled 1 L shot bottle and the gravity of 9.81 ms-2) was applied for 1 and 5 min, respectively. The tight connection between the membrane and the cell culture bottom was proven by successful migration of membrane-seeded cells in the area in front of the cut side after 24 h (Figure 35).

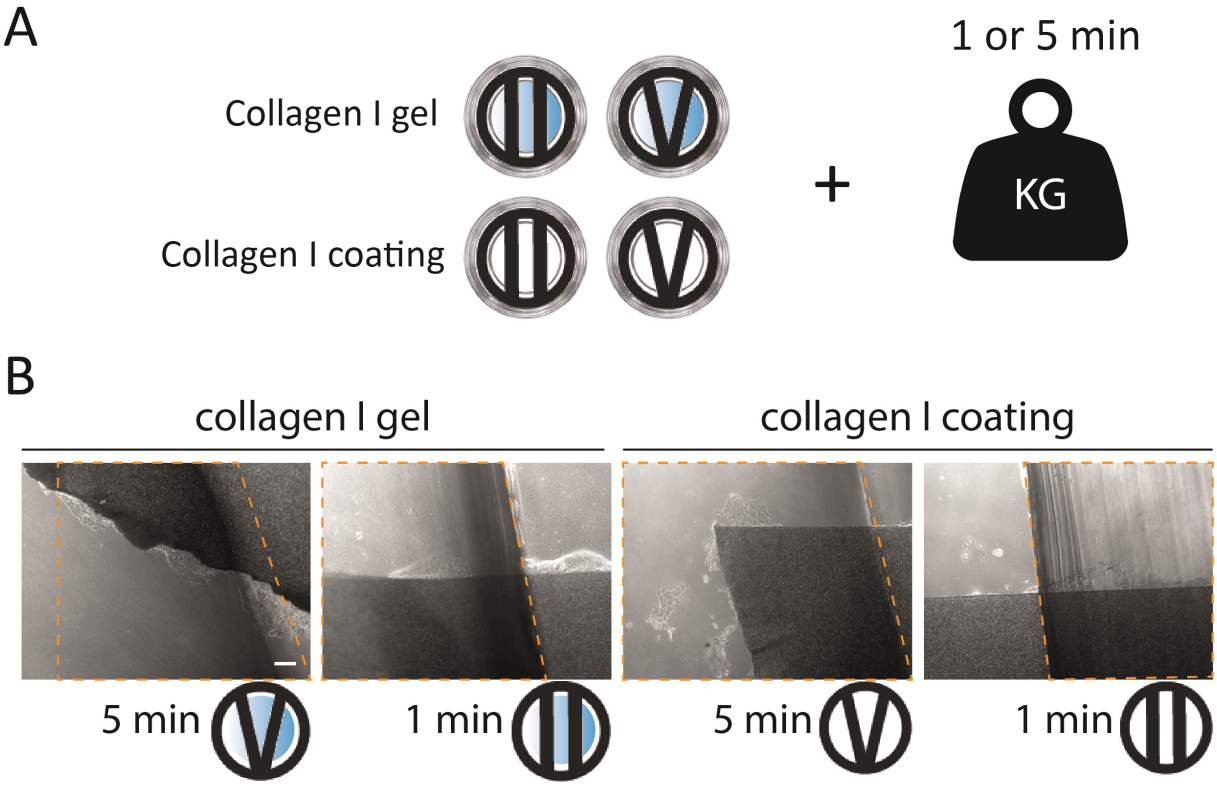

Figure 35: HaCaT cultivated membranes fixed with two differently designed PDMS molds. (A) Experimental set-up: In order to destroy cells lying under the mold a weight of 1 kg was applied for 1 and 5 min respectively. (B) Phase contrast image of PDMS-mold on top of membrane. The dotted orange line highlights the area covered by the PDMS-mold. Dark grey shades: HaCaT-monolayer carrying membrane. Scale bar: 100 µm. *Note that cells grew and migrated in the open space as well as in PDMS covered areas.*

However, cells migrated at all sides of the membrane in the open space, even under the PDMS mold. This observation revealed that the described strategy is not sufficient to kill cells under the PDMS mold. As pressure is defined as force per area one possible reason might be that due to the design of the molds and its rather large contact area the mold distributes the force over a large area leading to a local pressure that is too low to burst underlying cells. Additionally, it cannot be excluded that besides the pressure perception, cells directly under the PDMS mold would face a limited diffusion area. This in turn might lead to acidification of the surrounding medium, the diffusion area and eventually to an uncontrolled damaging of those cells.

To circumvent force absorbance by the elasticity of the material (as it might happen for PDMS) teflon was the chosen material for a second mold design. To maximize the pressure emerging from the applied force, the mold plane sitting on the cell monolayer was kept as small as possible (Figure 34 C, F, G mechanical fixation strategies).

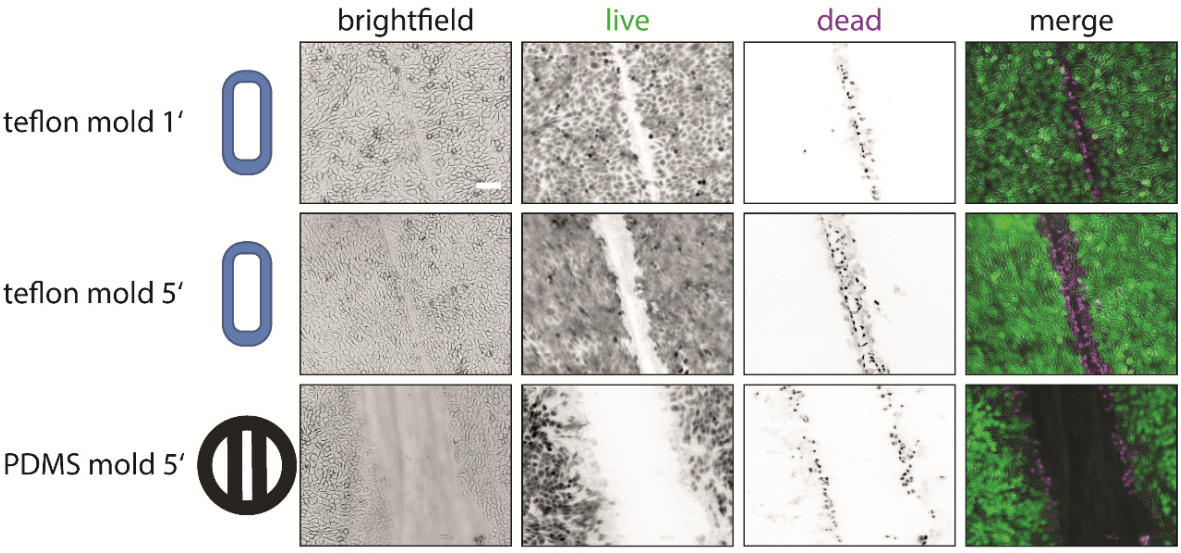

Figure 36: Weighed down teflon-molds kill HaCaT cells at contact side. HaCaT cells were grown in a 6-Well plate in full medium for 48 h until reaching full confluence before teflon- as well as PDMS-based molds were place on top. Molds were weighed down with 9.8 N for 1 and 5 min respectively. Live-dead staining reveals viability of cells at contact side with molds. Note that PDMS rips off underlying monolayer (instead of destroying cells). Living cells: green, dead cells: purple. Scale bar: 100 µm.

In order to test whether cells at the contact area with the teflon mold are mechanically destroyed, HaCaT cells were seeded in 6-well plates and grown until confluence. Teflon molds were placed on top of cell monolayers and weighed down with 9.8 N for 1 and 5 min respectively. Directly after, cell viability at the contact sides was determined. For the samples treated with the teflon mold, a clear line of dead cells at the contact side of the teflon mold within a viable cell monolayer was observed (Figure 36). This observation was made independently of the duration of force application, with the 5 min sample having a slightly broader “line” of dead cells. Remarkably, dead cells still adhered to the surface.

This is not the case for the samples having faced the PDMS mold which were ripped off the surface of the cell culture plastic (Figure 36).

In the next step I wanted to elucidate whether this locally highly controllable destroying of cells is also possible on surfaces where membranes carrying HaCaT monolayers are used instead of confluent plastic cell culture dishes. Again, membranes were placed inside cell culture dishes with the teflon mold on top and treated as described above. Figure 37 depicts a tile-scan over the whole membranes. In contrast to the results obtained with the PDMS molds, here clear lines of dead cells were observed at both membrane sides where the teflon mold kept the membrane fixated on the bottom side of the dish. Interestingly, a weight administration of 5 min was already sufficient to fully lyse cells at the bottom-side of the teflon mold.

Taken together, I developed a mechanical fixation strategy for HaCaT-carrying membranes. By this, no collagen I glue is needed for fixation of membranes. This strategy in combination with bi-functionalized glass surfaces conserves a defined and highly controlled ECM composition.

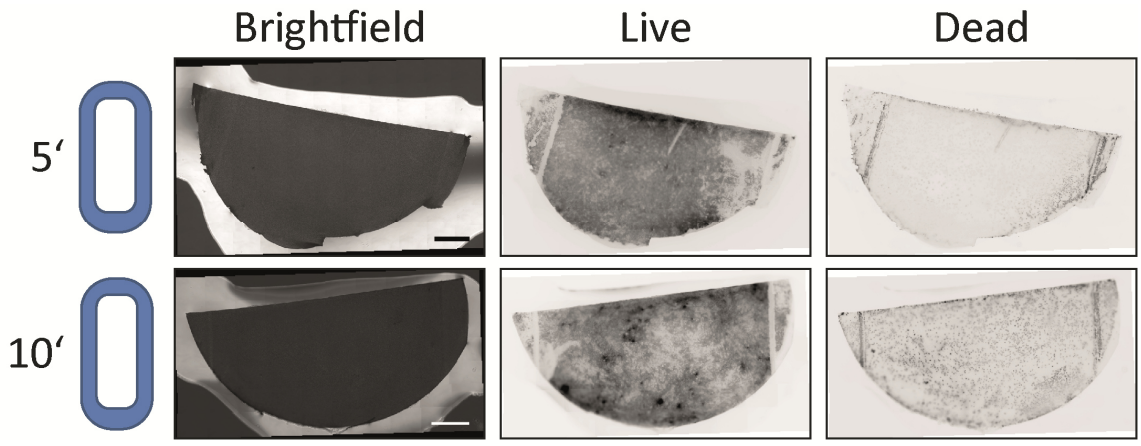

Figure 37: Weighed down teflon-molds kill HaCaT cells cultivated on polycarbonate membranes at contact side. HaCaT cells were grown and cultivated until full confluence on collagen I-coated polycarbonate membranes. Then, membranes were released from cell culture inserts and a wound was introduced by cutting the membrane. Membrane halves were immobilized in a cell culture dish using a teflon-based mold and subsequently ballasted with 9.8 N for 5 min. Live-dead staining reveals no viability of cells at contact side with molds. Scale bar: 1000 µm.

In order to successfully mechanically fixate membrane cultivated keratinocytes on various substrates, different molds of different materials were designed and tested. PDMS is a silicone-based elastic material. Its mechanical properties can be tuned within one latitude. By casting it into negative forms unlimited designs are possible. The PDMS design shown here was created by pouring unpolymerized PDMS in respective cell culture dishes and subsequently manually cut them in the desired shape. To get more standardized shapes it would be possible to build respective negative forms as a template which are filled with the liquid PDMS. It has been reported that repeatedly pressure stimulation of HaCaT cells with teflon weights induced a multilayered culture growth as well as adaption of cytokeratin expression (Görmar *et al.*, 1993). To prevent pressure-derived adaptions in cellular

phenotype I aimed to kill those cells which lay directly under the PDMS mold. Even though the PDMS-based molds generally worked in mediating HaCaT migration, they did not come with the desired properties in killing underlying cells. This is most probably explained by the PDMS' elastic properties and insufficient pressure transfer. To solve this problem, teflon molds were designed and commissioned to the in-house workshop. An additional benefit of the teflon material is that it is autoclavable thus reducing dramatically contamination events compared to the PDMS molds, which were disinfected with 70 % ethanol. The design came with a small contact area to provide maximal pressure transfer as well as a maximum width of the inside chamber to maximize the area which can be microscopically recorded. To further improve phase contrast imaging, the teflon mold was flooded with cell culture medium. To reduce the volume of medium a second generation of teflon molds was designed with a lower height of 6 mm instead of 10 mm (Figure 34 G).

3.3.6 Mechanical fixation mediates wound-induced collective migration of HaCaT monolayers

Having set up a mechanical immobilization of HaCaT monolayer carrying membranes, where cells at the contact side with the mold are specifically killed, it needs to be elucidated whether this fixation strategy still enables migration. For this, the before-described approach was applied (Figure 29 A) and different ECM surfaces were offered. As the two-stage ECM wound model was just about to be established, the molecular properties of the extracellular environment were kept constant. Thus, both the ECM 1 and ECM 2 were based on collagen I or collagen I related substrates. Even though the binding ligand was kept constant, mechanical variances from ECM 1 (membrane) to ECM 2 (glass) could not be excluded. Therefore, substrates with different mechanical properties were provided. Following this strategy, polycarbonate membranes were collagen I-coated (ECM 1) and subsequent substrates presented a collagen I coating, collagen I gels or RGD as a binding motif, which is found in collagen I (ECM 2). HaCaT cultivated membranes were produced and mechanically fixated (Figure 38 A). Time-lapse imaging was performed to observe HaCaT cell migration. Cell movement at the cut side of the membrane was observed within one hour after cutting. Transition from the membrane to the underlying ligand-presenting substrate occurred from 4 h on and continued for the next 60 h of recording. Figure 38 B depicts the collective character of the migration process. HaCaT cells did not traverse from the membrane to the second substrate if surfaces were passivated with no cellular binding motifs presented. As one cell-cultivated membrane is always cut in two equal halves, both halves were used in the experiment. Thus, the identical treated counterpart of the passivation sample always faced a substrate covered with binding ligands. Therefore, lack of migration can be confidently ascribed to lack of binding ligands and not to sample variances evoked by cultivation variances. Additionally, continuous cell movement at the cut side was observed, proving viability of membrane-cultivated cells, independently of presented surface.

Plotting the relative migration normalized to the invaded area after 24 h illustrates the continuous cell migration in the open space in front of the membrane. Whereas migration does not occur on passivated substrates, a clear increase in relative migration is observed for collagen I gels, collagen I-coated and cRGD functionalized surfaces (Figure 38 C). After 48 h, a significant difference in relative migration between collagen I gels ($p = 0.0301$) and passivated as well as collagen I -coated surfaces ($p = 0.0003$) was detected (Figure 38 D).

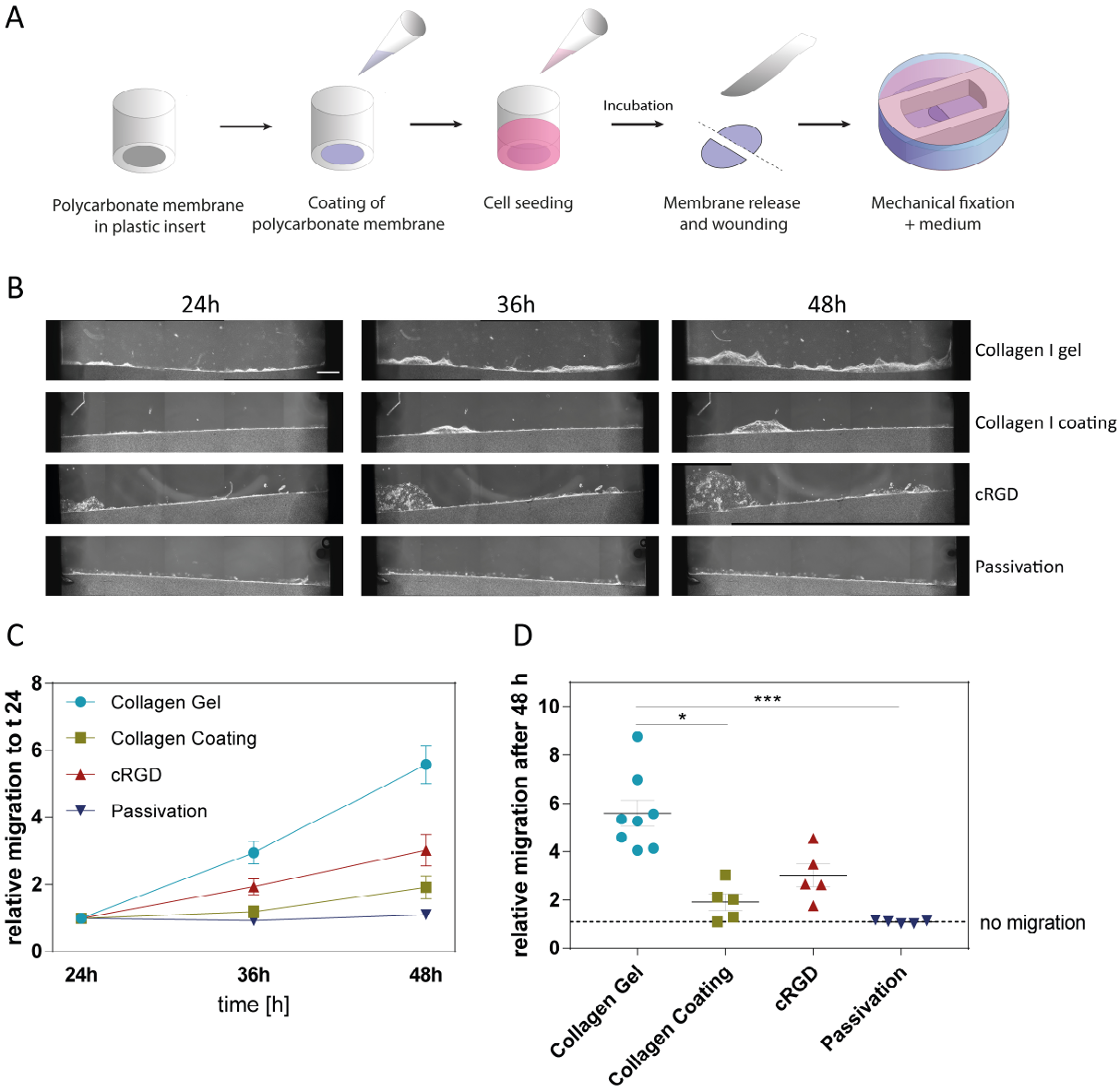

Figure 38: Mechanical fixation mediates wound induced collective migration of HaCaT monolayers/cells. 2D epidermal models collectively migrate after wound insertion on collagen I gels, collagen I-coated and cRGD functionalized glass surfaces. In the absence of a binding ligand no cell migration is observed (Passivation). (A) Schematic representation of the final procedure to produce membrane cultivated HaCaT monolayers, their wounding and subsequent mechanical fixation (B) Depicted are overviews (stitched from 5 single images) from the cut-side of the monolayer-carrying membrane after 24, 36 and 48 h. (C) Relative cell-covered area over time on indicated surfaces after 24, 36 and 48 h (D) Relative migration after 48 h normalized to the invaded area after 24 h. The data represents means ± SEM from three independent experiments. Kruskal-Wallis test was used to identify significant differences. Scale bar: 500 µm.

Taken together, I showed that a mechanical fixation strategy based on customized teflon molds mediates migration of membrane-cultivated HaCaT cells on glass surfaces with collagen I gels, collagen I coating, as well as nanostructured and cRGD functionalized glass surfaces.

Membrane-cultivated HaCaT cells showed collective migration behavior on all provided surfaces upon mechanical fixation (Figure 38). A different observation was made for Figure 32, where an end-point analysis of migrated cells on collagen I gels did not indicate a collective migration. However, there, fixation of HaCaT cultivated membranes was achieved using collagen I glue. Thus, it is possible that the divergent observation might be due to the different fixation strategies.

In agreement with past migration studies and the formation of leader cells, the migration readiness is not identical throughout the wound site. It is hypothesized that upon epithelial collective migration single leader cells at the edge of the monolayer are "elected" by their follower cells based on intercellular tension and forces (Vishwakarma *et al.*, 2018). Therefore, single migration fronts emerge throughout the wound site which I also observed in my experiments (Figure 38). A general observation was that such migration tongues often preferentially formed at the edge of the teflon mold. The reason for this is an open question which needs to be further investigated. It might be that lysed cells by the teflon mold could set the adjacent cells into a higher migration willingness due to released cytoplasmic factors (so called damage associated molecular patterns; DAMPs; Niethammer, 2016). Another reason might be that the membrane sites close to the teflon mold have better contact to the substrate and thus the transition from the membrane to the substrate is facilitated. Also, it would be interesting whether the number of migration fronts would increase upon increase of epithelial stress by initially seeding HaCaT cells in a higher density in the cell culture inserts.

Interestingly, for a few hours, cell movement at the cut side was observed, but transition from the membrane to the underlying substrate did not yet occur. A lag phase before re-epithelialization has been reported during which keratinocytes adapt their integrin expression to the new ECM in order to acquire migratory competence (Grinnell, 1992). For this reason, the presented ECM nature was kept constant to collagen I or its binding motifs. Therefore, additional explanations besides an adaption in integrin expression are conceivable. Maybe the new substrate first needs to be processed and collagen fibers need to be rearranged to enable HaCaT cell adhesion, which takes time. This would explain why HaCaT cells migrated better on cRGD functionalized glass surfaces than on collagen I -coated surfaces, as here no further processing to outreach binding sites is needed. Also, the height difference between the membrane and the underlying substrate might delay HaCaT migration. As the transition for collagen I gels occurred faster, it is to be assumed that the gel improved the transition from the membrane to the substrate, maybe due to its elastic properties which might reduce the height distance. This would further explain the higher total migration observed for collagen I gels compared to collagen I-coated or cRGD-functionalized glass surfaces, even though a softer substrate is typically disadvantageous to migration in direct comparison to stiffer substrates (Wang *et al.*, 2012).

Interestingly, the relative migration for collagen I and cRGD functionalized glass surfaces was similar, indicating that cRGD is a good replacement for the full collagen I protein.

To sum up, I demonstrated that such 2D epidermal models can be used to observe migrational activities of keratinocytes in time-lapse imaging on collagen I gels, collagen I -coated glass surfaces as well as on minimalistic, highly-defined ECM models, where only one single binding motif is presented. To initiate HaCaT migration, a simple cut was applied to introduce a real wound site – in contrast to other wound assays which use confinements. However, all presented steps of the development have also been performed with punched membranes, resembling another type of wounding (Appendix, Figure 51). Referring back to the scientific question, a punched wound site might be advantageous over a cut wound site, e.g. if one is interested in intercellular signaling of wound adjacent cells on the opposing sites of the wound site, or if the system should be utilized to investigate the contribution of the ECM environment on the formation of an acto-myosin based contractible ring around the wound site. In this example, cells form a subracellular actomyosin ring around the wound site involving several wound adjacent cells (Schwayer *et al.*, 2016). Upon contraction wound closure is achieved.

As the wound site is introduced in a separate step, the underlying substrate is not affected by the wounding procedure and thus the system can be combined with sophisticated highly defined and controlled ECM mimicking substrates. It has been shown that time-lapse imaging of several positions in parallel is possible and the mechanical fixation still ensures sufficient fixation. Thus, this fixation strategy is also suited to perform more advanced analyses of collective cell migration such as particle imaging velocimetry (PIV). On top of this, the established mechanical fixation also works on gel-like structures. Therefore, even force-sensing measurements such as traction force microscopy (TFM) can be approached. Furthermore, the developed system can be tuned according to the research question by utilizing another cell type, be it cell lines (independence of donor variations) or primary cells (closer to *in vivo* situation). On top of that, even 3D skin tissue samples or artificially generated 3D human tissue constructs can be mechanically fixated on highly defined substrates and thus utilized.

3.3.7 Bi-functionalized glass surfaces with varying amount of HA mediate HaCaT migration

Many studies examine the role of HA on migration in cutaneous wound healing models by applying exogenous HA (Ghazi *et al.*, 2012; D'Agostino *et al.*, 2015, 2017). However, during re-epithelialization it is not only HA which changes in abundancy and size but also other components of the ECM, for example upon maturation of the provisional matrix to the granulation tissue. So in order to examine the role of HA on migration and proliferation processes, one also needs to integrate changes in the ECM environment. Therefore, in a final experiment I combined the established bi-functionalized glass surfaces with varying amount of HA and different binding ligands (cRGD and EPDIM) with

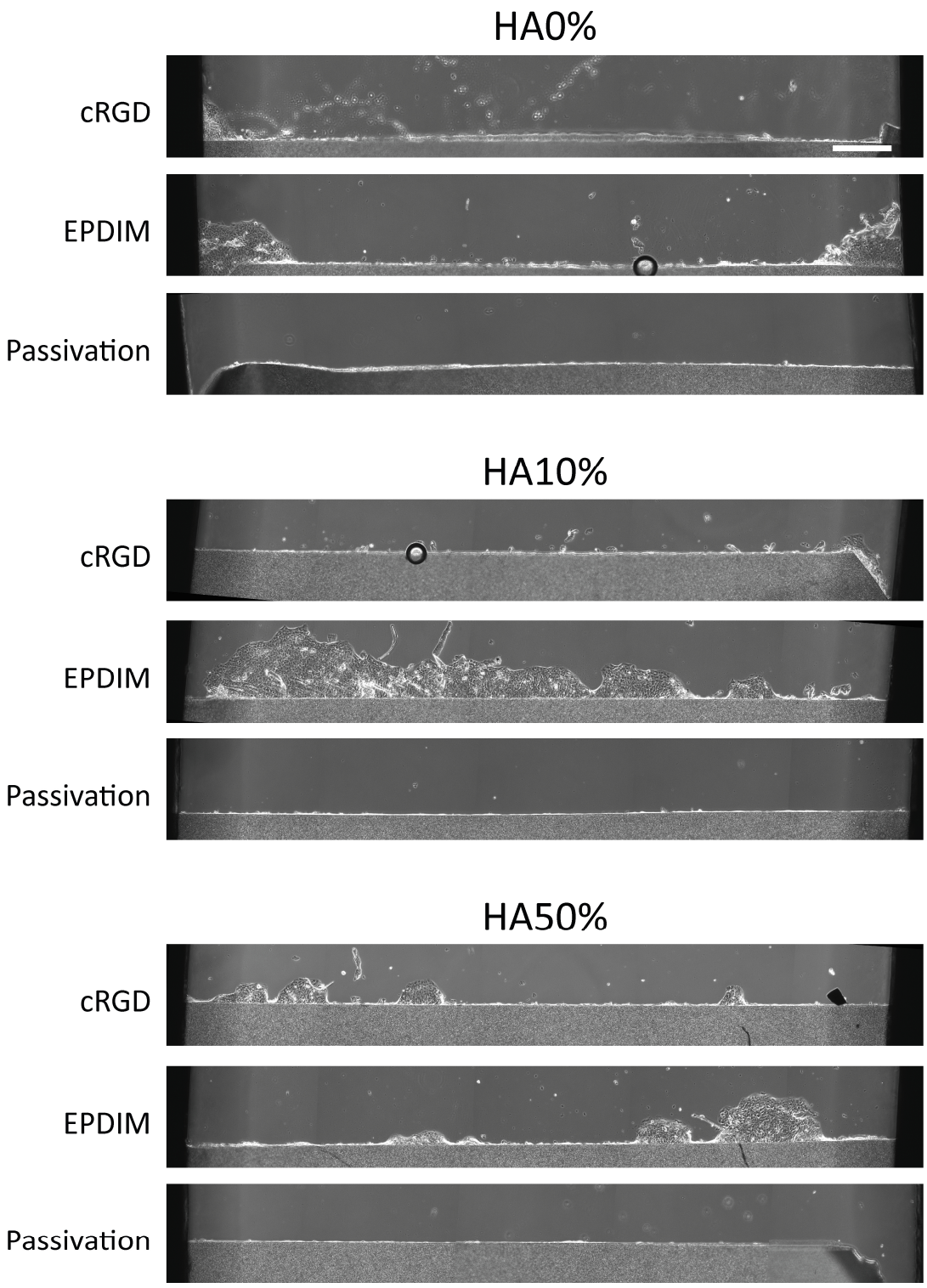

Figure 39: HaCaT migration on bi-functionalized glass surfaces. 3 x 10^5 cells were seeded on collagen I -coated polycarbonate membranes and cultivated for 24 h. Membranes were cut into halves and placed on bi-functionalized glass surfaces with different amounts of immobilized HA (HA0%, HA10%, HA50%) and functionalized with either cRGD or EPDIM. Passivated surfaces with no HA and no binding ligand served as control. Depicted are top-views (stitched from 5 single images) from the cut-side of the monolayer-carrying membrane after 72 h. Result of one representative experiment of two experiments. Scale bar: 500 µm.

wounded and mechanically fixed 2D epidermal wound models. First data revealed cell migration after 72 h for all samples where either cRGD or EPDIM with varying amounts of HA was presented (Figure 39). No migration was observed for the passivation control without binding ligand or HA (Figure 39). For quantitative statistics, more replicates are needed to correlate the amount of immobilized HA and single binding motifs with the migration capacity of membrane-cultivated HaCaT cells.

Taken together this shows that the combination of bi-functionalized glass surfaces and the two-stage ECM wound model successfully mediated cell migration of membrane-cultured HaCaT cells. Further research will unravel how exactly HA affects the migration as well as proliferation during re-epithelialization in cross-talk with single integrin-addressing binding motifs. It will be interesting whether an HA-mediated effect on focal adhesion formation, as seen in figure (Figure 28), will also be observed in the dynamic migration system and whether this will have an either pro- or anti-migratory effect.

In order to identify the impact of the ECM on keratinocyte migration, proliferation and differentiation tools are needed. I developed a two-stage ECM wound model where I demonstrated that such 2D epidermal models can be used to observe migrational activities of keratinocytes in time-lapse imaging on collagen I gels, collagen I-coated glass surfaces as well as on minimalistic, highly-defined ECM substrates, where either only one single binding motif or a second component such as HA is orthogonally presented. With this two-staged ECM wound model, it will be possible to better reveal the contribution of the ECM composition on impaired, delayed or failed re-epithelialization and thus how imbalanced ECM possibly provokes chronic, non-healing wounds or hypertrophic scars.

4 Conclusion and Outlook: The versatile two-stage ECM wound model system

For the first time a comprehensive study of a wide range of hyaluronic acid (HA) sizes (5, 60, 700 and 1800 kDa) applied in different concentrations (5, 50, 500, 1000 µg/mL) within the frame of re-epithelialization and within one and the same experimental set-up was performed for HaCaT cells being cultivated on collagen I-coated glass surfaces. Collagen I is a main component of the granulation tissue, the extracellular matrix (ECM) of a progressed wound site. Upon apical administration of HA, I showed that HA hampers migration on collagen I-coated glass surfaces in a rather concentration-dependent manner whereas in terms of proliferation HA has a pro-proliferative effect under conditions of low density on cell culture plastic. As the extracellular matrix (ECM) resembles the wound healing stage I aimed to identify HA's role on re-epithelialization in dependence of the underlying ECM. Hence, I provided surfaces coated with fibronectin, laminin 332 and collagen I. However, high variances in replicates impeded the dissection of the ECM contribution of apically applied HA solutions of different molecular weight (MW) and concentration on migration and proliferation.

Hence, I developed a defined and highly controllable two-component ECM environment which presents immobilized HA and provides reduced interaction sites for integrins. In order to address different integrin-binding families I functionalized gold-nanostructured, passivated glass surfaces with the established cRGD and a novel peptide, EPDIM as cell binding ligands. With these controlled interfaces EPDIM with an N-terminal linker was proven to be a suited cell binding ligand for functionalization of gold-nanostructures with an inter-particle spacing of 52 ± 9 nm. Additionally, I investigated whether end-alkylated HA of 5, 10 and 60 kDa can be bound to azide-presenting surfaces via click chemistry. Surface saturation with end-alkylated HA was ascertained via Quartz crystal microbalance with dissipation monitoring (QCM-D) experiments and accessibility of surface-bound 5 and 10 kDa HA by the hyaladherin aggrecan proved bioactivity of immobilized HA. HaCaT adhesion and subsequent spreading on bi-functionalized glass surfaces with cRGD or EPDIM as a binding ligand together with three different concentrations of immobilized HA was observed. Surfaces presenting HA without additional adhesive peptides did not mediate HaCaT cell adhesion.

To mimic the dynamic changes in ECM composition during wound healing (e.g. when the provisional matrix evolves into granulation tissue) a two-stage wound model system was developed. For this keratinocyte monolayers were cultivated on collagen I-coated polycarbonate membranes. Formation of confluent monolayers was achieved within 24 h. After, HaCaT-cultivated membranes were wounded via cutting, reflecting a real wound site, and placed on substrates of interest. As in my model the wounding procedure is, in contrast to commonly applied approaches, not performed on the substrate but in a separated step before assembling cellular membrane and surface, surface properties are not mechanically impaired. Customized molds enable the mechanical fixation of membrane-cultivated

HaCaTs on any desired surface without the need of collagen I glue thus ensuring a clean and well-controllable ECM environment without unintentional insertion of collateral ECM molecules representing a clear advantage compared to the usage of collagen I glue. Finally, I demonstrated that such 2D epidermal models can be used to observe migrational activities of keratinocytes in time-lapse imaging on collagen I gels, collagen I-coated glass surfaces as well as on minimalistic, highly-defined ECM models, where only one single binding motif is presented. Furthermore, migration was also mediated upon providing bi-functionalized glass surfaces where the binding ligands cRGD or EPDIM were presented orthogonally with HA of varying concentration.

The modular two-stage ECM model in combination with bi-functionalized glass surfaces is capable to reveal HA's signaling role in cooperation with other ECM molecules on re-epithelialization in future applications. This system is flexible and highly tunable in its complexity to adapt it to a wide variety of scientific questions.

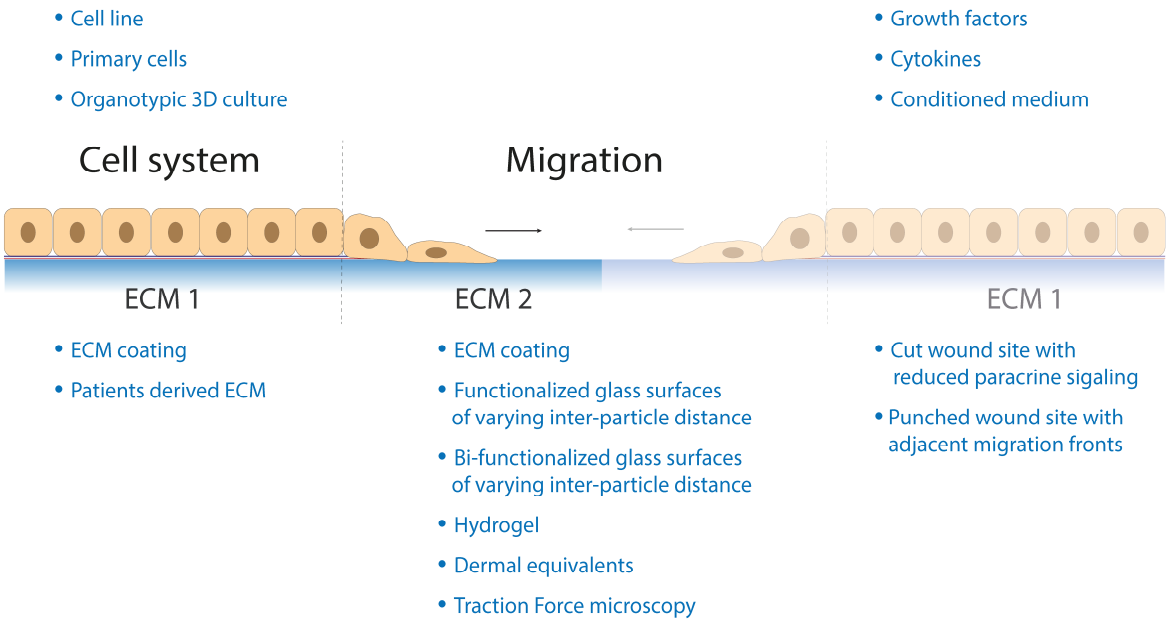

Figure 40: The versatile two-stage ECM model. Expandable list of modification and adjustment sites within the model.

The general experimental design established in this thesis can be customized in multiple ways including the variation of the cell system, the ECM model interfaces as well as additional supplements in the cell culture medium (an expandable list is found in Figure 40). During the establishment of this system the polycarbonate membranes have been coated with collagen I in the first stage (ECM 1, Figure 40). However, collagen I can be replaced by other proteins such as fibronectin or laminins. Also more sophisticated coating procedures are conceivable, e.g. sequential cultivation of the membranes first with

fibroblasts (maybe derived and isolated from a patient's chronic wound site) for ECM deposition and second with keratinocytes.

One is also flexible regarding the origin of the applied cells. In my set-up, the cell line HaCaT has been employed due to its stable phenotype which is (widely) independent of passaging. In contrast to that, function of primary cells isolated from tissues/organs can maintained *in vitro* only for a limited period of time. Primary cells, however, come with the advantage that they resemble better the *in vivo* characteristics which might be advantageous depending on the specific research question. Furthermore, by using primary keratinocytes derived from a patient's sample (e.g. diabetes) or aged tissue would help to specifically examine re-epithelialization in dependence of underlying medical conditions. The two-stage ECM system has been developed to flexibly switch from 2D system to 3D systems. Due to the mechanical fixation strategy, not only cellular monolayers cultivated on polycarbonate membranes can be utilized but the two-staged ECM model even enables the usage of membrane-cultivated organotypic 3D epidermal tissues.

The second stage ECM 2 (Figure 40) compartment is also highly flexible. Simple straight forward protein coatings are feasible, as well as highly defined ECM mimicking substrates with only one or two ECM ligands being provided. I established bi-functionalized glass surfaces where only HA and a second, integrin-addressing binding ligand is presented. Two different binding ligands, representing different stages of wound healing were employed: the fibronectin binding motif (c)RGD, predominant in granulation tissue as well as the newly established EPDIM ligand as binding motif for the laminin receptor α3β1, which is required for basement assembly (Longmate and DiPersio, 2014). A few highly specific cell binding ligands are available which selectively address single integrin-heterodimers (Kapp *et al.*, 2013; Rechenmacher *et al.*, 2013). Those are a powerful tool if one is interested in the contribution of HA-receptor interactions on selective integrin heterodimers during re-epithelialization.

The ligand presentation can be further adjusted by varying the inter-particle spacing. The BCML approach allows for spacing from 25 to 250 nm (Lohmüller *et al.*, 2011). With the aim to reduce structural complexity of HA, 5 kDa HA, which is expected to occur mostly in a rather rod-like conformation, was immobilized. Naturally, once a terminal alkyl group has been introduced higher (as well as lower) MW of HA can also be immobilized. QCM-D experiments showed a successful surface immobilization of 10 kDa as well as 60 kDa (Figure 19, Appendix, Figure 46). It would be interesting whether even higher MW HA can be applied or whether the more coil-like conformation would eventually mask the alkyl group needed for immobilization. Additionally, by tuning the ratio of azide groups (PEG3000azide) presented on the surface the number of immobilized HA molecules can be regulated. The MW of HA as well as PEG sizes, and the ratio of azide carrying PEGs determines the dynamical range before the surface would be saturated with HA. By using short HA in a high density the number of binding sites per area would be increased, mimicking a longer polymer size. Thus, it would be interesting, whether and how HA receptor clustering (e.g. CD44) would be affected by tuning the density of surface immobilized HA of small MW.

Furthermore, an alkyl moiety can not only be introduced at the end of the HA polymer, but HA can also be side-alkylated (Minsky, Antoni and Boehm, 2016). An end-alkylation introduces only one reaction group per molecule HA whereas a side-alkylation can introduce several alkyl groups per HA polymer. Both, immobilized end- and side-alkylated HA has been shown to be bioactive (Minsky, Antoni and Boehm, 2016). The latter comes with an increase in 3D HA complexity, as one and the same molecule might be modified at several sites and thus has more than only one possible interaction site with the surface and thus binding sites for cells might be sterically masked. Consequently, this would result in an ECM environment of higher complexity. A chemical modification of the HA polymer at the reducing end brings the advantage of a linear conformation of HA (if LMW HA is utilized) and so interrelates with a theoretical higher accomplishable molecule density on the surface as steric hindrance is reduced. Of course, a very high packing density in turn could again prevent hyaladherin binding. However, QCM-D measurements proved HA's bioactivity (Figure 21).

The novel approach to mechanically fix membrane-cultured keratinocytes by customized teflon molds is not only suited for rigid but also for gel-like substrates. This has been proven with collagen I gels, which successfully mediated cell migration (Figure 39). Based on this result, I expect that the two-stage ECM model would also work with other (HA-based) hydrogels or dermal equivalents, where dermal fibroblasts are embedded in collagen I gels (Figure 8 A). Moreover, by using polyacrylamide (PAA) gels with incorporated fluorescent carboxylated polystyrene beads, traction force microscopy (TFM) can be applied. TFM measures the traction cells exert to their underlying substrate. For this, the displacement of the fluorescent beads upon cellular force exertion is transcribed into displacement vectors. Therefore, an image before and after force application needs to be taken. With the help of these displacement vectors the cell-substrate traction can be reconstructed. Furthermore, using a force balance algorithm also the stress within the monolayer, namely cell-cell traction, can be calculated (Vishwakarma *et al.*, 2018). A typical TFM experiment looks like this: cells are seeded under sterile conditions on top of substrates with e.g. varying stiffness. After cell adhesion (i.e. cells apply force on the substrate to hold fast onto the substrate) the PAA gel and thus the bead distribution is recorded. To determine the initial bead localization under "relaxed" conditions cell-substrate interactions need to be resolved. This is achieved by simple trypsination of cells. Thus, TFM is a kind of end-point measurement and samples cannot be further processed (e.g. being fixed with subsequent immunostaining). However, in my migration system it is not necessary to trypsinize cells at the end of the TFM measurement. As cells are not directly seeded on the substrate of interest but initially on polycarbonate membranes, which are in a second step transferred onto the TFM gels, gels (and thus the fluorescent bead distribution) can already be recorded upon migration initiation. On top, TFM gels can also be gold-nanostructured and by this a more defined ECM environment can be created (Aydin *et al.*, 2010; Di Russo *et al.*, 2019).

The two-stage ECM model system also allows for variations in the wounding procedure. Membrane cultivated keratinocyte monolayers can be either cut to have a linear wound site, or membranes can be punched which generates a circular wound site. Commercial available biopsy

puncher with varying diameter from 1 mm on are available. The cut wounding procedure reduces paracrine effects by another opposing migration front. The punched wound model is expected to come with more paracrine effects and, as the whole wound site is surrounded by cells the formation of a supracellular contractile actomyosin ring is enabled. It has been reported that such contractile actomyosin rings are formed upon wounding of embryonic or adult tissues (Schwayer *et al.*, 2016).

Besides the modifications listed above, additionally conditioned medium or specific signaling molecules such as cytokines and growth factors can be dissolved in the cell culture medium and would be apically presented to migrating cells.

Chopra *et al.* (2014) postulated a role of HA in surpassing mechanical information from the extracellular environment. They observed that HA is able to override the mechanical signaling of integrins and by this induced a cellular phenotype on a soft tissue which is usually observed on very rigid substrates (Chopra *et al.*, 2014).

In this thesis I employed bi-functionalized glass surfaces and altered their functional groups: Only HA and a second, integrin-addressing binding ligand were presented on an otherwise passivated background. Such bi-functionalized glass surfaces are suited to examine the interplay between HA receptors and integrins. Applying BCML the spacing of presented ligands can be set. Additionally, the inter-particle space can be functionalized with HA (of different size). It would be interesting to investigate cell spreading behavior and focal adhesion formation according to various inter-particle spacing with constant HA density. Applying the two-stage ECM model would further unravel the impact of increased distance between integrin addressing binding ligands in combination with HA surface density.

5 Appendix

A. Figures

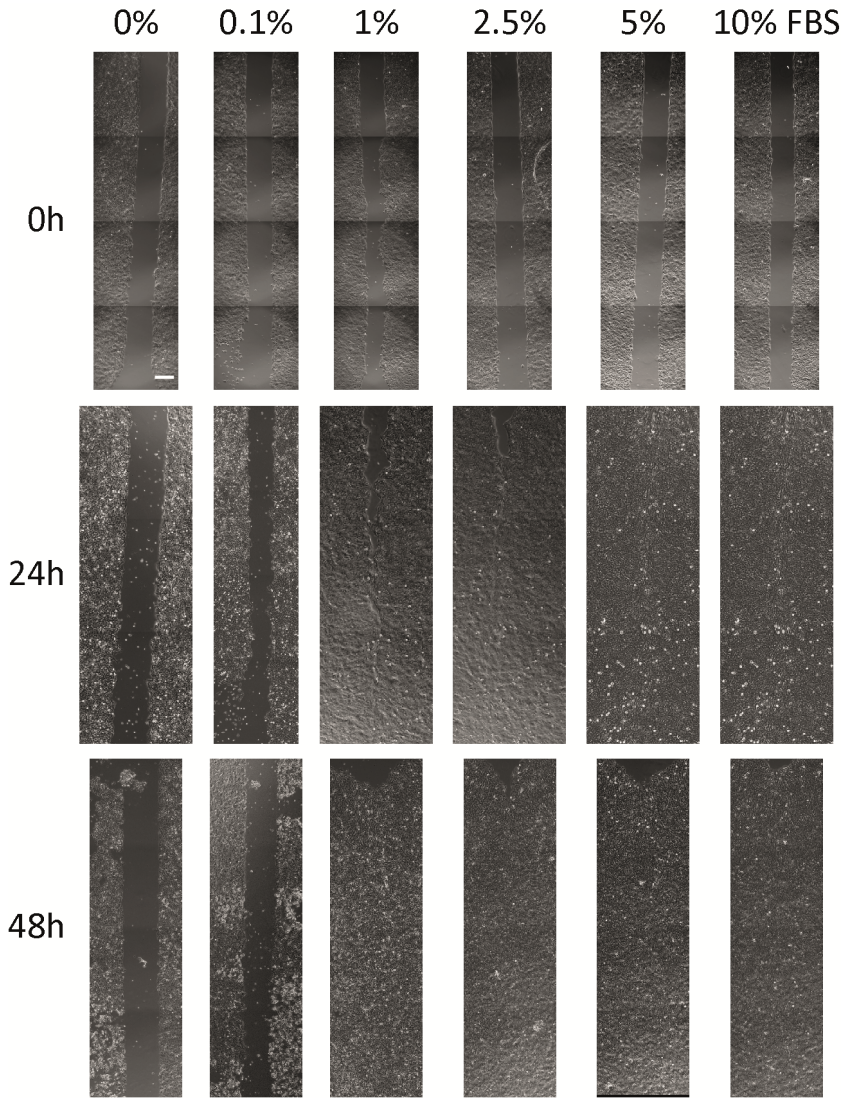

Figure 41: HaCaT migration for 48 h in dependence of FBS supplementation. An artificial wound site was generated by seeding 70 K HaCaT cells in each chamber of a two-chambered confinement in DMEM supplemented with 10 % (v/v) FBS. After 24 h of cultivation the confinement was removed and cell culture media replaced by DMEM with 0, 0.1, 1, 2.5, 5 and 10 % (v/v) FBS. Images of the artificial wound site were taken directly after confinement removal and after 24 and 48 h. Scale bar: 300 µm.

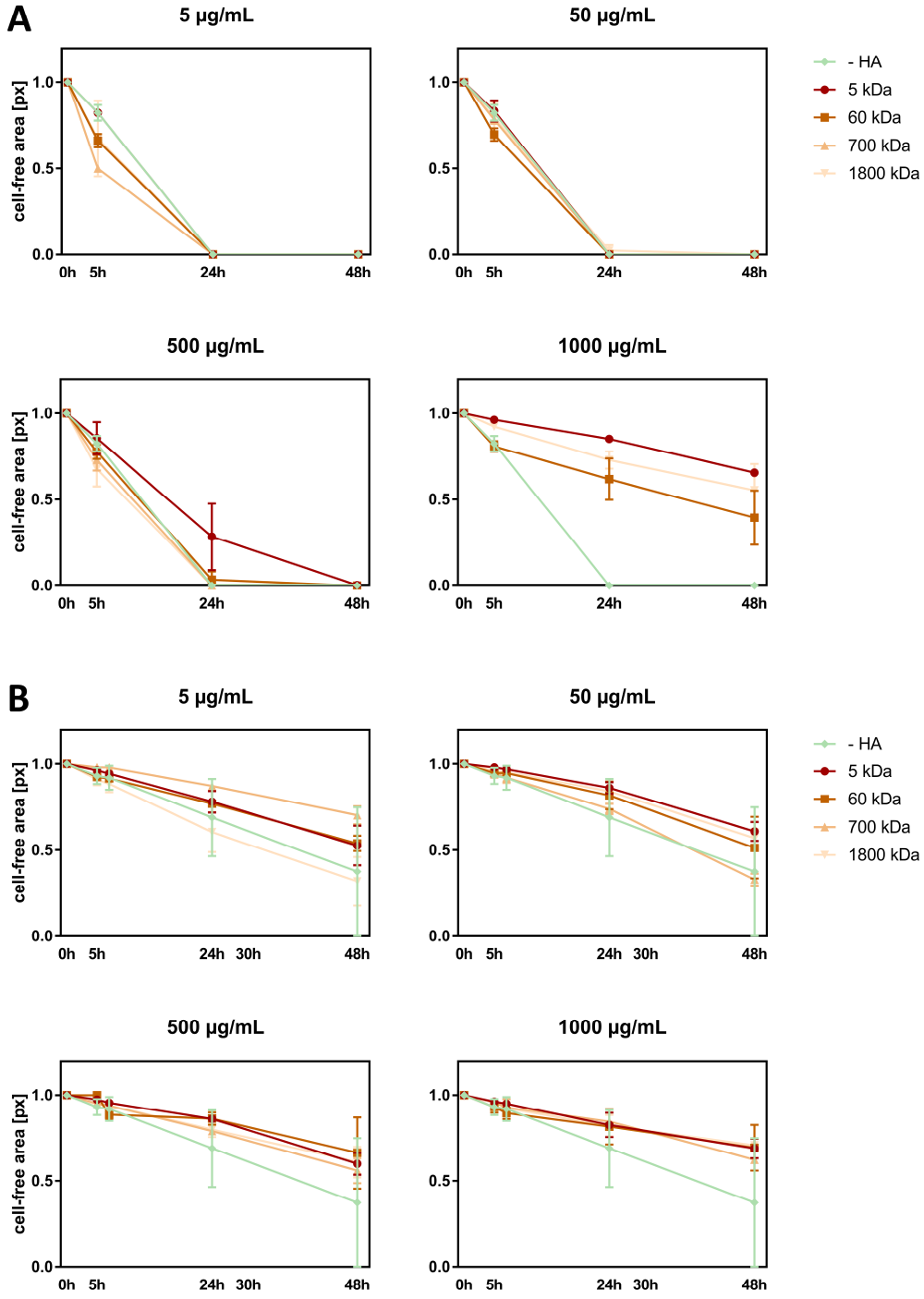

Figure 42: HaCaT migration into cell-free area dependent on different HA sizes and concentrations over a total observation time of 48 h. An artificial wound site was generated by seeding 7 x 104 HaCaT cells in each chamber of a two-chambered confinement in DMEM supplemented with 10 % (v/v) FBS on collagen I-coated glass surfaces. After 24 h of cultivation the confinement was removed and cell culture media replaced by DMEM 1 % (v/v) FBS with respective HA species (5, 60, 700 and 1800 kDa) in the indicated concentrations (0, 5, 50, 500 and 1000 µg/mL). Images of the artificial wound site were taken directly after confinement removal and after 5, 24 and 30 h. The cell-free area was semi-automatically determined following image segmentation. The graphs show two independent technical replicates with two replicates per condition, each value represents mean ± SD. The cell-free area was normalized to the cell-free area directly upon HA treatment at t0.

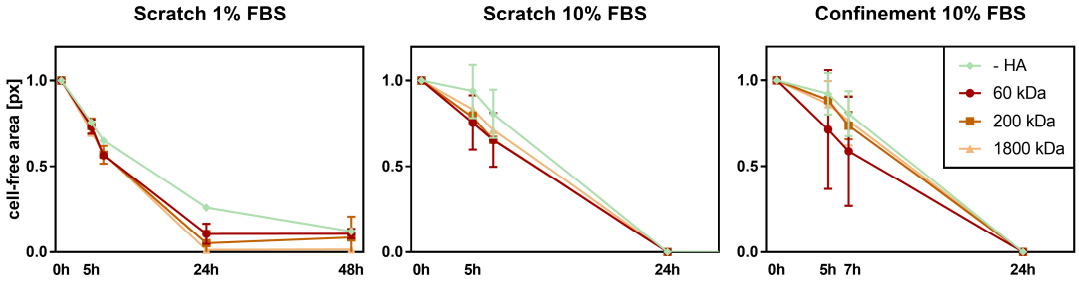

Figure 43: Cell-free area in dependence of vol% FBS and wounding strategy over a total observation of 48 h. HaCaT cells were seeded on collagen I-coated surfaces either directly in cell culture plastic wells or in each chamber of a two-chambered confinement in DMEM supplemented with 10 % (v/v) FBS. After 24 h of cultivation a wound site was introduced by either scratching the monolayer or upon removal of the confinement. Cell culture media was replaced by DMEM with indicated vol% FBS with respective HA species (60, 200 and1800 kDa) at a concentration of 1000 µg/mL. Images of wound sites were taken directly after confinement removal and after 5, 7, 24 and 48 h as indicated. The cell-free area was semi-automatedly determined following image segmentation. The cell-free area was normalized to the cell-free area directly upon HA treatment at t0. N= 2. Each point represents mean ± SD.

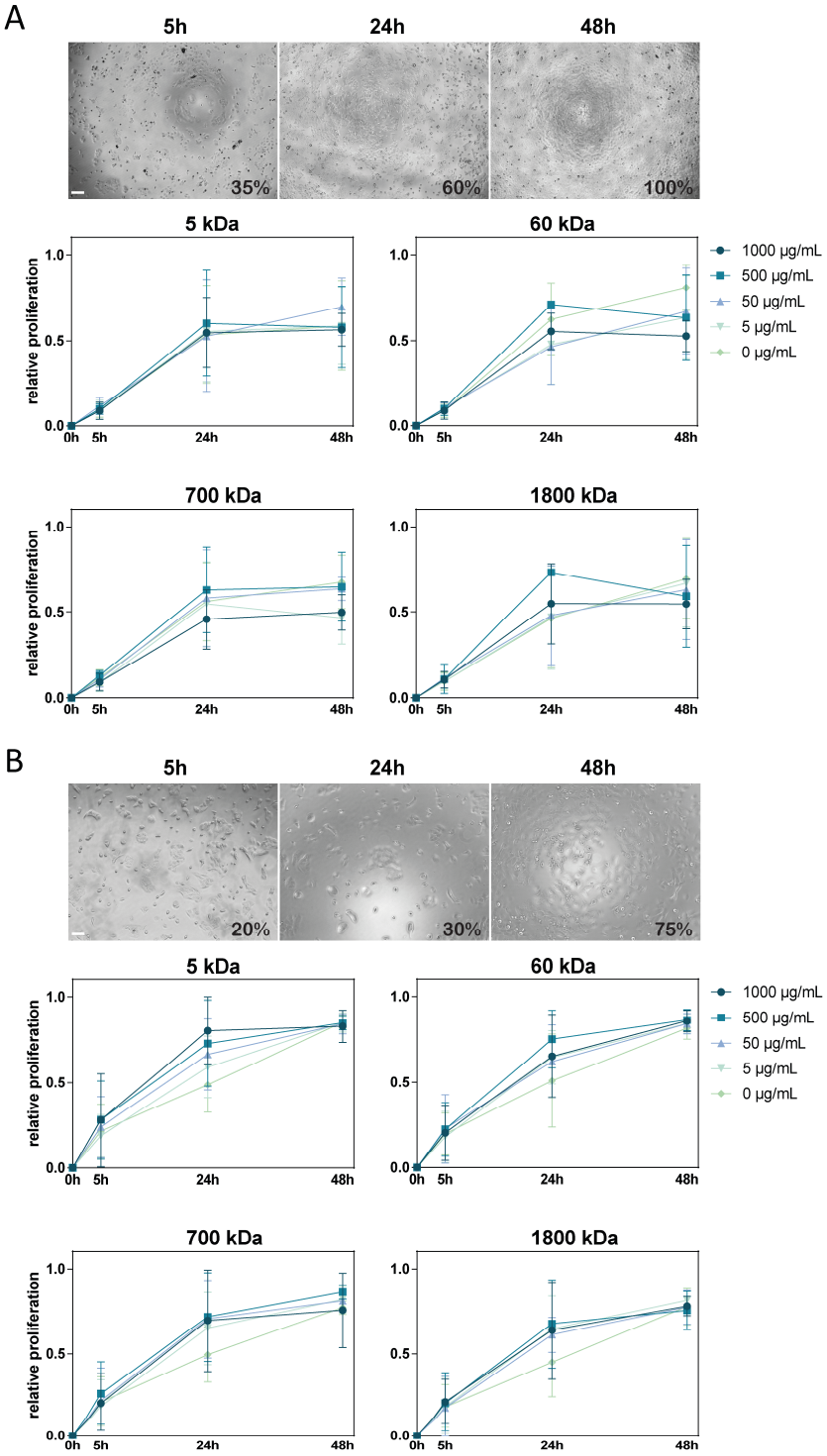

Figure 44: HaCaT proliferation in dependence of different HA sizes and concentrations as well as confluence over a total observation of 48 h. (A) 5 x 104 ("high" density) and (B) 2.5 x 104 ("low" density) HaCaT cells were seeded in DMEM supplemented with 10 % (v/v) FBS in one well of a 96-Well plate. After 24 h of cultivation cell culture media was replaced by DMEM 1 % (v/v) FBS with respective HA species (5, 60, 700 and1800 kDa, respectively) in indicated concentrations (0, 5, 50, 500 and 1000 µg/mL) together with EdU. Relative proliferation rate was determined by dividing the number of EdU stained cells by the number of Hoechst stained cells of an area of 380 x 380 µm. Six replicates per condition of two independent experiments each value represents mean ± SD. Representative brightfield images reveal confluence for samples without HA after indicated timepoints. (A) 10x objective, scale bar 100 µm, (B) 5x objective, scale bar 200 µm. Note: due to the small diameter of a 96-well plate the meniscus effect negatively impacts the quality of phase contrast images and is responsible for the halo in the center of the images.

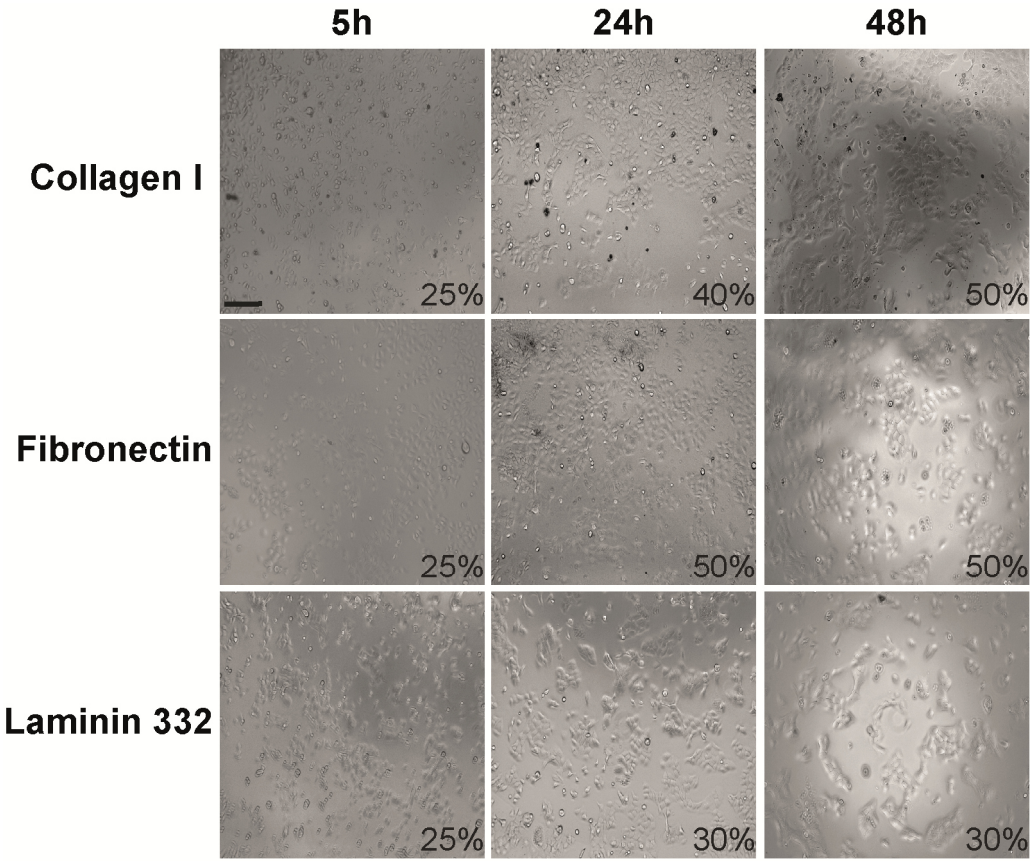

Figure 45: HaCaT confluence on different substrates over a total observation of 48h. 2.5 x 10^4 ("low" density) HaCaT cells were seeded in DMEM supplemented with 10 % (v/v) FBS in one well of a collagen, fibronectin or laminin 332-coated 96-Well plate. After 24 h of cultivation cell culture media was replaced by DMEM 1 % (v/v) FBS. Cell confluence was determined after 5, 24 and 48 h. Representative brightfield images reveal indicated confluence after indicated time points. Scale bar: 200 µm. *Note: due to the small diameter of a 96-Well plate the meniscus effect negatively impacts the quality of phase contrast images and is responsible for the halo in the center of the images.*

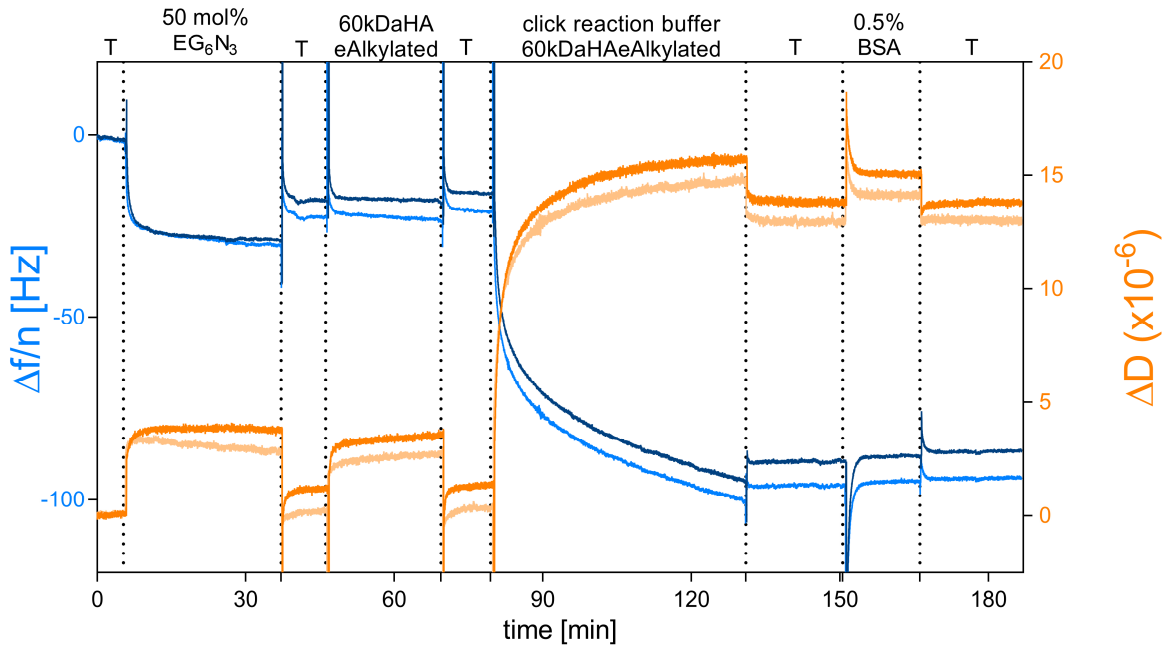

Figure 46: 60 kDa end-alkylated HA binds to EG_3OH/EG_6N_3 layers. SAMS of EG3OH and EG6N3 (1:1 mol%) were adsorbed on gold QCM-D sensors. Next, end-alkylated 10 kDa HA (10kDaHAeAlkylated, 2.5 mg/mL) (a) and end-alkylated 60 kDa HA (60kDaHAeAlkylated, 2.5 mg/mL) was added first without click reaction buffer and then with click reaction buffer in order to catalyze the copper(I)-catalyzed azide-alkyne cycloaddition. QCM-D graph of the seventh overtone, change in frequency (Δ f/n, shades of blue) and dissipation (Δ D, shades of orange) were monitored over time. B: 0.1 M TRIS buffer pH 8; depicted are two replicates (visualized by different color shades). *Note: the question of this experiment was whether alkylated 60 kDA HA generally binds to substrates presenting azide groups. Therefore, the QCM-D measurement was carried on even though no plateau for Δ f/n was reached upon administration of click reaction buffer with 60kDaHAeAlkylated.*

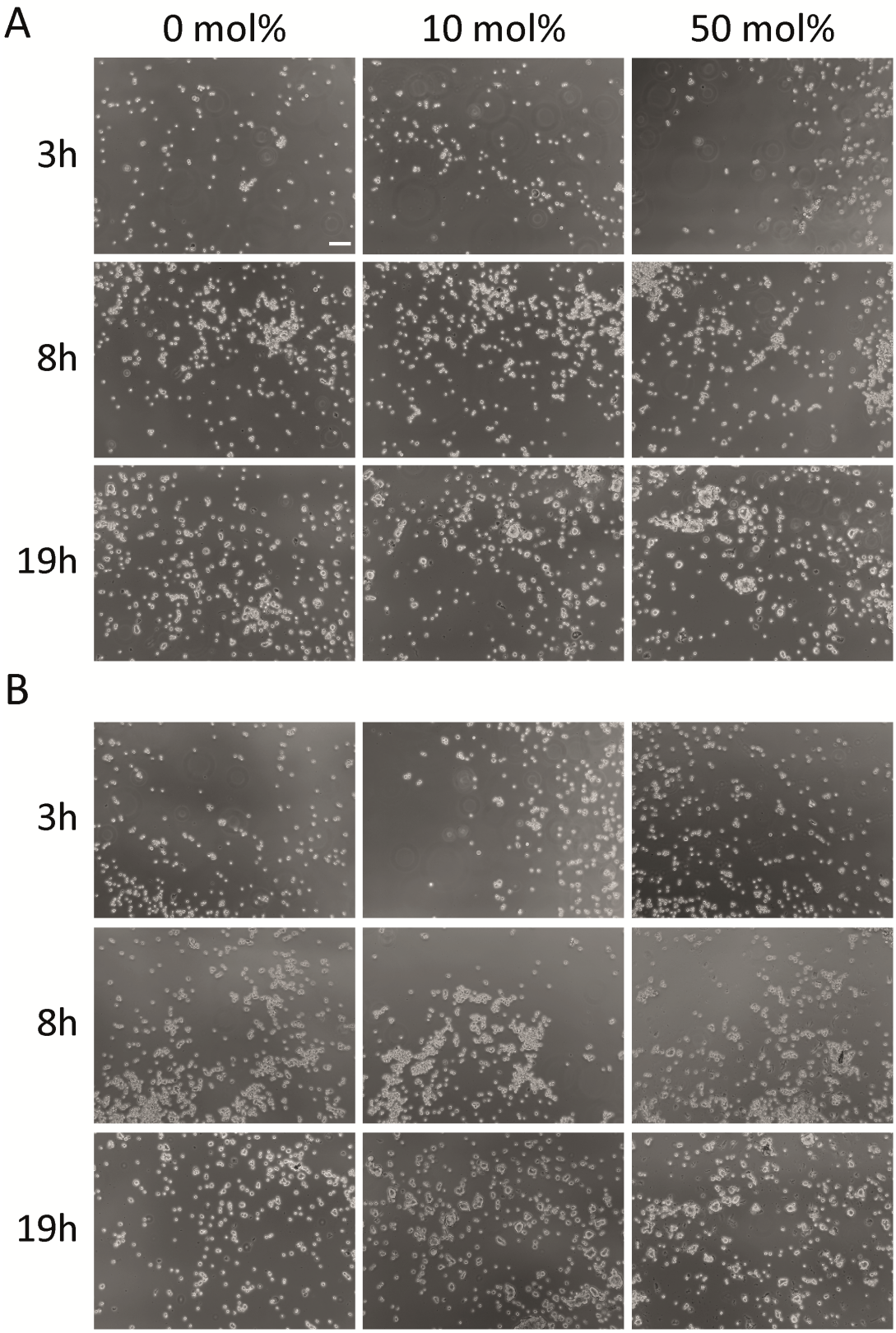

Figure 47: Wider surface overview of HaCaT cell adhesion on PEG2000/PEG3000azide passivated glass surfaces.

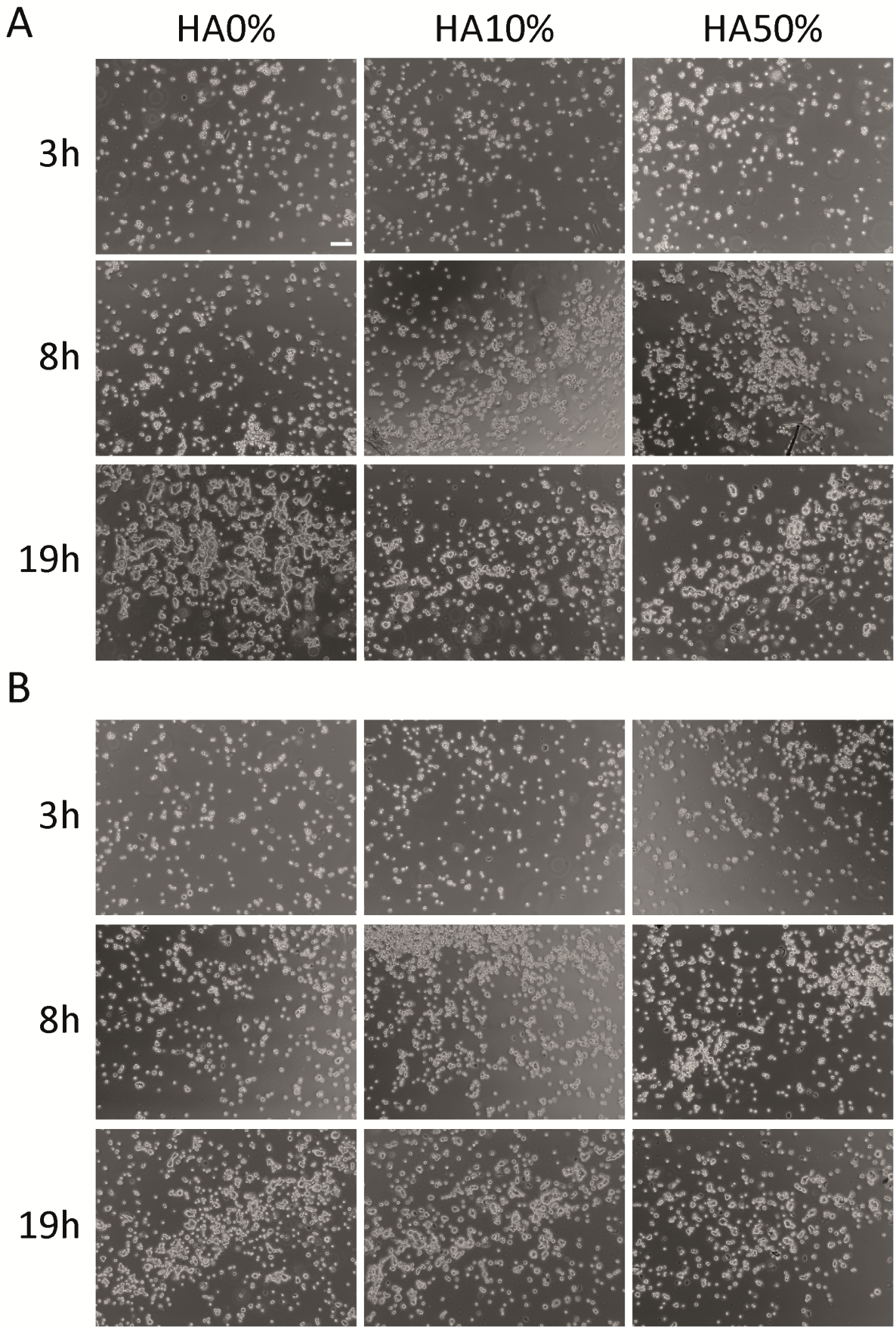

Figure 48: Wider overview of HaCaT cell adhesion on PEG2000/PEG3000azide passivated and HA immobilized glass surfaces.

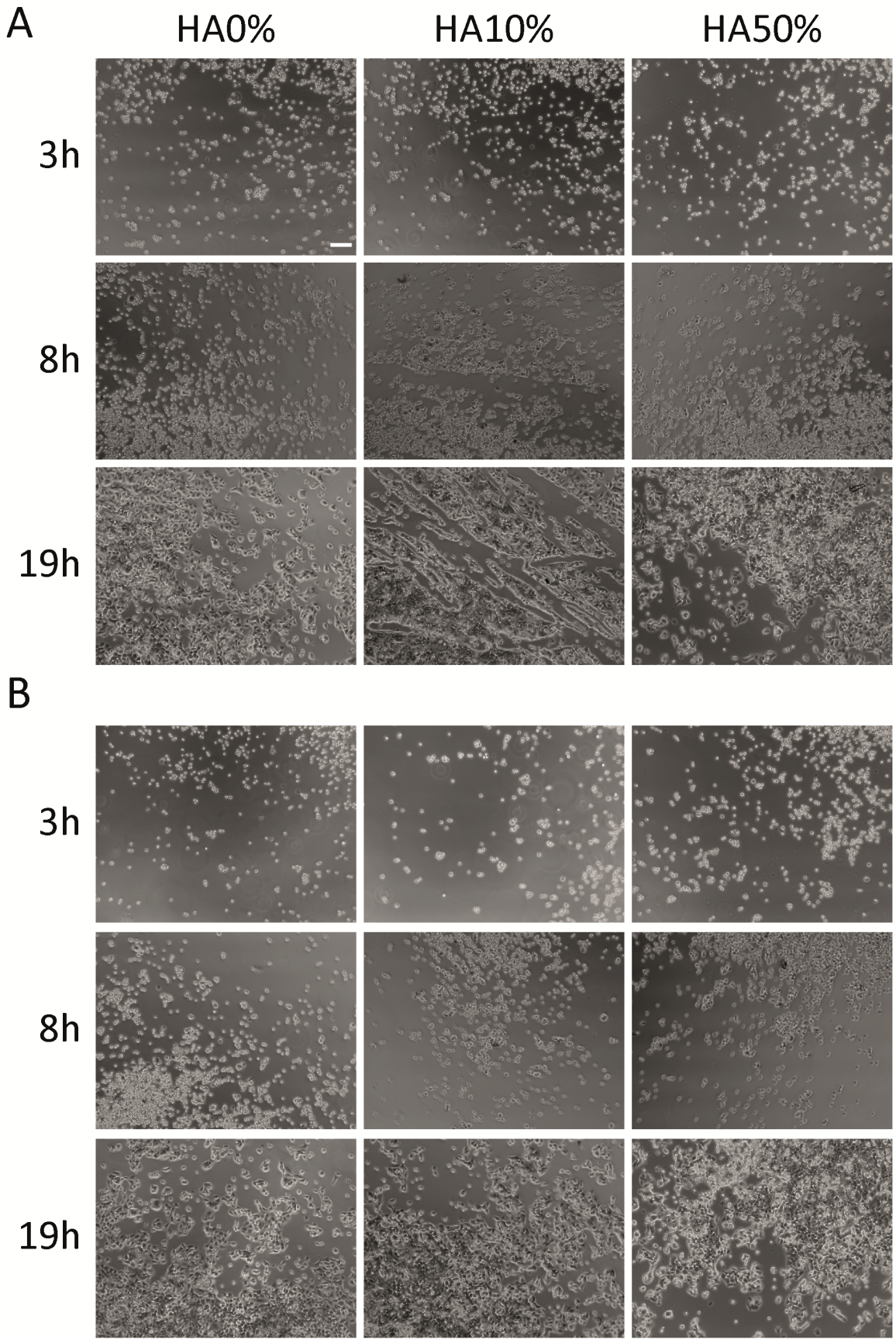

Figure 49: Wider overview of HaCaT cell adhesion on PEG2000/PEG3000azide passivated, HA immobilized glass surfaces and functionalized gold-nanostructured glass surfaces.

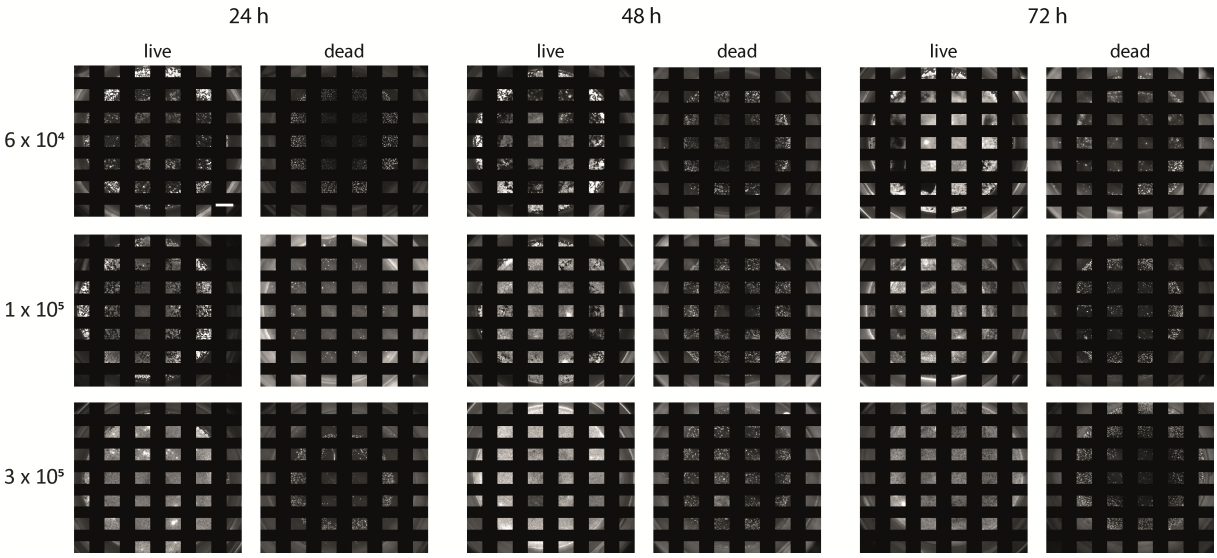

Figure 50: Membrane cell coverage upon seeding different numbers of HaCaT cells and cultivation for 24/48/72 h. Membranes were collagen I-coated and initial HaCaT cell seeding number per membrane was 6 x 104, 105 and 3 x 105, respectively. Living cells were visualized by calcein-AM (live) and dead cells by Ethidium-Homodimer-1 (dead) to determine membrane cultivation after 24, 48 and 72 h in DMEM supplemented with 10 % (v/v) FBS. Full membrane area was recorded at 10x magnification with a tiles shift of 100%. Membrane boundaries are indicated in grey. Representative images of 2 replicates. Scale bar: 1000 µm.

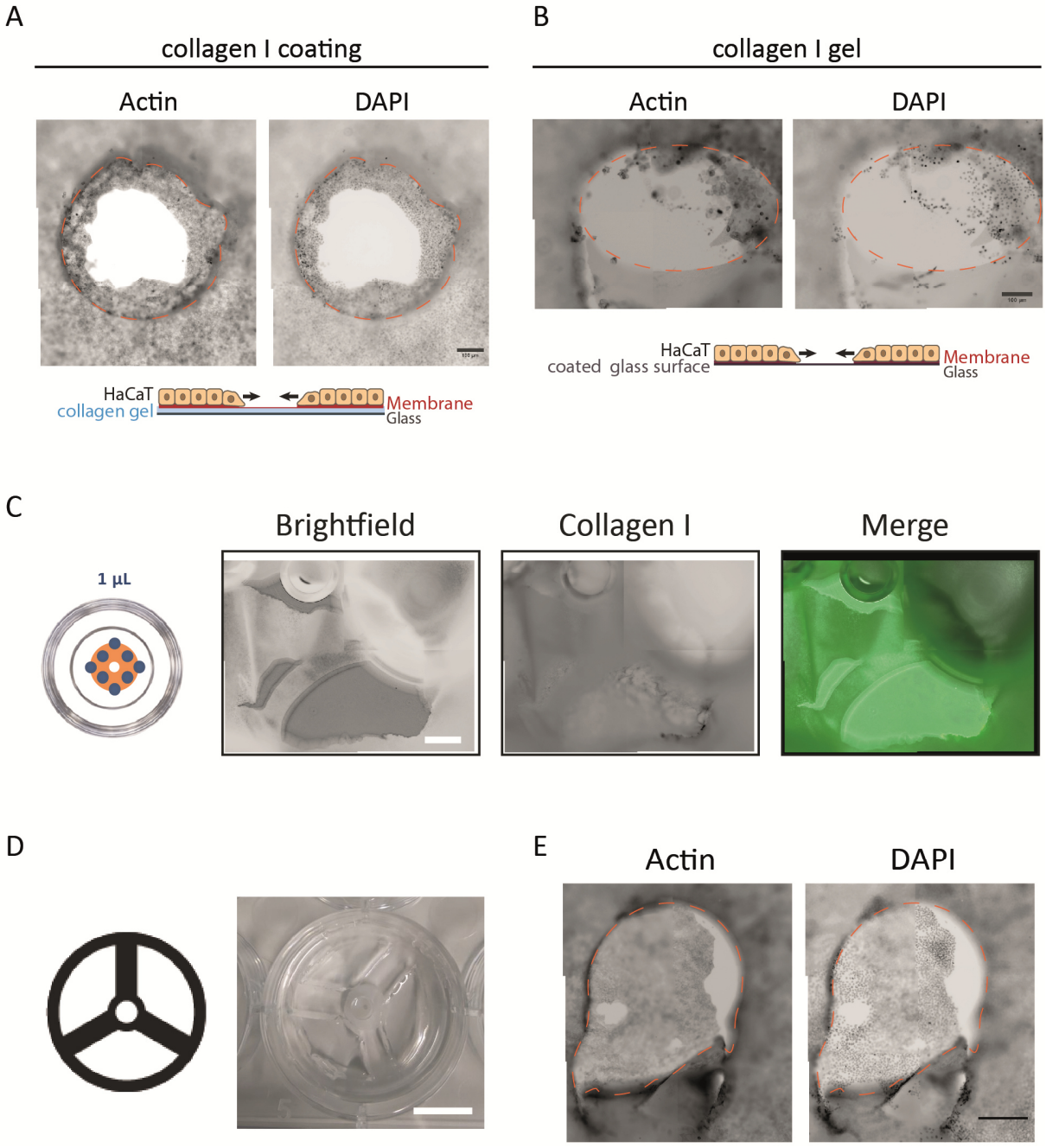

Figure 51: 2D epidermal models with round wound site (2 mm biopsy punch). (A), (B) Membranes with cultivated, full confluent HaCaT monolayers were punched in the middle and placed on collagen I -coated surfaces (A) and collagen I gels (B). surfaces. After 4 days cells were PFA-fixed and nuclei were visualized with DAPI and actin by phalloidin. Dotted line indicates round wound site generated by a 2 mm biopsy punch; Scale bar: 100 µm. (C) Collagen I glue localizes in wound site. Immunostaining of polymerized collagen I glue under wounded (cut) membranes. Membrane halves were fixated on activated glass surfaces using unpolymerized collagen I ("collagen I glue"). Drops of collagen I glue of indicated volumes were placed in different patterns on surfaces before membranes are placed directly on top of the drops of pushed (indicated by arrow) inside them. Immunostaining upon collagen I polymerization against collagen I (green) reveals its localization under and around the membranes (grey); scale bar: 500 µm. (D) PDMS-based molds to mechanically fix punched HaCaT carrying membranes on cell culture dishes. Left: top view of two PDMS mold design; right: respective picture; scale bar: 1 cm. (E) Membranes with cultivated, full confluent HaCaT monolayers were punched in the middle and placed on collagen I -coated surfaces. After 4 days cells were PFA-fixed and nuclei were visualized with DAPI and actin by phalloidin. Dotted line indicates round wound site generated by a 2 mm biopsy punch; scale bar: 500 µm.

B. Tables

Table 25: Mean, SD and N of replicates of non-normalized relative proliferation on collagen I or fibronectin upon HA administration.

ECM	HA [kDa]	conc [µg/mL]	Mean	SD	N
Collagen I	-HA	-	0.627	0.119	12
	5	500	0.777	0.050	6
	1800	5	0.762	0.078	3
Fibronectin	-HA	-	0.603	0.111	9
	5	500	0.664	0.085	6
	1800	5	0.811	0.164	6

Table 26: Mean, SD and N of replicates of non-normalized relative proliferation on collagen I or fibronectin upon HA administration.

HA [kDa]	conc [µg/mL]	low density			high density		
		Mean	SD	N	Mean	SD	N
5	0	0.487	0.162	6	0.534	0.285	6
	5	0.591	0.181	6	0.555	0.298	6
	50	0.667	0.211	6	0.526	0.328	6
	500	0.730	0.253	6	0.601	0.309	6
	1000	0.803	0.196	6	0.547	0.203	6
60	0	0.509	0.273	6	0.624	0.210	6
	5	0.647	0.156	6	0.478	0.236	6
	50	0.623	0.212	6	0.464	0.225	6
	500	0.753	0.168	6	0.710	0.020	3
	1000	0.653	0.242	6	0.554	0.105	6
700	0	0.496	0.159	6	0.561	0.230	6
	5	0.650	0.212	6	0.547	0.247	6
	50	0.705	0.228	6	0.581	0.285	6
	500	0.717	0.261	6	0.630	0.251	6
	1000	0.694	0.298	6	0.457	0.174	6
1800	0	0.520	0.244	3	0.461	0.287	6
	5	0.621	0.139	3	0.468	0.302	6
	50	0.665	0.123	3	0.479	0.293	6
	500	0.878	0.065	3	0.735	0.021	3
	1000	0.813	0.211	3	0.548	0.235	6

Table 27: Commercially available cell culture inserts with a pore size of 0.4 µm.

Name	Company	order number	Diameter [mm]	Material
Millicell Hanging Cell Culture Insert	Merck	MCHT12H48	12	Polyethylene Terephthalate (PET)
Millicell Cell Culture Insert	Merck	PIHP01250	12	Polycarbonate
Cell Culture Inserts	Nunc	140620	7.7	Polycarbonate
Millicell Cell Culture Insert	EMD Millipore	PICM01250	12	Polytetrafluorethylen

Bibliography

Aflak, N. *et al.* (2019) 'Sustainable Construction of Heterocyclic 1,2,3-Triazoles by Strict Click [3+2] Cycloaddition Reactions Between Azides and Alkynes on Copper/Carbon in Water', *Frontiers in Chemistry*. Frontiers Media S.A., 7(FEB), p. 81. doi: 10.3389/fchem.2019.00081.

Alhajj, M., Bansal, P. and Goyal, A. (2020) *Physiology, Granulation Tissue*, *StatPearls*. StatPearls Publishing. Available at: http://www.ncbi.nlm.nih.gov/pubmed/32119289 (Accessed: 29 May 2020).

Anderegg, U., Simon, J. C. and Averbeck, M. (2014) 'More than just a filler - the role of hyaluronan for skin homeostasis', *Experimental Dermatology*, 23(5), pp. 295–303. doi: 10.1111/exd.12370.

Arganda-Carreras, I. *et al.* (2017) 'Trainable Weka Segmentation: a machine learning tool for microscopy pixel classification', *Bioinformatics*. Edited by R. Murphy. Oxford University Press, 33(15), pp. 2424–2426. doi: 10.1093/bioinformatics/btx180.

Arnold, M. *et al.* (2004) 'Activation of integrin function by nanopatterned adhesive interfaces', *ChemPhysChem*. WILEY-VCH Verlag, 5(3), pp. 383–388. doi: 10.1002/cphc.200301014.

Aumailley, M. *et al.* (1991) 'Arg-Gly-Asp constrained within cyclic pentapoptides Strong and selective inhibitors of cell adhesion to vitronectin and laminin fragment P1', *FEBS Letters*, 291(1), pp. 50–54. doi: 10.1016/0014-5793(91)81101-D.

Aya, K. L. and Stern, R. (2014) 'Hyaluronan in wound healing: Rediscovering a major player', *Wound Repair and Regeneration*. Blackwell Publishing Inc., 22(5), pp. 579–593. doi: 10.1111/wrr.12214.

Aydin, D. *et al.* (2010) 'Polymeric substrates with tunable elasticity and nanoscopically controlled biomolecule presentation', *Langmuir*, 26(19), pp. 15472–15480. doi: 10.1021/la103065x.

Bae, J. S. *et al.* (2002) 'Big-H3 Supports Keratinocyte Adhesion, Migration, and Proliferation Through A3B1 Integrin', *Biochemical and Biophysical Research Communications*, 294(5), pp. 940–948. doi: 10.1016/S0006-291X(02)00576-4.

Bagby, T. R. *et al.* (2012) 'Impact of molecular weight on lymphatic drainage of a biopolymer-based imaging agent', *Pharmaceutics*. Multidisciplinary Digital Publishing Institute (MDPI), 4(2), pp. 276–295. doi: 10.3390/pharmaceutics4020276.

Balazs, E. A. *et al.* (1967) 'Hyaluronic acid in synovial fluid. I. Molecular parameters of hyaluronic acid in normal and arthritic human fluids', *Arthritis & Rheumatism*, 10(4), pp. 357–376. doi: 10.1002/art.1780100407.

Blümmel, J. *et al.* (2007) 'Protein repellent properties of covalently attached PEG coatings on nanostructured SiO2-based interfaces', *Biomaterials*, 28(32), pp. 4739–4747. doi: 10.1016/j.biomaterials.2007.07.038.

Böhm, H. (2008) *Micromechanical Properties and Structure ofthe Pericellular Coat of Living Cells Modulatedby Nanopatterned Substrates*. Heidelberg University.

Bono, P. *et al.* (2001) 'Layilin, a Novel Integral Membrane Protein, Is a Hyaluronan Receptor', *Molecular Biology of the Cell*. Edited by J. S. Brugge. American Society for Cell Biology, 12(4), pp. 891–900. doi: 10.1091/mbc.12.4.891.

Botta, A. *et al.* (2012) 'Confluence switch signaling regulates ECM composition and the plasmin proteolytic cascade in keratinocytes', *Journal of Cell Science*. The Company of Biologists Ltd, 125(18), pp. 4241–4252. doi: 10.1242/jcs.096289.

Boukamp, P. *et al.* (1988) 'Normal Keratinization in a Spontaneously Immortalized Aneuploid Human Keratinocyte Cell Line', *Journal of Cell Biology*. The Rockefeller University Press, 106(March), pp. 761–771. doi: 10.1083/jcb.106.3.761.

Bourguignon, L. Y. W. *et al.* (2013) 'Selective matrix (hyaluronan) interaction with CD44 and RhoGTPase signaling promotes keratinocyte functions and overcomes age-related epidermal dysfunction', *Journal of*

Dermatological Science, 72(1), pp. 32–44. doi: 10.1016/j.jdermsci.2013.05.003.

Brice, J. C. (1985) 'Crystals for quartz resonators', *Reviews of Modern Physics*. American Physical Society, 57(1), pp. 105–146. doi: 10.1103/RevModPhys.57.105.

Brown, C. *et al.* (1991) 'Vitronectin: Effects on keratinocyte motility and inhibition of collagen-induced motility', *Journal of Investigative Dermatology*. J Invest Dermatol, 96(5), pp. 724–728. doi: 10.1111/1523-1747.ep12470960.

Brown, R. L. *et al.* (2011) 'CD44 splice isoform switching in human and mouse epithelium is essential for epithelial-mesenchymal transition and breast cancer progression.', *The Journal of clinical investigation*. American Society for Clinical Investigation, 121(3), pp. 1064–74. doi: 10.1172/JCI44540.

Brown, T. J., Alcorn, D. and Fraser, J. R. E. (1999) 'Absorption of Hyaluronan Applied to the Surface of Intact Skin', *Journal of Investigative Dermatology*. Blackwell Publishing Inc., 113(5), pp. 740–746. doi: 10.1046/j.1523-1747.1999.00745.x.

Camenisch, T. D. *et al.* (2000) 'Disruption of hyaluronan synthase-2 abrogates normal cardiac morphogenesis and hyaluronan-mediated transformation of epithelium to mesenchyme', *Journal of Clinical Investigation*. The American Society for Clinical Investigation, 106(3), pp. 349–360. doi: 10.1172/JCI10272.

Cavalcanti-Adam, E. A. *et al.* (2006) 'Lateral spacing of integrin ligands influences cell spreading and focal adhesion assembly', *European Journal of Cell Biology*. Elsevier GmbH, 85(3–4), pp. 219–224. doi: 10.1016/j.ejcb.2005.09.011.

Cavalcanti-Adam, E. A. *et al.* (2007) 'Cell Spreading and Focal Adhesion Dynamics Are Regulated by Spacing of Integrin Ligands', *Biophysical Journal*. Cell Press, 92(8), pp. 2964–2974. doi: 10.1529/BIOPHYSJ.106.089730.

Chopra, A. *et al.* (2014) 'Augmentation of integrin-mediated mechanotransduction by hyaluronic acid', *Biomaterials*. NIH Public Access, 35(1), pp. 71–82. doi: 10.1016/j.biomaterials.2013.09.066.

Clark, R. A. F. *et al.* (1982) 'Fibronectin and fibrin provide a provisional matrix for epidermal cell migration during wound reepithelialization', *Journal of Investigative Dermatology*. Elsevier, 79(5), pp. 264–269. doi: 10.1111/1523-1747.ep12500075.

Cowman, M. K. *et al.* (2005) 'Extended, Relaxed, and Condensed Conformations of Hyaluronan Observed by Atomic Force Microscopy', *Biophysical Journal*. Cell Press, 88(1), pp. 590–602. doi: 10.1529/BIOPHYSJ.104.049361.

Cowman, M. K. *et al.* (2015) 'The Content and Size of Hyaluronan in Biological Fluids and Tissues.', *Frontiers in immunology*. Frontiers Media SA, 6, p. 261. doi: 10.3389/fimmu.2015.00261.

Culty, M., Nguyen, H. A. and Underhill, C. B. (1992) 'The hyaluronan receptor (CD44) participates in the uptake and degradation of hyaluronan', *Journal of Cell Biology*. Rockefeller University Press, 116(4), pp. 1055–1062. doi: 10.1083/jcb.116.4.1055.

D'Agostino, A. *et al.* (2015) 'In vitro analysis of the effects on wound healing of high- and low-molecular weight chains of hyaluronan and their hybrid H-HA/L-HA complexes', *BMC Cell Biology*, 16(1), p. 19. doi: 10.1186/s12860-015-0064-6.

D'Agostino, A. *et al.* (2017) 'Is molecular size a discriminating factor in hyaluronan interaction with human cells?', *Carbohydrate Polymers*. Elsevier Ltd., 157, pp. 21–30. doi: 10.1016/j.carbpol.2016.07.125.

Dahl,', L. B. *et al.* (1985) 'Concentration and molecular weight of sodium hyaluronate in synovial fluid from patients with rheumatoid arthritis and other arthropathies', *Annals of the Rheumatic Diseases*, 44, pp. 817–822. doi: 10.1136/ard.44.12.817.

Damiati, L. *et al.* (2018) 'Impact of surface topography and coating on osteogenesis and bacterial attachment on titanium implants.', *Journal of tissue engineering*. SAGE Publications Ltd, 9, p. 2041731418790694. doi: 10.1177/2041731418790694.

Damodarasamy, M. *et al.* (2014) 'Hyaluronan enhances wound repair and increases collagen III in aged dermal wounds', *Wound Repair and Regeneration*. Blackwell Publishing Inc., 22(4), pp. 521–526. doi: 10.1111/wrr.12192.

Dawson, R. A. *et al.* (1996) 'Influence of extracellular matrix proteins on human keratinocyte attachment, proliferation and transfer to a dermal wound model', *Burns*. Elsevier Ltd, 22(2), pp. 93–100. doi: 10.1016/0305-4179(95)00092-5.

Day, A. J. and Prestwich, G. D. (2002) 'Hyaluronan-binding proteins: Tying up the giant', *Journal of Biological Chemistry*. American Society for Biochemistry and Molecular Biology, pp. 4585–4588. doi: 10.1074/jbc.R100036200.

Devanand, K. and Selser, J. C. (1991) 'Asymptotic Behavior and Long-Range Interactions in Aqueous Solutions of Poly(ethylene oxide)', *Macromolecules*. American Chemical Society, 24(22), pp. 5943–5947. doi: 10.1021/ma00022a008.

Dixon, M. C. (2008) 'Quartz crystal microbalance with dissipation monitoring: Enabling real-time characterization of biological materials and their interactions', *Journal of Biomolecular Techniques*. The Association of Biomolecular Resource Facilities, pp. 151–158.

Dunphy, J. E. and Udupa, K. N. (1955) 'Chemical and histochemical sequences in the normal healing of wounds', *The New England journal of medicine*. Massachusetts Medical Society, 253(20), pp. 847–851. doi: 10.1056/NEJM195511172532002.

Frantz, C., Stewart, K. M. and Weaver, V. M. (2010) 'The extracellular matrix at a glance', *Journal of Cell Science*. The Company of Biologists Ltd, pp. 4195–4200. doi: 10.1242/jcs.023820.

Frenkel, J. S. (2014) 'The role of hyaluronan in wound healing', *International Wound Journal*, 11(2), pp. 159–163. doi: 10.1111/j.1742-481X.2012.01057.x.

Gao, S. *et al.* (2018) 'Effects of high-concentration salt solutions and pH on swelling behavior of physically and chemically cross-linked hybrid hydrophobic association hydrogels with good mechanical strength', *Soft Materials*. Taylor and Francis Inc., 16(4), pp. 249–264. doi: 10.1080/1539445X.2018.1489844.

Garland, S. P. *et al.* (2014) 'A Cell Culture Substrate with Biologically Relevant Size-Scale Topography and Compliance of the Basement Membrane'. doi: 10.1021/la403590v.

Gerdin, B. and Hällgren, R. (1997) 'Dynamic role of hyaluronan (HYA) in connective tissue activation and inflammation', *Journal of Internal Medicine*. Blackwell Publishing Ltd, 242(1), pp. 49–55. doi: 10.1046/j.1365-2796.1997.00173.x.

Ghatak, S. *et al.* (2015) 'Roles of Proteoglycans and Glycosaminoglycans in Wound Healing and Fibrosis', *International Journal of Cell Biology*. Hindawi, 2015, p. 834893. doi: 10.1155/2015/834893.

Ghazi, K. *et al.* (2012) 'Hyaluronan Fragments Improve Wound Healing on In Vitro Cutaneous Model through P2X7 Purinoreceptor Basal Activation: Role of Molecular Weight', *PLoS ONE*. Edited by C. Egles. Public Library of Science, 7(11), p. e48351. doi: 10.1371/journal.pone.0048351.

Gonzalez, A. C. D. O. *et al.* (2016) 'Wound healing - A literature review', *Anais Brasileiros de Dermatologia*. Sociedade Brasileira de Dermatologia, pp. 614–620. doi: 10.1590/abd1806-4841.20164741.

Görmar, F. E. *et al.* (1993) *Mechanical Stimulation Enhances Human Keratinocyte Differentiation in Culture: Induction of Cytokeratin 9 Synthesis*.

Grinnell, F. (1992) 'Wound repair, keratinocyte activation and integrin modulation', *Journal of Cell Science*, 101(1), pp. 1–5.

Gu, H. *et al.* (2010) 'HA modulation of epidermal morphogenesis in an organotypic keratinocyte-fibroblast co-culture model', *Experimental Dermatology*. Exp Dermatol. doi: 10.1111/j.1600-0625.2009.01052.x.

Guo, M., Toda, K. I. and Grinnell, F. (1990) 'Activation of human keratinocyte migration on type I collagen and fibronectin', *Journal of Cell Science*, 96(2), pp. 197–205.

Harada, H. and Takahashi, M. (2007) 'CD44-dependent intracellular and extracellular catabolism of hyaluronic acid by hyaluronidase-1 and -2', *Journal of Biological Chemistry*. American Society for Biochemistry and Molecular Biology, 282(8), pp. 5597–5607. doi: 10.1074/jbc.M608358200.

Harder, P. *et al.* (1998) 'Molecular conformation in oligo(ethylene glycol)-terminated self-assembled monolayers on gold and silver surfaces determines their ability to resist protein adsorption', *Journal of Physical Chemistry B*. American Chemical Society , 102(2), pp. 426–436. doi: 10.1021/jp972635z.

Hardingham, T. (1981) 'Proteoglycans: their structure, interactions and molecular organization in cartilage.', *Biochemical Society transactions*. Biochem Soc Trans, 9(6), pp. 489–497. doi: 10.1042/bst0090489.

Hynes, R. O. and Naba, A. (2012) 'Overview of the matrisome-An inventory of extracellular matrix constituents and functions', *Cold Spring Harbor Perspectives in Biology*. Cold Spring Harbor Laboratory Press, 4(1). doi: 10.1101/cshperspect.a004903.

Iorio, V., Troughton, L. D. and Hamill, K. J. (2015) 'Laminins: Roles and Utility in Wound Repair', *Advances in Wound Care*. Mary Ann Liebert, Inc., 4(4), pp. 250–263. doi: 10.1089/wound.2014.0533.

Itano, N. *et al.* (1999) 'Three isoforms of mammalian hyaluronan synthases have distinct enzymatic properties', *Journal of Biological Chemistry*. American Society for Biochemistry and Molecular Biology, 274(35), pp. 25085–25092. doi: 10.1074/jbc.274.35.25085.

Janata, J. (1989) *Principles of Chemical Sensors*, *New York: Plenum*.

Järveläinen, H. *et al.* (2009) 'Extracellular matrix molecules: Potential targets in pharmacotherapy', *Pharmacological Reviews*. Pharmacol Rev, pp. 198–223. doi: 10.1124/pr.109.001289.

Johnson, L. A. *et al.* (2007) 'Inflammation-induced uptake and degradation of the lymphatic endothelial hyaluronan receptor LYVE-1', *Journal of Biological Chemistry*. American Society for Biochemistry and Molecular Biology, 282(46), pp. 33671–33680. doi: 10.1074/jbc.M702889200.

Kapp, T. G. *et al.* (2013) 'Integrin modulators: a patent review', *Expert Opinion on Therapeutic Patents*. Informa UK, Ltd., 23(10), pp. 1273–1295. doi: 10.1517/13543776.2013.818133.

Kapp, T. G. *et al.* (2017) 'A Comprehensive Evaluation of the Activity and Selectivity Profile of Ligands for RGD-binding Integrins', *Scientific Reports*. Nature Publishing Group, 7, p. 39805. doi: 10.1038/srep39805.

Karousou, E. *et al.* (2010) 'The activity of hyaluronan synthase 2 is regulated by dimerization and ubiquitination', *Journal of Biological Chemistry*. J Biol Chem, 285(31), pp. 23647–23654. doi: 10.1074/jbc.M110.127050.

Karvinen, S. *et al.* (2003) 'Keratinocyte Growth Factor Stimulates Migration and Hyaluronan Synthesis in the Epidermis by Activation of Keratinocyte Hyaluronan Synthases 2 and 3*', *Published JBC Papers in Press*. doi: 10.1074/jbc.M310445200.

Kästle, G. *et al.* (2003) 'Micellar Nanoreactors - Preparation and Characterization of Hexagonally Ordered Arrays of Metallic Nanodots', *Advanced Functional Materials*. John Wiley & Sons, Ltd, 13(11), pp. 853–861. doi: 10.1002/adfm.200304332.

Kawaguchi, S. *et al.* (1997) 'Aqueous solution properties of oligo- and poly(ethylene oxide) by static light scattering and intrinsic viscosity', *Polymer*. Elsevier BV, 38(12), pp. 2885–2891. doi: 10.1016/S0032-3861(96)00859-2.

Kennedy, J. F. *et al.* (2000) *Hyaluronan: Proceedings of an International Meeting*. Volume 1. Woodhead Publishing.

Kim, J. E. *et al.* (2000) 'Identification of motifs for cell adhesion within the repeated domains of transforming growth factor-β-induced gene, βig-h3', *Journal of Biological Chemistry*. American Society for Biochemistry and Molecular Biology, 275(40), pp. 30907–30915. doi: 10.1074/jbc.M002752200.

Kjeuin, L. and Lindahl, U. (1991) *Proteoglycans: Structures and Interactions*, *Annu. Rev. Biochem*. Available at: www.annualreviews.org.

Koistinen, V. *et al.* (2017) 'EMT induced by EGF and wounding activates hyaluronan synthesis machinery and EV shedding in rat primary mesothelial cells', *Matrix Biology*, 63, pp. 38–54. doi: 10.1016/j.matbio.2016.12.007.

Krieg, T. and Aumailley, M. (2011) 'The extracellular matrix of the dermis: flexible structures with dynamic functions', *Experimental Dermatology*. John Wiley & Sons, Ltd, 20(8), pp. 689–695. doi: 10.1111/j.1600-0625.2011.01313.x.

Krupkova, O. *et al.* (2020) 'Expression and activity of hyaluronidases HYAL-1, HYAL-2 and HYAL-3 in the human intervertebral disc', *European Spine Journal*. Springer, 29(3), pp. 605–615. doi: 10.1007/s00586-019-06227-3.

Kuschel, C. *et al.* (2006) 'Cell adhesion profiling using extracellular matrix protein microarrays', *BioTechniques*. Future Science Ltd London, UK , 40(4), pp. 523–531. doi: 10.2144/000112134.

Lambrichta, L. *et al.* (2014) 'The type and composition of alginate and hyaluronic-based hydrogels influence the viability of stem cells of the apical papilla', *Dental Materials*. Elsevier Inc., 30(12), pp. e349–e361. doi: 10.1016/j.dental.2014.08.369.

Larjava, H., Häkkinen, L. and Koivisto, L. (2013) 'Re-Epithelialization of Wounds', *Oral Wound Healing: Cell Biology and Clinical Management*, 24, pp. 81–123. doi: 10.1002/9781118704509.ch5.

Lee, H. *et al.* (2008) 'Synthesis, characterization, and in vivo diagnostic applications of hyaluronic acid immobilized gold nanoprobes', *Biomaterials*, 29(35), pp. 4709–4718. doi: 10.1016/j.biomaterials.2008.08.038.

Lee, H. *et al.* (2009) 'A coarse-grained model for polyethylene oxide and polyethylene glycol: Conformation and hydrodynamics', *Journal of Physical Chemistry B*. American Chemical Society, 113(40), pp. 13186–13194. doi: 10.1021/jp9058966.

Lenormand, H., Amar-Bacoup, F. and Vincent, J. C. (2011) 'PH effects on the hyaluronan hydrolysis catalysed by hyaluronidase in the presence of proteins. Part III. The electrostatic non-specific hyaluronan-hyaluronidase complex', *Carbohydrate Polymers*. Elsevier, 86(4), pp. 1491–1500. doi: 10.1016/j.carbpol.2011.06.044.

Lesley, J. *et al.* (2000) 'Hyaluronan binding by cell surface CD44', *Journal of Biological Chemistry*, 275(35), pp. 26967–26975. doi: 10.1074/jbc.M002527200.

Li, J., Han, D. and Zhao, Y. P. (2014) 'Kinetic behaviour of the cells touching substrate: The interfacial stiffness guides cell spreading', *Scientific Reports*. Nature Publishing Group, 4(1), pp. 1–11. doi: 10.1038/srep03910.

Li, L. and Zhang, Z. (2016) 'Development and applications of the copper-catalyzed azide-alkyne cycloaddition (CuAAC) as a bioorthogonal reaction', *Molecules*. MDPI AG. doi: 10.3390/molecules21101393.

Lohmüller, T. *et al.* (2011) 'Nanopatterning by block copolymer micelle nanolithography and bioinspired applications', *Biointerphases*, 6(1), pp. MR1–MR12. doi: 10.1116/1.3536839.

Longmate, W. M. and DiPersio, C. M. (2014) 'Integrin Regulation of Epidermal Functions in Wounds', *Advances in Wound Care*. Mary Ann Liebert, Inc., 3(3), pp. 229–246. doi: 10.1089/wound.2013.0516.

Love, J. C. *et al.* (2005) *Self-assembled monolayers of thiolates on metals as a form of nanotechnology*, *Chemical Reviews*. doi: 10.1021/cr0300789.

Malaisse, J. *et al.* (2016) 'Hyaluronan does not regulate human epidermal keratinocyte proliferation and differentiation', *Journal of Biological Chemistry*. American Society for Biochemistry and Molecular Biology, 291(12), pp. 6347–6358. doi: 10.1074/jbc.M115.661348.

Martin, P. (1997) 'Wound healing - Aiming for perfect skin regeneration', *Science*. American Association for the Advancement of Science, 276(5309), pp. 75–81. doi: 10.1126/science.276.5309.75.

Mas-Moruno, C. *et al.* (2016) 'αvβ3- or α5β1-Integrin-Selective Peptidomimetics for Surface Coating', *Angewandte Chemie - International Edition*, 55(25), pp. 7048–7067. doi: 10.1002/anie.201509782.

Mehne, J. *et al.* (2008) 'Characterisation of morphology of self-assembled PEG monolayers: A comparison of mixed and pure coatings optimised for biosensor applications', *Analytical and Bioanalytical Chemistry*. Springer, 391(5), pp. 1783–1791. doi: 10.1007/s00216-008-2066-0.

Mendichi, R., Šoltés, L. and Giacometti Schieroni, A. (2003) 'Evaluation of radius of gyration and intrinsic viscosity molar mass dependence and stiffness of hyaluronan', *Biomacromolecules*. American Chemical Society , 4(6), pp. 1805–1810. doi: 10.1021/bm0342178.

Michopoulou, A. *et al.* (2020) 'A novel mechanism in wound healing: Laminin 332 drives MMP9/14 activity by recruiting syndecan-1 and CD44', *Matrix Biology*. Elsevier. doi: 10.1016/j.matbio.2020.06.004.

Minsky, B. B., Antoni, C. H. and Boehm, H. (2016) 'Controlled Immobilization Strategies to Probe Short Hyaluronan-Protein Interactions', *Scientific Reports*. Nature Publishing Group, 6(1), p. 21608. doi: 10.1038/srep21608.

Morasso, M. I. and Tomic-Canic, M. (2005) 'Epidermal stem cells: the cradle of epidermal determination, differentiation and wound healing', *Biology of the Cell*. Wiley, 97(3), pp. 173–183. doi: 10.1042/bc20040098.

Mueller, R. M. and White, W. (1968) 'Direct gravimetric calibration of a quartz crystal microbalance', *Review of Scientific Instruments*. American Institute of PhysicsAIP, 39(3), pp. 291–295. doi: 10.1063/1.1683352.

Niethammer, P. (2016) 'The early wound signals', *Current Opinion in Genetics and Development*. Elsevier Ltd, pp. 17–22. doi: 10.1016/j.gde.2016.05.001.

Nyman, E. *et al.* (2013) 'Hyaluronic acid, an important factor in the wound healing properties of amniotic fluid: *In vitro* studies of re-epithelialisation in human skin wounds', *Journal of Plastic Surgery and Hand Surgery*. Taylor & Francis, 47(2), pp. 89–92. doi: 10.3109/2000656X.2012.733169.

O'Toole, E. A. *et al.* (1997) 'Laminin-5 Inhibits Human Keratinocyte Migration', *Experimental Cell Research*. Academic Press, 233(2), pp. 330–339. doi: 10.1006/EXCR.1997.3586.

Oelmeier, S. A., Dismer, F. and Hubbuch, J. (2012) 'Molecular dynamics simulations on aqueous two-phase systems - Single PEG-molecules in solution', *BMC Biophysics*. Springer Nature, 5(1), p. 14. doi: 10.1186/2046-1682-5-14.

Omelyanenko, N. P., Ilyich, S. L. and Pavlovich, M. S. (2016) 'Connective Tissue: Histophysiology, Biochemistry, Molecular Biology', in. CRC Press, p. 303.

Oria, R. *et al.* (2017) 'Force loading explains spatial sensing of ligands by cells', *Nature*. Nature Publishing Group, 552(7684), pp. 219–224. doi: 10.1038/nature24662.

Park, S. *et al.* (2017) 'Tissue-scale coordination of cellular behaviour promotes epidermal wound repair in live mice', *Nature Cell Biology*. Nature Research, 19(2), pp. 155–163. doi: 10.1038/ncb3472.

Pasonen-Seppänen, S. *et al.* (2003) 'EGF upregulates, whereas TGF-β downregulates, the hyaluronan synthases Has2 and Has3 in organotypic keratinocyte cultures: Correlations with epidermal proliferation and differentiation', *Journal of Investigative Dermatology*, 120(6), pp. 1038–1044. doi: 10.1046/j.1523-1747.2003.12249.x.

Pastar, I. and Stojadinovic, O. (2010) '<Title/>', *Molecular Medicine*. The Feinstein Institute for Medical Research, 16(3–4), p. 1. doi: 10.2119/molmed.2009.00149.

Perrais, M. *et al.* (2007) 'E-cadherin homophilic ligation inhibits cell growth and epidermal growth factor receptor signaling independently of other cell interactions', *Molecular Biology of the Cell*. American Society for Cell Biology, 18(6), pp. 2013–2025. doi: 10.1091/mbc.E06-04-0348.

Petersen, M. J. *et al.* (1990) 'Enhanced synthesis of collagenase by human keratinocytes cultured on type I or type IV collagen', *Journal of Investigative Dermatology*. Elsevier, 94(3), pp. 341–346. doi: 10.1111/1523-1747.ep12874471.

Ponce, L. *et al.* (2017) 'Isolation and cultivation of primary keratinocytes from piglet skin for compartmentalized co-culture with dorsal root ganglion neurons', *Journal of Cellular Biotechnology*. IOS Press,

2(2), pp. 93–115. doi: 10.3233/JCB-15030.

Posa, F. *et al.* (2019) 'Surface Co-Presentation of BMP-2 and Integrin Selective Ligands at the Nanoscale Favors β1 Integrin Adhesion'. ChemRxiv. doi: 10.26434/CHEMRXIV.8209349.V1.

Prevo, R. *et al.* (2001) 'Mouse LYVE-1 Is an Endocytic Receptor for Hyaluronan in Lymphatic Endothelium', *Journal of Biological Chemistry*. American Society for Biochemistry and Molecular Biology, 276(22), pp. 19420–19430. doi: 10.1074/jbc.M011004200.

Quent, V. M. C. *et al.* (2010) 'Discrepancies between metabolic activity and DNA content as tool to assess cell proliferation in cancer research', *Journal of Cellular and Molecular Medicine*. Wiley-Blackwell, 14(4), pp. 1003–1013. doi: 10.1111/j.1582-4934.2010.01013.x.

Rechenmacher, F. *et al.* (2013) 'Functionalizing ??v??3- or ??5??1-selective integrin antagonists for surface coating: A method to discriminate integrin subtypes in vitro', *Angewandte Chemie - International Edition*. WILEY-VCH Verlag, 52(5), pp. 1572–1575. doi: 10.1002/anie.201206370.

Reheman, A. *et al.* (2005) 'Vitronectin stabilizes thrombi and vessel occlusion but plays a dual role in platelet aggregation', *Journal of Thrombosis and Haemostasis*. J Thromb Haemost, 3(5), pp. 875–883. doi: 10.1111/j.1538-7836.2005.01217.x.

Rittié, L. (2016) 'Cellular mechanisms of skin repair in humans and other mammals', *Journal of Cell Communication and Signaling*. Springer Netherlands, pp. 103–120. doi: 10.1007/s12079-016-0330-1.

Rousselle, P., Montmasson, M. and Garnier, C. (2019) 'Extracellular matrix contribution to skin wound re-epithelialization', *Matrix Biology*, 75–76, pp. 12–26. doi: 10.1016/j.matbio.2018.01.002.

Di Russo, J. *et al.* (2019) 'NTA-Co3+-His6 versus NTA-Ni2+-His6 mediated E-Cadherin surface immobilization enhances cellular traction', *Biomaterials*. Elsevier, 192, pp. 171–178. doi: 10.1016/J.BIOMATERIALS.2018.10.042.

Rüther, L. *et al.* (2017) 'Hyaluronan as a key for accelerated wound healing in human 3D full thickness skin models', *Hautarzt*. Springer Verlag, pp. 987–993. doi: 10.1007/s00105-017-4054-9.

Safferling, K. *et al.* (2013) 'Wound healing revised: A novel reepithelialization mechanism revealed by in vitro and in silico models', *Journal of Cell Biology*. The Rockefeller University Press, 203(4), pp. 691–709. doi: 10.1083/jcb.201212020.

Sauerbrey, G. (1959) 'Verwendung von Schwingquarzen zur Wägung dünner Schichten und zur Mikrowägung', *Zeitschrift für Physik*. Springer, 155(2), pp. 206–222. doi: 10.1007/BF01337937.

Sauter, A. *et al.* (2013) 'Effective polyethylene glycol passivation for the inhibition of surface interactions of peripheral blood mononuclear cells and platelets', *Biointerphases*. Springer Verlag, 8(1), pp. 1–12. doi: 10.1186/1559-4106-8-14.

Schanté, C. E. *et al.* (2011) 'Chemical modifications of hyaluronic acid for the synthesis of derivatives for a broad range of biomedical applications', *Carbohydrate Polymers*. Elsevier, pp. 469–489. doi: 10.1016/j.carbpol.2011.03.019.

Schenk, F. C. *et al.* (2014) 'Dual-functionalized nanostructured biointerfaces by click chemistry', *Langmuir*. American Chemical Society, 30(23), pp. 6897–6905. doi: 10.1021/la500766t.

Schindelin, J. *et al.* (2012) 'Fiji: An open-source platform for biological-image analysis', *Nature Methods*. Nature Publishing Group, pp. 676–682. doi: 10.1038/nmeth.2019.

Schlessinger, M. J., Lax, L. and Lemmon, M. (1995) *Regulation of Growth Factor Activation by Proteoglycans: What Is the Role of the Low Affinity Receptors?*, *Cell*.

Schwayer, C. *et al.* (2016) 'Developmental Cell Review Actin Rings of Power', *Developmental Cell*, 37, pp. 493–506. doi: 10.1016/j.devcel.2016.05.024.

Smith, M. M. and Melrose, J. (2015) 'Proteoglycans in Normal and Healing Skin', *Advances in Wound Care*. Mary Ann Liebert Inc, 4(3), pp. 152–173. doi: 10.1089/wound.2013.0464.

Sorrell, J. M. *et al.* (1999) 'Versican in human fetal skin development', *Anatomy and Embryology*. Springer, 199(1), pp. 45–56. doi: 10.1007/s004290050208.

Spatz, J. P. *et al.* (2000) 'Ordered deposition of inorganic clusters from micellar block copolymer films', *Langmuir*, 16(2), pp. 407–415. doi: 10.1021/la990070n.

Spicer A P and Lee Tien J, Y. (2004) *Molecular Genetic Dissection of Hyaluronan Function in the Mouse*. Elsevier Science Ltd. doi: 10.1016/B978-008044382-9/50057-1.

Stambaugh, C. *et al.* (2020) 'Linking mass measured by the quartz crystal microbalance to the SI', *Metrologia*. IOP Publishing, 57(2), p. 025002. doi: 10.1088/1681-7575/AB54A5.

Stern, R. (2004) 'Hyaluronan catabolism: A new metabolic pathway', *European Journal of Cell Biology*. Elsevier GmbH, 83(7), pp. 317–325. doi: 10.1078/0171-9335-00392.

Stern, R., Asari, A. A. and Sugahara, K. N. (2006) 'Hyaluronan fragments: An information-rich system', *European Journal of Cell Biology*, 85(8), pp. 699–715. doi: 10.1016/j.ejcb.2006.05.009.

Takahashi, R. *et al.* (1999) 'Effect of molecular weight distribution on the solution properties of sodium hyaluronate in 0.2M NaCl solution', *Biopolymers*. John Wiley & Sons, Ltd, 50(1), pp. 87–98. doi: 10.1002/(SICI)1097-0282(199907)50:1<87::AID-BIP8>3.0.CO;2-K.

Tammi, R. *et al.* (1991) 'Degradation of newly synthesized high molecular mass hyaluronan in the epidermal and dermal compartments of human skin in organ culture', *Journal of Investigative Dermatology*. Elsevier, 97(1), pp. 126–130. doi: 10.1111/1523-1747.ep12478553.

Tammi, R. *et al.* (2005) 'Hyaluronan synthase induction and hyaluronan accumulation in mouse epidermis following skin injury', *Journal of Investigative Dermatology*, 124(5), pp. 898–905. doi: 10.1111/j.0022-202X.2005.23697.x.

Tammi, R. H. *et al.* (2011) 'Transcriptional and post-translational regulation of hyaluronan synthesis', *FEBS Journal*. FEBS J, pp. 1419–1428. doi: 10.1111/j.1742-4658.2011.08070.x.

Tammi, R. and Tammi, M. (1991) 'Correlations between hyaluronan and epidermal proliferation as studied by [3H]glucosamine and [3H]thymidine incorporations and staining of hyaluronan on mitotic keratinocytes', *Experimental Cell Research*. Academic Press, 195(2), pp. 524–527. doi: 10.1016/0014-4827(91)90405-J.

Tavianatou, A.-G. *et al.* (2019) 'Molecular size-dependent specificity of hyaluronan on functional properties, morphology and matrix composition of mammary cancer cells', *Matrix Biology Plus*. Elsevier, p. 100008. doi: 10.1016/J.MBPLUS.2019.100008.

Thorne, R. F., Legg, J. W. and Isacke, C. M. (2004) 'The role of the CD44 transmembrane and cytoplasmic domains in co-ordinating adhesive and signalling events', *Journal of Cell Science*. The Company of Biologists Ltd, 117(3), pp. 373–380. doi: 10.1242/jcs.00954.

Tolg, C. *et al.* (2006) 'Rhamm-/- fibroblasts are defective in CD44-mediated ERK1,2 motogenic signaling, leading to defective skin wound repair', *Journal of Cell Biology*, 175(6), pp. 1017–1028. doi: 10.1083/jcb.200511027.

Toole, B. P. (2004) 'Hyaluronan: from extracellular glue to pericellular cue', *Nature Reviews Cancer*. Nature Publishing Group, 4(7), pp. 528–539. doi: 10.1038/nrc1391.

Tracy, L. E., Minasian, R. A. and Caterson, E. J. (2016) 'Extracellular Matrix and Dermal Fibroblast Function in the Healing Wound', *Advances in Wound Care*. Mary Ann Liebert, Inc., 5(3), pp. 119–136. doi: 10.1089/wound.2014.0561.

Underhill, C. B. (1992) 'The Hyaluronan Receptor: CD44', *Journal of Cell Science*, 103, pp. 293–298. doi: 10.1016/B978-008044382-9/50036-4.

Vicente-Manzanares, M., Choi, C. K. and Horwitz, A. R. (2009) 'Integrins in cell migration - The actin connection', *Journal of Cell Science*. The Company of Biologists Ltd, 122(2), pp. 199–206. doi: 10.1242/jcs.018564.

Vigetti, D. *et al.* (2009) 'Modulation of hyaluronan synthase activity in cellular membrane fractions', *Journal of Biological Chemistry*. J Biol Chem, 284(44), pp. 30684–30694. doi: 10.1074/jbc.M109.040386.

Vishwakarma, M. *et al.* (2018) 'Mechanical interactions among followers determine the emergence of leaders in migrating epithelial cell collectives', *Nature Communications*. Nature Publishing Group, 9(1), p. 3469. doi: 10.1038/s41467-018-05927-6.

Voinova, M. V *et al.* (1999) 'Viscoelastic Acoustic Response of Layered Polymer Films at Fluid-Solid Interfaces: Continuum Mechanics Approach', *Physica Scripta*. IOP Publishing, 59(5), pp. 391–396. doi: 10.1238/physica.regular.059a00391.

Wang, Y. *et al.* (2012) 'Substrate stiffness regulates the proliferation, migration, and differentiation of epidermal cells', *Burns*. Elsevier, 38(3), pp. 414–420. doi: 10.1016/j.burns.2011.09.002.

Wang, Y. *et al.* (2014) 'Plasma fibronectin supports hemostasis and regulates thrombosis', *Journal of Clinical Investigation*. American Society for Clinical Investigation, 124(10), pp. 4281–4293. doi: 10.1172/JCI74630.

Weigel, P. H. (2017) 'Planning, evaluating and vetting receptor signaling studies to assess hyaluronan size-dependence and specificity', *Glycobiology*. Springer Science+Business Media, New York, NY, 27(9), pp. 796–799. doi: 10.1093/glycob/cwx056.

Weigel, P. H. and Baggenstoss, B. A. (2017) 'What is special about 200 kDa hyaluronan that activates hyaluronan receptor signaling?', *Glycobiology*, 27(9), pp. 1–10. doi: 10.1093/glycob/cwx039.

Weinstein, G. D. and Boucek, R. J. (1960) 'Collagen and elastin of human dermis.', *The Journal of investigative dermatology*. Elsevier, 35(4), pp. 227–229. doi: 10.1038/jid.1960.109.

Woodley, D. T., Bachmann, P. M. and O'Keefe, E. J. (1988) 'Laminin inhibits human keratinocyte migration', *Journal of Cellular Physiology*, 136(1), pp. 140–146. doi: 10.1002/jcp.1041360118.

Wu, M. F. *et al.* (2017) 'Effect of human autologous serum and fetal bovine serum on human corneal epithelial cell viability, migration and proliferation in vitro', *International Journal of Ophthalmology*. International Journal of Ophthalmology (c/o Editorial Office), 10(6), pp. 908–913. doi: 10.18240/ijo.2017.06.12.

Yeom, J. *et al.* (2010) 'Effect of cross-linking reagents for hyaluronic acid hydrogel dermal fillers on tissue augmentation and regeneration', *Bioconjugate Chemistry*. Bioconjug Chem, 21(2), pp. 240–247. doi: 10.1021/bc9002647.

Zhu, X. Y. *et al.* (2001) 'Grafting of high-density poly(ethylene glycol) monolayers on Si(111)', *Langmuir*. American Chemical Society , 17(25), pp. 7798–7803. doi: 10.1021/la010672i.

List of Figures

List of Tables

Abbreviations

2D	2 dimensional
3D	3 dimensional
APTES	3-aminopropyl-triethoxysilane
BCML	Block copolymere micelle lithography
BM	Basement membrane
BMP-2	Bone morphogenetic protein-2
BSA	Bovine serum albumin
c(RGDfV)	Cell binding motif
CD44	Cluster of differentiation 44
cRGD	Cell binding motif
DAMP	Damage associated molecular patterns
DAPI	4′,6-diamidino-2-phenylindole
dH_2O	Deionized water
DMEM	Dulbecco's modified eagle's medium
DNA	Deoxyribonucleic acid
ECM	Extracellular matrix
EDTA	Ethylenediaminetetraacetic acid
EdU	5-Ethynyl-2´-deoxyuridine
EG	Ethylene glycol
EGF	Epidermal growth factor
EPDIM	Cell binding motif
EtOH	Ethanol
EZM	Extrazelluläre Matrix
FBS	Fetal Bovine Serum
GAG	Glycosaminoglycans
HA	Hyaluronic acid
HARE	HA receptor for endocytosis
HAS (1, 2, 3)	HA synthase (1, 2, 3)
HMWHA	High molecular weight HA
HYAL	Hyaluronidase
IC_{50}	Half maximal inhibitory concentration
IPL	Information Processing Language (programming language)
KGF	Keratinocyte growth factor
LMWHA	Low molecular weight HA

MEM	Minimum essential medium
MMP	Matrix-metalloproteases
MMWHA	Medium molecular weight HA
MW	Molecular weight
NHDF	Human dermal fibroblasts
NHEK	Normal human epidermal keratinocytes
NKDIL	Cell binding motif
OEG	Oligoethylenglycol
P2VP	Poly(2-Vinyl Pyridine)
PAA	Polyacrylamide
PBS	Phosphate-Buffered Saline
PDMS	Polydimethylsiloxane
PEG	Polyethylene glycol
PEG2000	$(CH_3O)_3Si$-PEG2000
PEG3000azide	$(CH_3O)_3Si$-PEG3000-N_3
PFA	Paraformaldehyde
PS	Polystyrene
PS-b-P2VP	Polystyrene-b-poly(2-vinylpyridine)
QCM-D	Quartz crystal microbalance with dissipation monitoring
Rg	Radius of gyration
ROS	Reactive oxygen species
RT	Room temperature
SAM	Self-assembled monolayer
SDS	Sodium dodecyl sulfate
SEM	Scanning electron microscopy
TFM	Traction force microscopy
TGF-β	Transforming growth factor beta
TLR2	Toll-like receptor 2
TRITC	Tetramethylrhodamine
UVO	UV ozone
VEGF	Vascular endothelial growth factor
ΔD	Change of Dissipation
Δf	Change of frequency
Δm	Absorbed / changed mass

Danksagung

Diese Arbeit wäre nicht ohne Unterstützung zustande gekommen. Daher möchte ich mich im Folgenden bei einigen Menschen bedanken.

Zu allererst danke ich Herrn Prof. Dr. Ralf Bartenschlager für seine Bereitschaft als Erstgutachter zu fungieren und für sein aktives Mitwirken währen der TAC Meetings.

Ich möchte mich ganz herzlich bei meiner Gruppenleiterin und Betreuerin PD Dr. Heike Böhm für das spannende Wundheilungsprojekt rund um die Hyaluronsäure bedanken. Heike, ich danke dir für die produktiven Diskussionen, deine wissenschaftliche Unterstützung und für dein entgegengebrachtes Vertrauen und die Freiheit mein Projekt gestalten zu dürfen.

Vielen Dank an PD Dr. Dr. Ada Cavalcanti-Adam für die aktiven Diskussionen und kritischen biologischen Fragen während der Gruppenmeetings. Ich freue mich sehr, dich in meinem Prüfungskomitee zu haben.

Außerdem möchte ich mich bei Herrn Prof. Suat Özbek für die unkomplizierte Bereitschaft das Prüfungskomitee zu vervollständigen bedanken.

Ein großes Dankeschön geht auch an Prof. Dr. Joachim Spatz für die Möglichkeit meinen PhD in seiner Arbeitsgruppe machen zu dürfen, die vielfältigen technischen Möglichkeiten am Institut sowie unseren jährlichen Retreat nach Antholz. Der wissenschaftliche Austausch im schönen Südtirol hat das Projekt jedes Mal aufs Neue deutlich vorangebracht.

Mein besonderer Dank geht an Alba Diz-Muñoz, die als TAC Mitglied meine Arbeit von Anfang an mit verfolgt hat und immer aufmunternde Worte gefunden hat. Gleichzeitig war sie auch immer darauf bedacht mich anzuleiten den Fokus dieser Arbeit nicht zu verlieren.

Ein ganz großes Dankeschön geht an alle vergangenen und aktuellen Mitarbeiter des AK Spatz, für die herzliche Aufnahme in die Gruppe, die entspannte Arbeitsatmosphäre, kurzweilige Mittags- und Kaffeepausen, sämtliche Einstands- Ausstands-, Straf- und Geburtstagskuchen und Veranstaltungen außerhalb des Labors. Vielen Dank auch für die hilfsbereite Einarbeitung und Unterstützung in technischen Fragen.

Dazu gehören natürlich auch alle Mitglieder der AG Böhm!. Besonders vielen Dank an Patricia Hegger, die während Heikes Abwesenheit eine wunderbare Gruppenleiter-Vertretung war. Ein besonderes Dankeschön geht an Burcu Minsky, die mich am Anfang trotz der kurzen Zeit mit viel Sorgfalt in die Keratinozytenkultur eingearbeitet hat.

In diesem Zusammenhang möchte ich auch all unsere hilfsbereiten technischen Assistenten(innen) nennen, dank denen alles seinen Platz im Labor hat und Lieferungen immer den richtigen Empfänger finden: Sabine Grünewald, Cornelia Weber, Annette Fautsch und Raimund Jung. Ein besonderer Dank geht an Johannes Hirte für die Einarbeitung in und Unterstützung bei allen Arbeitsschritten rund um BCML sowie die Hilfe bei den SEM Aufnahmen.

Ganz vielen Dank an Oskar Staufer für das spannende und motivierende Kollaborationsprojekt, es hat sehr viel Spaß gemacht, dich mit meinem Wissen rund um die Hautgewebemodelle unterstützen zu können.

Allen „meinen“ Praktikanten danke ich, dass sie mit mir mein Projekt weitergebracht haben: Lena Bohaumilitzky, Lelia Wagner und Lutz Neuhäuser. Ein ganz besonderer Dank geht an Lutz, der fast ein ganzes Jahr mit im Team war. Lutz, es hat super viel Spaß gemacht, mit dir zusammen zu arbeiten, zu diskutieren und deine Fortschritte mitzuverfolgen!

Herzlichen Dank an Rebecca Medda, die vielbeschäftige gute Seele der Gruppe und nun des Instituts. Vielen lieben Dank für all die wissenschaftlichen Diskussionen in denen du deine Erfahrung und dein Wissen mit mir geteilt hast, deine Geduld, wenn ich mich auch mal wiederholt habe und deine Unterstützung bei der Korrektur bis zum Ende. Vielen lieben dank dir für all die schönen Kaffeepausen, Ausflüge und Einblicke in (MPI) außerwissenschaftliche Thematiken.

Saliha meine Doktorarbeitsschwester. Was hätte ich ohne dich gemacht! Wir zwei haben fast gleichzeitig angefangen und zusammen alle Höhen und Tiefen der vergangenen Jahre geteilt. Du hast mir zugehört, wenn ich jemanden zum Reden brauchte, hast mich beschwichtigt, wenn ich mich zu sehr ärgern musste, hast mich motiviert, wenn ich mich antriebslos gefühlt habe und warst einfach immer da. Vielen lieben dank dir!

Vielen Dank auch an die Mitarbeiter der Werkstätten des MPIs sowie des PCIs. Liebe PCI-ler, ohne eure präzise Herstellung der Teflon molds wäre diese Arbeit vielleicht nur halb so dick geworden.

Ein ganz großes Dankeschön geht an die Imaging Facility vom ZMBH. Vielen Dank, dass ihr so viel Zeit und Mühe in das Makro gesteckt habt.

Vielen Dank auch an alle Mitarbeiter und Mitarbeiterinnen von HBIGS. Vielen Dank für die immerwährend schnelle und unkomplizierte Unterstützung bei allen Fragen und Sorgen! Ich bin froh, dass ich durch die Graduiertenschule durch zahlreiche Core und Additional courses mein (Fach)Wissen, aber auch mein Netzwerk zu erweitern und hilfreiche Kontakte knüpfen konnte.

Stellvertretend möchte ich mich an dieser Stelle bei allen anderen lieben Menschen bedanken, die mich in den letzten Jahren durch alle Auf und Abs begleitet haben und mich alle auf ihre Art und Weise wissentlich und unwissentlich während meiner Doktorarbeitsphase unterstützt haben.

Ein ganz großes, herzliches Dankschön geht an meine Familie, die mich in den vergangenen Jahren immer unterstützt hat, sei es durch tatkräftiges Korrekturlesen vor deadlines, beim Akkus aufladen zuhause oder im Urlaub oder einfach nur durchs Zuhören. Vielen lieben Dank!

Zuletzt möchte ich dir Martin für deine unglaubliche und fast unendliche Geduld und all dein Verständnis in den letzten Jahren danken. Du hast mich, wo immer es dir möglich war unterstützt und mir vor allem in den letzten Monaten unglaublich den Rücken freigehalten!

Danke.